



ΕΘΝΙΚΟ ΜΕΤΣΟΒΙΟ ΠΟΛΥΤΕΧΝΕΙΟ
ΣΧΟΛΗ ΕΦΑΡΜΟΣΜΕΝΩΝ ΜΑΘΗΜΑΤΙΚΩΝ
ΚΑΙ ΦΥΣΙΚΩΝ ΕΠΙΣΤΗΜΩΝ
ΤΟΜΕΑΣ ΦΥΣΙΚΗΣ
ΔΠΜΣ «ΜΙΚΡΟΣΥΣΤΗΜΑΤΑ & ΝΑΝΟΔΙΑΤΑΞΕΙΣ»



Μελέτη της αποδόμησης με
excimer laser για την
κατασκευή μικροοπτικών
διατάξεων

ΜΕΤΑΠΤΥΧΙΑΚΗ ΕΡΓΑΣΙΑ

Μαρία Α. Αναστασοπούλου

Επιβλέποντες:

Ιωάννα Ζεργιώτη

Rene Sanders

Επίκουρη Καθηγήτρια ΕΜΠ

technologist in Philips Innovation Services

Αθήνα, Μάρτιος 2012



ΕΘΝΙΚΟ ΜΕΤΣΟΒΙΟ ΠΟΛΥΤΕΧΝΕΙΟ
ΣΧΟΛΗ ΕΦΑΡΜΟΣΜΕΝΩΝ ΜΑΘΗΜΑΤΙΚΩΝ
ΚΑΙ ΦΥΣΙΚΩΝ ΕΠΙΣΤΗΜΩΝ
ΤΟΜΕΑΣ ΦΥΣΙΚΗΣ
ΔΠΜΣ «ΜΙΚΡΟΣΥΣΤΗΜΑΤΑ & ΝΑΝΟΔΙΑΤΑΞΕΙΣ»

Μελέτη της αποδόμησης με excimer laser για την κατασκευή μικροοπτικών διατάξεων

ΜΕΤΑΠΤΥΧΙΑΚΗ ΕΡΓΑΣΙΑ

Μαρία Α. Αναστασοπούλου

Επιβλέποντες:

Ιωάννα Ζεργιώτη

Rene Sanders

Επίκουρη Καθηγήτρια ΕΜΠ

technologist in Philips Innovation Services

Εγκρίθηκε από την τριμελή εξεταστική επιτροπή την ... 3/2012.

.....
Ι. Ζεργιώτη
Επικ. Καθηγήτρια ΕΜΠ

.....
Ι. Ράπτης
Καθηγητής ΕΜΠ

.....
Δ. Τσουκαλάς
Καθηγητής ΕΜΠ

Αθήνα, Μάρτιος 2012

ΕΥΧΑΡΙΣΤΙΕΣ

Η παρούσα μεταπτυχιακή εργασία εκπονήθηκε στα πλαίσια πρακτικής άσκησης στα εργαστήρια της Philips Innovation Services στο Eindhoven.

Θα ήθελα να ευχαριστήσω όλους όσους βοήθησαν στην πραγματοποίηση αυτής της εργασίας, ξεκινώντας από την επιβλέπουσα καθηγήτριά μου κ.Ιωάννα Ζεργιώτη. Την ευχαριστώ θερμά για την πολύτιμη ευκαιρία που μου έδωσε να εργαστώ στα εργαστήρια της Philips και να γνωρίσω από κοντά μια μεγάλη βιομηχανία , καθώς και να εργαστώ σε ένα πολύ ενδιαφέρον θέμα και να συνεργαστώ με σημαντικούς ανθρώπους. Επίσης την ευχαριστώ και για την υποστήριξη που μου παρείχε και κατά τη διάρκεια της εκπόνησης της εργασίας.

Επίσης, θα ήθελα να ευχαριστήσω τον επιβλέποντά μου στη Philips κ.Rene Sanders για τη συνεχή καθοδήγησή του και τις χρήσιμες συμβουλές του, από την αρχή μέχρι το τέλος της εργασίας μου. Τέλος, θα ήθελα να ευχαριστήσω όλη την ομάδα (acknowledgements) των mesooptics για την πολύτιμη συνεργασία μας, και ιδιαίτερα τον συνάδελφο και φοιτητή Longfei Shen για τη βοήθεια και την άψογη συνεργασία μας.

Πίνακας περιεχομένων

Περίληψη-Σκοπός	5
1. Εισαγωγή στην αποδόμηση με excimer laser	6
2. Αλληλεπίδραση ύλης-laser: Πολυμερή.....	6
3. Μοντέλο του Beer για την πρόβλεψη του βάθους αποδόμησης στα πολυμερή	7
3.1. Σκέδαση και απορρόφηση από το νέφος	8
3.2. Εξάρτηση από την κλίση του υποστρώματος	8
4. Προβολή μάσκας στο υπόστρωμα.....	9
5. Τεχνικές με μάσκες.....	9
5.1. Απλές δυαδικές μάσκες.....	10
5.1.1. Σταθερές μέθοδοι.....	10
5.1.2. Μέθοδοι σάρωσης.....	10
6. Excimer M8000 workstation.....	10
7. Μέθοδοι.....	11
7.1. Μέθοδος υπολογισμού της rms τιμής της τραχύτητας.....	11
7.2. Μέθοδος μείωσης της τραχύτητας	12
7.2.1. Διαμόρφωση ρυθμίσεων.....	12
8. Αποκλίσεις από το επιθυμητό σχήμα	
8.1. Επιφανειακή τραχύτητα κατά τη διαδικασία αποδόμησης.....	14
8.2. Παραμορφώσεις μεγάλης κλίμακας.....	14
8.2.1. Χαντάκια.....	15
8.2.2. Κεκλιμένα τοιχώματα	15
8.2.3. Καμπυλωμένη επιφανειακή κοιλότητα	16
9. Πειραματικά αποτελέσματα.....	16
9.1. Μελέτη σχέσης μεγέθους μάσκας – ρυθμού αποδόμησης.....	16
9.1.1. Πείραμα με κυκλικές οπές διαφορετικής διαμέτρου	16
9.1.2. Πείραμα με σχισμές διαφορετικού πλάτους.....	17
9.1.3. Συζήτηση.....	18
9.2. Δημιουργία επιφανειακού φουσκώματος.....	18
9.2.1. Εξέλιξη του σχήματος του φουσκώματος.....	18
9.2.2. Σύγκριση μεταξύ του προφίλ βάθους ενός κυκλικού και ενός τετραγωνικού ανοίγματος.....	19
9.2.3. Σύγκριση polycarbonate με polyimide: Καμπύλη αποδόμησης και προφίλ βάθους	20
9.2.4. Μερική μετακίνηση της κυκλικής τρύπας έξω από το υπόστρωμα.....	22
9.2.5. Συζήτηση.....	23
9.3. Χαντάκια.....	24
9.3.1. Χρήση ορθογωνικής μάσκας με grayscale άκρα.....	24
9.3.2. Συζήτηση.....	25
9.4. Μείωση τραχύτητας με μέθοδο σάρωσης	26
9.4.1. Συζήτηση	28
10. Επίλογος	28
Contents	29

Εισαγωγή – Σκοπός

Η αποδόμηση πολυμερών με excimer laser είναι ένα ευέλικτο και αποτελεσματικό εργαλείο στην κατασκευή μικροοπτικών δομών καθώς και σε άλλες εφαρμογές. Η ποιότητα της επιφάνειας της μικροδομής που έχει παραχθεί με αυτό τον τρόπο έχει κριτική σημασία για την επιτυχία ή μη της εφαρμογής για την οποία προορίζεται η μικροδομή. Κατά τη διάρκεια της αποδόμησης με laser, όμως, συμβαίνουν φαινόμενα που προκαλούν παραμορφώσεις και τοπογραφικές ανωμαλίες στην τελική μικροδομή.

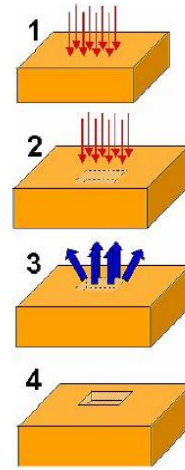
Ο σκοπός αυτής της μελέτης είναι η καταγραφή και κατανόηση των πιο σημαντικών τοπογραφικών ανωμαλιών που εισάγονται κατά τη διαδικασία της αποδόμησης. Επιπλέον για μια κατηγορία από αυτές τις τοπογραφικές ανωμαλίες, τη γνωστή τραχύτητα, εισάγεται και εφαρμόζεται μια μέθοδος για την μείωση της.

Αρχικά (1,2,3) γίνεται μια θεωρητική ανασκόπηση της διαδικασίας της αποδόμησης με laser που αφορά το κομμάτι αλληλεπίδραση της ύλης με την ακτινοβολία laser. Στη συνέχεια (4,5), περιγράφονται κάποιες τεχνικές και η μέθοδος προβολής που καθορίζει το σχήμα της μικροδομής. Έπειτα (6) περιγράφεται το σύστημα που χρησιμοποιήθηκε και εισάγεται μία μέθοδος για την εκτίμηση της τραχύτητας (7) καθώς και μία για τη μείωσή της (7). Μετά (8), γίνεται μια κατηγοριοποίηση και περιγραφή των τοπογραφικών ανωμαλιών, ενώ στο τέλος (9) παρουσιάζονται τα πειραματικά αποτελέσματα και σχολιάζονται.

Στο δεύτερο κομμάτι της εργασίας υπάρχει το αγγλικό κείμενο, όπου η θεωρία καθώς και τα πειραματικά αποτελέσματα παρουσιάζονται πιο αναλυτικά.

1. Εισαγωγή στην αποδόμηση με excimer laser

Η αποδόμηση με laser είναι η απομάκρυνση υλικού από ένα υπόστρωμα μέσω απευθείας απορρόφησης ενέργειας laser. Η έναρξη της αποδόμησης συμβαίνει πάνω από μια τιμή κατωφλίου ροής ενέργειας, η οποία εξαρτάται από το μηχανισμό απορρόφησης, τις ιδιότητες του υλικού, τη μορφολογία, την παρουσία ατελειών, καθώς και από παραμέτρους του laser όπως το μήκος κύματος και η διάρκεια του παλμού. Κατά τη διάρκεια της αποδόμησης μπορεί να λαμβάνουν χώρα διάφοροι μηχανισμοί, οι οποίοι εξαρτώνται από το συγκεκριμένο υλικό που ακτινοβολείται καθώς και από παραμέτρους επεξεργασίας με laser όπως το μήκος κύματος, η ροή της ενέργειας και το μήκος του παλμού.



Εικόνα 1: Βήματα αποδόμησης με excimer laser: 1) Ακτινοβολήση του υλικού με παλμό laser, 2) η παλμική ενέργεια απορροφάται τοπικά, 3) εκτόξευση των σωματιδίων του υλικού, 4) άνοιγμα μιας μικροσπής

Την τελευταία δεκαετία, η αποδόμηση υλικών με excimer laser απέκτησε τη φήμη μιας αξιόπιστης τεχνολογίας για την κατασκευή μικροδομών. Αυτή η τεχνολογία δεν απαιτεί εγκαταστάσεις καθαρού χώρου, μπορεί να εφαρμοσθεί σε μια ευρεία κλίμακα υλικών και είναι σχετικά γρήγορη, μιας και επιτρέπει την παράλληλη μικροεπεξεργασία και κατασκευή δομών μέσω μοτίβων μασκών. Αυτό σημαίνει ότι η τεχνική είναι κατάλληλη και για δημιουργία προτύπων και για κατασκευή μικροδομών σε μικρούς αριθμούς, ή για εφαρμογές όπου τα συμβατικά εργαλεία όπως μηχανικές διατρήσεις δεν έχουν την απαραίτητη ακρίβεια. Στην βιομηχανία κατασκευής μικροφακών, το κύριο πλεονέκτημα αυτής της απευθείας τεχνικής βρίσκεται στην ικανότητα κατασκευής μικροφακών με χαρακτηριστικά που μπορούν να προσαρμοστούν για κάθε φακό ξεχωριστά.

2. Αλληλεπίδραση ύλης-laser: Πολυμερή

Τα πολυμερή προσφέρουν χαμηλά κατώφλια αποδόμησης ($0.01-0.5 \text{ J/cm}^2$), ακμές υψηλής ποιότητας και παρατηρείται μικρή ή καθόλου θερμική καταστροφή στο γύρω υλικό. Οι τυπικοί δεσμοί στις μοριακές αλυσίδες έχουν ενέργειες που είναι στο ίδιο εύρος με τις ενέργειες των φωτονίων του excimer. Αυτή η ιδιότητά τους είναι υπεύθυνη για τους υψηλούς συντελεστές

απορρόφησης σε μήκη κύματος UV και το φαινόμενο ψυχρής αποδόμησης (cold ablation): τα απορροφημένα φωτόνια διεγείρουν ηλεκτρονιικές καταστάσεις σε συγκεκριμένους οργανικούς δεσμούς και η χαλάρωση από τη διεγερμένη κατάσταση μπορεί να γίνει μέσω απευθείας διάσπασης. Στην πράξη, η διαδικασία της αποδόμησης πάντα περιλαμβάνει θερμική και μη θερμική διάσπαση και εξάτμιση. Γενικότερα, τα πολυμερή συνθέτουν μια πολύ καλή ομάδα για τη διαδικασία αποδόμησης με laser.

Πολυμερή που αποσυνθέτονται σε θραύσματα είναι για παράδειγμα τα polyimides και τα polycarbonates. Αυτά τα πολυμερή δείχνουν στην περίπτωση της αποσύνθεσης (θερμικής ή φωτοχημικής) μια τάση για έκδηλο κατακερματισμό σε διάφορα μικρά μόρια.

3. Μοντέλο του Beer για την πρόβλεψη του βάθους αποδόμησης στα πολυμερή

Για την κατανόηση του φαινομένου της αποδόμησης με laser, μπορούν να διακριθούν φωτοχημικοί και φωτοθερμικοί μηχανισμοί, οι οποίοι εξαρτώνται από τις παραμέτρους του laser και τις ιδιότητες των υλικών. Στους φωτοχημικούς μηχανισμούς, η ενέργεια των φωτονίων είναι αρκετά υψηλή ώστε να προκαλέσει απευθείας διάσπαση των χημικών δεσμών, προκαλώντας την αποδόμηση του υλικού. Στους φωτοθερμικούς μηχανισμούς, τα φωτόνια από το laser θερμαίνουν ορισμένη ποσότητα του υλικού σε σημείο όπου οι θερμικές διεργασίες έχουν ως αποτέλεσμα την αποσύνθεση και την εκτόξευση του υλικού. Στην πράξη, και οι δύο αυτοί μηχανισμοί είναι υπεύθυνοι για την αποδόμηση με laser. Εάν, όπως στα περισσότερα πολυμερή, το μήκος θερμικής διάχυσης είναι πολύ μικρό συγκριτικά με το μήκος απορρόφησης της ακτινοβολίας laser, η έκταση της διέγερσης του υλικού καθορίζεται κυρίως από την οπτική απορρόφηση των φωτονίων. Αυτό οδηγεί σε ένα ευρέως διαδεδομένο μοντέλο που βασίζεται στο νόμο του Beer:

$$d(F) = \frac{1}{a_{eff}} \ln \left[\frac{F}{F_{th}} \right] \quad (1)$$

Οι δύο κύριες παράμετροι που περιγράφουν την αποδόμηση με laser είναι ο ρυθμός αποδόμησης $d(F)$ και το κατώφλι της ροής της ενέργειας F_{th} , η οποία ορίζεται ως η μικρότερη ροή ενέργειας στην οποία μπορεί να παρατηρηθεί η έναρξη της αποδόμησης. Μια τρίτη σημαντική παράμετρος είναι ο ενεργός συντελεστής απορρόφησης, a_{eff} , που περιέχει πληροφορίες σχετικά με τους μηχανισμούς που λαμβάνουν χώρα κατά τη διαδικασία της αποδόμησης σε αντίθεση με το γραμμικό συντελεστή αποδόμησης a_{lin} που μετράται σε μη ακτινοβολημένα υμένα πολυμερών.

Η ανακλαστικότητα της επιφάνειας (R) πολλές φορές αγνοείται, μιας και κατέχει το 6-10% της συνολικής πυκνότητας ροής. Μπορεί να ενσωματωθεί στην παραπάνω εξίσωση του Beer ως εξής:

$$d(F) = \frac{1}{a_{eff}} \ln \left[(1 - R) \frac{F}{F_{th}} \right] \quad (2)$$

3.1. Σκέδαση και απορρόφηση από το νέφος

Η εκτόξευση των σωματιδίων από την επιφάνεια λόγω της ακτινοβόλησης οδηγεί στο σχηματισμό ενός σύννεφου αποδομημένου υλικού που κινείται ταχέως μακριά από την επιφάνεια. Συνήθως, ένα τέτοιο σύννεφο αποτελείται από διεγερμένα ή στη βασική κατάσταση ουδέτερα, ηλεκτρόνια και ιόντα.

Η σκέδαση και η απορρόφηση της ακτινοβολίας laser από αυτό το νέφος, το οποίο είναι γνωστό ως φαινόμενο ασπίδας (shielding effect), επηρεάζει δραστικά την αποτελεσματικότητα της διαδικασίας αποδόμησης με laser. Αφού το εκτοξευμένο νέφος αλληλεπιδρά με την ακτινοβολία laser, οδηγεί σε εξασθένιση της ενέργειας που εναποτίθεται στο υλικό και μειώνει το ρυθμό αποδόμησης.

Όταν αυτό το φαινόμενο λαμβάνεται υπόψη, το μοντέλο του Beer τροποποιείται ως εξής:

$$d(F) = \frac{\mu}{\alpha \mu_p} \ln \left\{ 1 + \mu_p (F - F_{th}) / \mu F_{th} \right\} \quad (3)$$

Εδώ τα $\mu = \alpha / \rho$ και $\mu_p = \alpha_p / \rho_p$ είναι οι συντελεστές απορρόφησης μάζας για το στερεό πολυμερές και το νέφος αντίστοιχα.

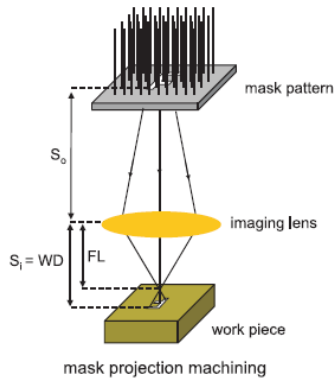
3.2. Εξάρτηση από την κλίση του υποστρώματος

Όταν επεξεργάζονται επιφάνειες με ποικίλο ύψος, η πρόσπτωση της ακτινοβολίας δεν είναι κάθετη αλλά έχει κάποια κλίση θ . Εκτός από ένα γεωμετρικό παράγοντα $\cos\theta$ μείωσης της ενέργειας υπάρχουν και άλλοι παράγοντες που πρέπει να ληφθούν υπόψη και συμπεριλαμβάνονται στο παρακάτω τροποποιημένο μοντέλο του Beer.

$$d(F) = \frac{\mu \cos\theta}{\mu_p \alpha_0} \ln \left[1 + \frac{\mu_p (1 - R_\theta) F}{\mu (1 - R_0) F_{T0}} - \frac{\mu_p \alpha_0}{\mu \alpha_\theta \cos\theta} \right] \quad (4)$$

Όπου το R_θ είναι ο συντελεστής ανάκλασης της επιφάνειας, α_θ είναι ο ενεργός συντελεστής απορρόφησης του πολυμερούς κατά μήκος του x για γωνία πρόσπτωσης θ και α_0 και R_0 είναι οι αντίστοιχοι συντελεστές για κάθετη πρόσπτωση.

4. Προβολή μάσκας στο υπόστρωμα



Εικόνα 2: Σύστημα προβολής, μάσκα-φακός-υπόστρωμα

Καθώς η δέσμη των excimer lasers είναι πολυρυθμική, δεν εστιάζεται πολύ καλά. Όμως, οι μεγάλες εγκάρσιες διαστάσεις της, καθιστούν αυτά τα lasers κατάλληλα για τεχνικές προβολής και απεικόνισης μάσκας. Μια γενική διάταξη για ένα αυτοματοποιημένο σταθμό κατεργασίας υλικών με laser δίνεται στο διπλανό σχήμα. Μια δέσμη laser χρησιμοποιείται για να ακτινοβολήσει μια μάσκα, η οποία αποτελείται από αδιαφανείς και διαφανείς περιοχές. Οι προσπίπτουσες ακτίνες πάνω στα διαφανή μέρη διαβιβάζονται μέσω της μάσκας, συλλέγονται από τον φακό απεικόνισης και κατευθύνονται πάνω στην επιφάνεια του υποστρώματος. Εάν αυτό βρίσκεται στο επίπεδο απεικόνισης, η γεωμετρία πάνω στο υπόστρωμα θα είναι πανομοιότυπη με το μοτίβο της μάσκας, εκτός από ένα σταθερό παράγοντα μείωσης μεγέθυνσης του συστήματος. Οι θέσεις της μάσκας, του υποστρώματος και του φακού σχετίζονται μεταξύ τους ως:

$$\frac{1}{S_o} + \frac{1}{S_i} = \frac{1}{FL} \quad (5)$$

Ο λόγος S_o/S_i ισούται με το παράγοντα μείωσης μεγέθυνσης DM.

Αφού οι διαστάσεις της εικόνας διαιρούνται με ένα παράγοντα $(DM)^{-1}$, η ένταση (ή η ροή ενέργειας) πάνω στο υπόστρωμα πολλαπλασιάζεται με $(DM)^2$ εκτός από τις απώλειες μετάδοσης που μπορεί να προκύψουν στο οπτικό μονοπάτι.

5. Τεχνικές με μάσκες

Όλες οι τεχνικές για την κατασκευή 3D δομών χρησιμοποιούν ειδικά σχέδια μασκών. Συγκεκριμένα, δύο οικογένειες βασικών μασκών χρησιμοποιούνται: οι απλές δυαδικές μάσκες και οι μάσκες γκριζας κλίμακας (grayscale).

5.1. Απλές δυαδικές μάσκες

Σε μια απλή δυαδική μάσκα (0 ή 100% μετάδοση), κάθε παλμός laser απομακρύνει υλικό από το υπόστρωμα στο ίδιο βάθος σε όλες τις εκτεθειμένες περιοχές. Διάφορες μέθοδοι μπορούν να χρησιμοποιηθούν για να παραχθούν χαρακτηριστικά με ποικίλο βάθος από την επιφάνεια.

5.1.1. Σταθερές μέθοδοι

Η πιο απλή και διαδεδομένη μέθοδος είναι η step and repeat. Σε αυτή τη μέθοδο η μάσκα ακτινοβολείται και παράγεται μια συγκεκριμένη δομή στο υπόστρωμα. Η ίδια δομή μπορεί να αναπαραχθεί με τον εξής απλό τρόπο: το laser ακτινοβολεί τη μάσκα, το laser κλείνει, το δείγμα μετακινείται εγκάρσια ή οριζόντια και ακτινοβολεί ξανά τη νέα περιοχή για να παραχθεί η ίδια δομή ξανά.

5.1.2. Μέθοδοι σάρωσης

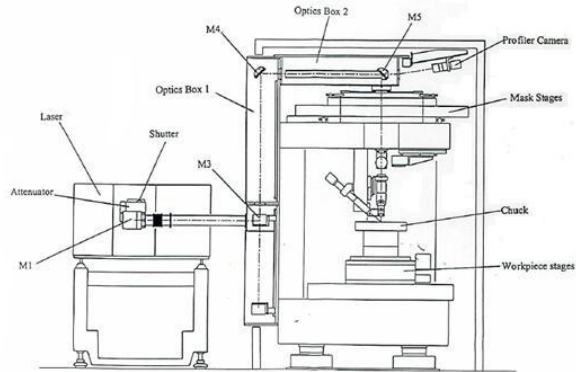
Εάν η μάσκα μετακινείται κατά την ακτινοβολήση του laser, μπορούν να παραχθούν δομές που το προφίλ βάθους τους θα ποικίλει. Αυτό μπορεί να επιτευχθεί διασφαλίζοντας ότι ένα άνοιγμα κινείται κάθετα ή οριζόντια της δέσμης laser με ένα απόλυτα ελεγχόμενο τρόπο κατά τη διάρκεια της ακτινοβολήσης. Έτσι το στατικό υπόστρωμα εκτίθεται σε μία συνεχόμενα διαφορετική ποσότητα ενέργειας κατά μήκος της εκτιθέμενης περιοχής, που παράγει μια κλίση βάθους στο δείγμα. Αυτή η τεχνική είναι γνωστή ως mask dragging. Από την άλλη μεριά, εάν μετακινείται το υπόστρωμα αλλά παραμένει σταθερή η μάσκα τότε η τεχνική ονομάζεται workpiece dragging.

Η SIS (Synchronized Image Scanning) είναι μια παραλλαγή των παραπάνω τεχνικών, στην οποία το δείγμα σύρεται κάτω από μια γραμμική σειρά από ανοίγματα μάσκας που το μέγεθός τους αυξάνεται ή μειώνεται διαδοχικά και ακτινοβολούνται επίσης διαδοχικά από τη δέσμη laser. Το βήμα ακτινοβολήσης του laser τίθεται ίσο με το διάστημα μεταξύ των ανοιγμάτων της μάσκας έτσι ώστε κάθε σημείο στο δείγμα να εκτίθεται σε ένα μόνο παλμό από κάθε άνοιγμα με τη σειρά.

6. Excimer M8000 workstation

Σε αυτή τη μελέτη χρησιμοποιήθηκε ένα KrF excimer laser system Series M8000 (Exitech Limited, UK) εξοπλισμένο με LPX210 (Lambda Physik, Germany) πηγή laser με μήκος κύματος 248 nm και 20ns χρονική διάρκεια. Το σύστημα μετάδοσης της δέσμης περιείχε οπτικά διαμόρφωσης και

ομογενοποίησης της δέσμης έτσι ώστε να δημιουργούν μια ομοιόμορφη, τετραγωνική δέσμη στο επίπεδο της μάσκας. Το σύστημα του laser ελέγχεται από υπολογιστή που τρέχει MS Windows NT είτε χειροκίνητα είτε μέσω script. Το περιβάλλον του θαλάμου που βρίσκεται το προς ακτινοβολήση υλικό βρίσκεται σε ατμοσφαιρικό αέρα. Το πολυμερές που ακτινοβολήθηκε ήταν polycarbonate πάχους 1 mm.



Εικόνα 3: Πλάγια όψη του σταθμού εργασίας M8000 Excimer

7. Μέθοδοι

Αναπτύχθηκαν μία μέθοδος για την ποσοτική εκτίμηση της τραχύτητας και μία μέθοδος για τη μείωσή της.

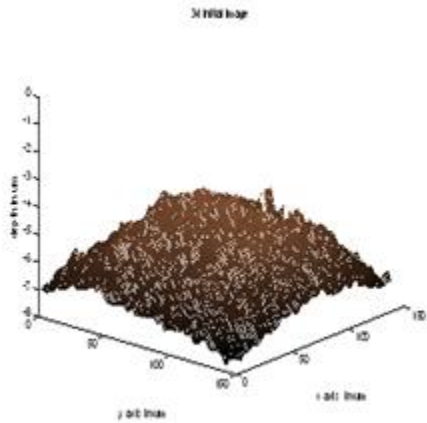
7.1. Μέθοδος υπολογισμού της rms τιμής της τραχύτητας

Η RMS τιμή της τραχύτητας (R_q) για μια ψηφιακή εικόνα υπολογίζεται από τον τύπο:

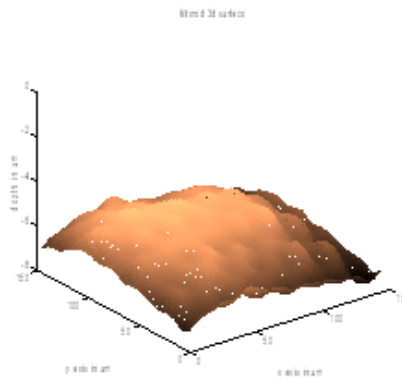
$$R_q = \sqrt{\frac{1}{MN} \sum_{i=1}^M \sum_{j=1}^N Z^2(x_i, y_j)} \quad (6)$$

Όταν το ύψος Z υπολογίζεται αφαιρώντας την ιδανικά επίπεδη επιφάνεια από την πραγματική επιφάνεια του δείγματος, η τραχύτητα υπερτιμάται. Αυτό συμβαίνει επειδή η παραμόρφωση ενσωματώνεται στον υπολογισμό της τραχύτητας.

Για να αποφευχθεί αυτό, ένα δισδιάστατο ιδανικό βαθυπερατό φίλτρο εφαρμόζεται στην επιφάνεια και έχει σαν έξοδο μια εξομαλυμένη επιφάνεια που περιλαμβάνει την παραμόρφωση, αλλά είναι απαλλαγμένη από την τραχύτητα. Το Z υπολογίζεται από την αφαίρεση της εξομαλυμένης επιφάνειας από την αρχική.



Εικόνα 4: Αρχική εικόνα επιφάνειας



Εικόνα 5: Εικόνα φιλτραρισμένης επιφάνειας

7.2. Μέθοδος μείωσης της τραχύτητας

Παρότι το προφίλ της έντασης της δέσμης laser θεωρητικά πρέπει να είναι πλήρως ομοιόμορφο και ομογενές, υπάρχουν χρονικές και χωρικές ανομοιομορφίες οι οποίες προκαλούν τραχύτητα.

Η βασική ιδέα της επόμενης τεχνικής είναι η μείωση της τραχύτητας εξαιτίας της χωρικής ανομοιομορφίας της δέσμης, παίρνοντας το μέσο όρο της άνισης κατανομής της κατανομής της ενέργειας. Αυτό πετυχαίνεται με ακτινοβολήση του υποστρώματος από διαφορετικά σημεία της δέσμης.

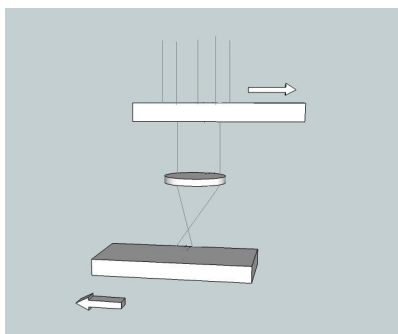
7.2.1. Διαμόρφωση ρυθμίσεων

Σε αυτή την τεχνική χρησιμοποιείται μια μέθοδος σάρωσης. Το δείγμα τοποθετείται σε μια μηχανοκίνητη βάση που μπορεί να κινείται στον τρισδιάστατο χώρο μέσω ελεγχόμενης από υπολογιστή περιστροφής γ και μετακίνησης στο x , y , z άξονα. Η μάσκα κρατείται σε ένα ανοικτό πλαίσιο και μπορεί να κινηθεί στον δισδιάστατο χώρο στους άξονες u και v . Οι άξονες u και x είναι οριζόντιοι, ενώ οι y και v είναι κάθετοι.

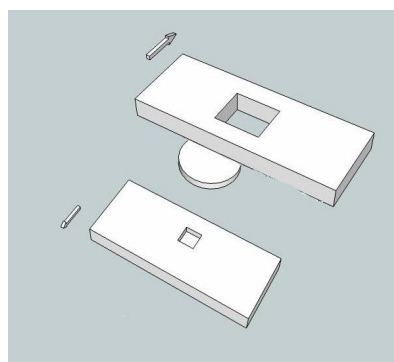
Για να παραχθεί μια συγκεκριμένη δομή εφαρμόζεται ένας αριθμός επαναλήψεων. Παρακάτω φαίνεται ένα υπεραπλουστευμένο μοντέλο της προβολής της μάσκας.

Μία επανάληψη αποτελείται από τα εξής βήματα:

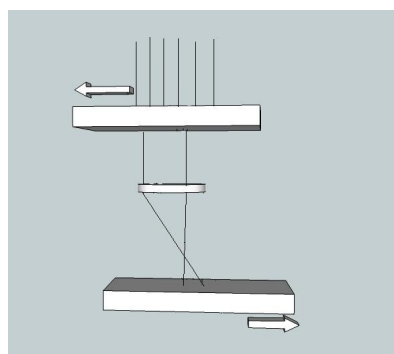
Στο πρώτο βήμα υπάρχει μια οριζόντια μετατόπιση της βάσης του δείγματος στον άξονα x (Δx) και ταυτόχρονα μια αντίθετη οριζόντια μετατόπιση του u άξονα (Δu) της βάσης της μάσκας. Η ταχύτητα της βάσης της μάσκας είναι πενταπλάσια της ταχύτητας της βάσης του δείγματος λόγω του παράγοντα μείωσης της μεγέθυνσης $5x$. Κατά τη διάρκεια αυτής της συγχρονισμένης κίνησης, το laser ακτινοβολεί παλμούς.



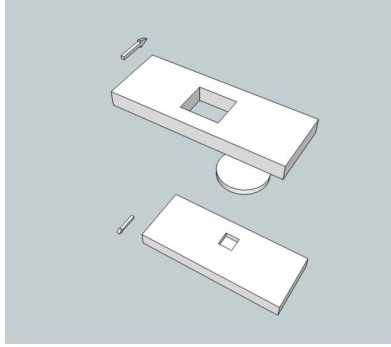
Στο δεύτερο βήμα, υπάρχει μια παρόμοια κίνηση που γίνεται αυτή τη φορά εγκάρσια. Δηλαδή, αντί για x - u μετατόπιση, έχουμε y - v μετατόπιση. Εδώ το laser παραμένει ανενεργό.



Το τρίτο βήμα είναι μια πανομοιότυπη επανάληψη του πρώτου βήματος αλλά ανάποδα.



Τέλος, το τελευταίο βήμα είναι μια επανάληψη του δεύτερου βήματος.



8. Αποκλίσεις από το επιθυμητό σχήμα

Παρότι η αποδόμηση με laser είναι μια τεχνική μεγάλης ακρίβειας και τα πολυμερή είναι κατάλληλα για να επιτύχουν ένα ελέγξιμο και ιδανικό τελικό αποτέλεσμα, πάντα υπάρχουν αποκλίσεις από το επιθυμητό και προβλέψιμο σχήμα της τελικής δομής του δείγματος. Αυτές οι αποκλίσεις μπορεί να προέρχονται είτε από την ίδια τη διαδικασία της αποδόμησης είτε από ατελή σχεδιασμό της μάσκας (π.χ. για grayscale μάσκες, σφάλματα κβαντοποίησης λόγω του μικρού αριθμού διαφορετικών επιπέδων μετάδοσης). Αυτή η εργασία είναι επικεντρωμένη στις ανωμαλίες της επιφάνειας που προκαλούνται κατά τη διάρκεια της φυσικής διαδικασίας της αποδόμησης.

Ο σκοπός της κατασκευής 3D δομών δεν είναι μόνο η δημιουργία μιας επιθυμητής τοπογραφίας στο υπόστρωμα αλλά και η διατήρηση μιας λείας επιφάνειας. Αυτό είναι ιδιαίτερα σημαντικό για εφαρμογές σε μικροοπτικές διατάξεις και μικρορευστά. Συνεπώς, ένας βολικός τρόπος αντιμετώπισης των ανωμαλιών της επιφάνειας είναι να τις κατηγοριοποιήσουμε σε σχέση με την κλίμακα μεγέθους τους. Η τραχύτητα μπορεί να θεωρηθεί ως μια παραμόρφωση μικρής κλίμακας, ενώ τα κεκλιμένα τοιχώματα των κοιλοτήτων, τα «φουσκώματα» και τα σχηματικά λάθη μπορεί να θεωρηθούν ως παραμορφώσεις μεγάλης κλίμακας.

8.1. Επιφανειακή τραχύτητα κατά τη διαδικασία αποδόμησης

Μια ανάλυση των παραγόντων που καθορίζουν την τραχύτητα μιας αποδομημένης από excimer laser επιφάνειας πολυμερούς πρέπει να λάβει υπόψη της ιδιότητες των υλικών καθώς και οπτικούς παράγοντες.

Προκειμένου να βελτιωθεί η ποιότητα της επιφάνειας (και να εξαλειφτεί η τραχύτητα) είτε η διαδικασία της αποδόμησης με laser πρέπει να βελτιωθεί είτε πρέπει να εφαρμοστεί κάποια μέθοδος μετά την αποδόμηση.

Οι διακυμάνσεις της ροής της ενέργειας σε μια ονομαστικά ομοιόμορφα δέσμη είναι ένας βασικός παράγοντας παραγωγής τραχύτητας. Μια απλή ιδέα που έχει αναπτυχθεί είναι η ισοκατανομή της χωρικής πυκνότητας ροής ενέργειας της δέσμης laser στην αποδομημένη περιοχή ακτινοβολώντας το δείγμα από διαφορετικά περιοχές της δέσμης laser. Αυτό μπορεί να επιτευχθεί με περιστροφή του δείγματος. Το κέντρο της μάσκας ευθυγραμμίζεται με το κέντρο περιστροφής της τράπεζας του δείγματος. Η ταυτόχρονη περιστροφή και ακτινοβολήση του δείγματος παράγει μια 3D αξονικά συμμετρική δομή. Βέβαια μια τέτοια μέθοδος περιλαμβάνει πολλούς περιορισμούς ως προς το σχήμα των δομών που μπορεί να παράγει.

Υπάρχουν όμως και μέθοδοι που εφαρμόζονται μετά την παραγωγή του δείγματος. Μια ομάδα τέτοιων τεχνικών χρησιμοποιεί την ανάττηξη του υλικού είτε απαλύνοντας το υλικό σε υψηλές θερμοκρασίες είτε λιώνοντας μια λεπτή επιφανειακή στοιβάδα μέσω παλμικής εφαρμογής ενέργειας.

8.2. Παραμορφώσεις μεγάλης κλίμακας

8.2.1. Χαντάκια

Μια πολύ κοινή παραμόρφωση είναι η κακής ποιότητα επιφάνεια της μικροδομής κοντά στις άκρες. Όπως μπορεί να παρατηρηθεί, η περιοχή κοντά στα τοιχώματα είναι βαθύτερη και σχηματίζεται μια δομή που μοιάζει με χαντάκι. Η εξήγηση για τη δημιουργία αυτού του χαρακτηριστικού θεωρείται ότι είναι η ανάκλαση του φωτός από τους απόκρημνους τοίχους της τρύπας η οποία συμβάλει σε μια αυξημένη ταχύτητα αποδόμησης. Το φως συσσωρεύεται στον πυθμένα γειτονικά των τοιχωμάτων και κατά συνέπεια «κόβει παραπάνω» κατά μία μικρή ποσότητα την περιοχή. Επίσης μια εξήγηση που περιλαμβάνει περίθλαση του φωτός μπορεί να εφαρμοστεί σε ορισμένες περιπτώσεις.

8.2.2. Κεκλιμένα τοιχώματα

Παρότι τα τοιχώματα της κοιλότητας θα έπρεπε να είναι κατακόρυφα στην επιφάνεια, έχουν ορισμένη κλίση. Η απαρχή της κλίσης των τοιχωμάτων στα πραγματικά συστήματα είναι αποτέλεσμα του «θαμπώματος» των άκρων λόγω φαινομένων που μπορούν να περιλαμβάνουν περίθλαση, ατέλειες στο οπτικό σύστημα, θέρμανση και πιθανές παραμορφώσεις, έτσι ώστε η γωνία των τοιχωμάτων εξαρτάται από πολλούς παράγοντες. Οι πιο σημαντικοί από αυτούς είναι η

προσπίπτουσα ακτινοβολία, το αριθμητικό άνοιγμα του συστήματος προβολής, η σύνθεση του υλικού και το μήκος κύματος.

8.2.3. Καμπυλωμένη επιφανειακή κοιλότητα

Όταν δυαδικές μάσκες χρησιμοποιούνται, η επιφάνεια του πυθμένα ιδανικά πρέπει να είναι τελείως επίπεδη. Πάραυτα, η ιδανικά επίπεδη επιφάνεια ποτέ δεν επιτυγχάνεται πειραματικά. Αντιθέτως, σε μερικές περιπτώσεις παρατηρήθηκε ένας επιφανειακά κυρτωμένος πυθμένας. Αυτό το φαινόμενο είναι ιδιαίτερα οξυμμένο σε κυκλικές τρύπες παρά σε ορθογώνιες και μπορεί να χαρακτηριστεί ως «καρούμπαλο».

9. Πειραματικά αποτελέσματα

Οι μετρήσεις της τοπολογίας των δειγμάτων πραγματοποιήθηκαν με το Wyko NT1100 ιντερφερόμετρο λευκού φωτός.

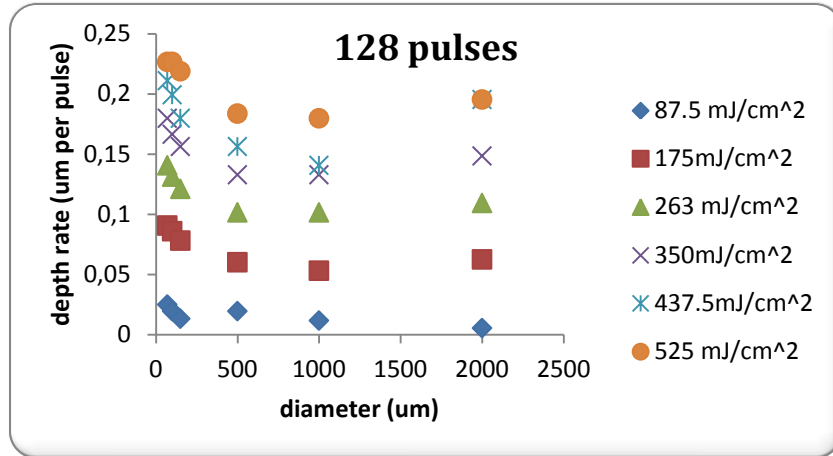
9.1. Μελέτη σχέσης μεγέθους μάσκας – ρυθμού αποδόμησης

Σε αυτή τη σειρά πειραμάτων μελετήθηκε η εξάρτηση του ρυθμού αποδόμησης από το μέγεθος της μάσκας της μικροδομής και κατά συνέπεια της ίδιας της μικροδομής. Έχει παρατηρηθεί στη βιβλιογραφία ότι όταν το μέγεθος της δέσμης laser έχει διάμετρο κάτω από 200 μm, ο ρυθμός αποδόμησης αρχίζει και εξαρτάται από τη διάμετρο της δέσμης. Συγκεκριμένα φαίνεται ότι ο ρυθμός αποδόμησης μειώνεται με την αύξηση της διαμέτρου.

9.1.1. Πείραμα με κυκλικές οπές διαφορετικής διαμέτρου

Στο συγκεκριμένο πείραμα ακτινοβολήθηκαν 6 κυκλικά ανοίγματα από τη μάσκα, από τα οποία το καθένα είχε διαφορετική διάμετρο. Συγκεκριμένα η διάμετρος των οπών ήταν: 75μm, 100μm, 150μm, 500μm, 1mm και 2mm. Κάθε οπή ακτινοβολήθηκε με 2, 4, 8, 16, 32, 64, 128 και 256 παλμούς με συχνότητα 50 Hz. Η ροή ενέργειας ήταν διαδοχικά 87.5 mJ/cm², 175mJ/cm², 263 mJ/cm², 350 mJ/cm², 437.5 mJ/cm² and 525 mJ/cm².

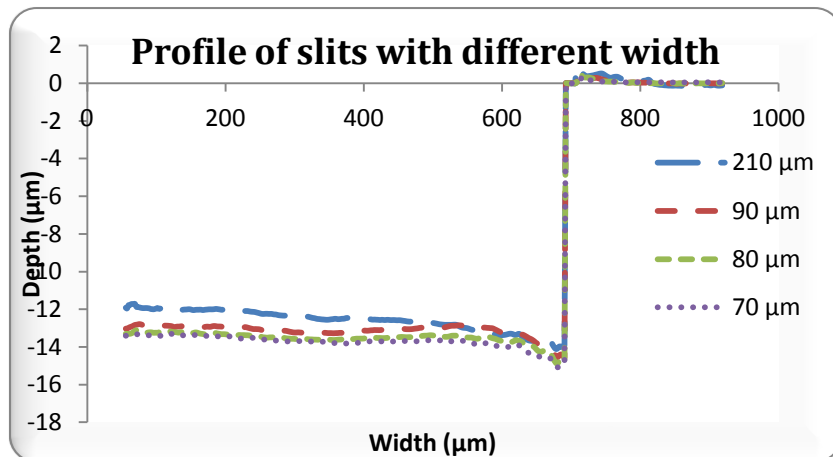
Το παρακάτω γράφημα αναπαριστά τους διαφορετικούς ρυθμούς αποδόμησης για κάθε οπή και ροή ενέργειας για 128 παλμούς. Από το παρακάτω γράφημα είναι φανερό ότι ο ρυθμός αποδόμησης μειώνεται καθώς η διάμετρος αυξάνεται και αυτό παρατηρείται μέχρι και τη διάμετρο των 500 μm.



Γράφημα 1: Ρυθμός αποδόμησης τρυπών με διαφορετική διάμετρο

9.1.2. Πείραμα με σχισμές διαφορετικού πλάτους

Στη συνέχεια πραγματοποιήθηκε ένα ακόμα πείραμα με σχισμές με διαφορετικά πλάτη αντί για κυκλικές τρύπες με διαφορετικές διαμέτρους. Όπως φαίνεται από την παρακάτω γραφική, όπου αναπαριστάται το εγκάρσιο προφίλ της επιφάνειας της κάθε κοιλότητας, υπάρχει μια φανερή μείωση του βάθους της κοιλότητας καθώς το πλάτος της σχισμής μεγαλώνει.



Γράφημα 2: Προφίλ κοιλότητας σχισμών με διαφορετικό πλάτος

9.1.3. Συζήτηση

Σύμφωνα με τα προηγούμενα πειράματα, επιβεβαιώθηκε μια εξάρτηση του ρυθμού αποδόμησης από το μέγεθος της μικροδομής και κατά συνέπεια της μάσκας. Επίσης φαίνεται ότι αυτή η εξάρτηση υπάρχει και για τα κυκλικά και για τα τετραγωνικά σχήματα. Ο ρυθμός αποδόμησης αυξάνεται καθώς μειώνεται το μέγεθος της προς ακτινοβολήση μάσκας. Επίσης φαίνεται ότι αυτή η παρατήρηση ισχύει για μεγέθη κάτω από τα 500 μm.

Δεν υπάρχει κοινά αποδεκτή εξήγηση για αυτή τη συμπεριφορά, αλλά όλες οι πιθανές εξηγήσεις συγκλίνουν στη συσχέτιση αυτού του φαινομένου με την εκτόνωση του νέφους και το φαινόμενο ασπίδας. Μια υπόθεση σχετίζεται με τη δυναμική του νέφους και το σχήμα εκτόνωσης. Πιθανολογείται ότι το σχήμα του νέφους καθώς και τρόπος εξάπλωσης εξαρτάται από το μέγεθος της τρύπας. Διαφορετικό σχήμα και διαφορετική κινητική του νέφους προκαλεί και διαφορετικό φαινόμενο ασπίδας, έτσι ώστε στις μικρότερες τρύπες το φαινόμενο να είναι πιο ασθενές και περισσότερη ακτινοβολία να φτάνει στην επιφάνεια. Μια άλλη πιθανή εξήγηση έχει να κάνει επίσης με το φαινόμενο ασπίδας που είναι πιο ασθενές στις μικρότερες τρύπες, αλλά αυτή τη φορά αυτό συμβαίνει εξαιτίας της μεγαλύτερης συγκέντρωσης των εκτοξευμένων σωματιδίων και ειδικότερα των συσσωμάτων (clusters). Τα clusters στις μεγαλύτερες τρύπες θεωρείται ότι έχουν μεγαλύτερο μέγεθος, κάτι που επίσης συμβάλει σε μεγαλύτερη εξασθένιση της ακτινοβολίας.

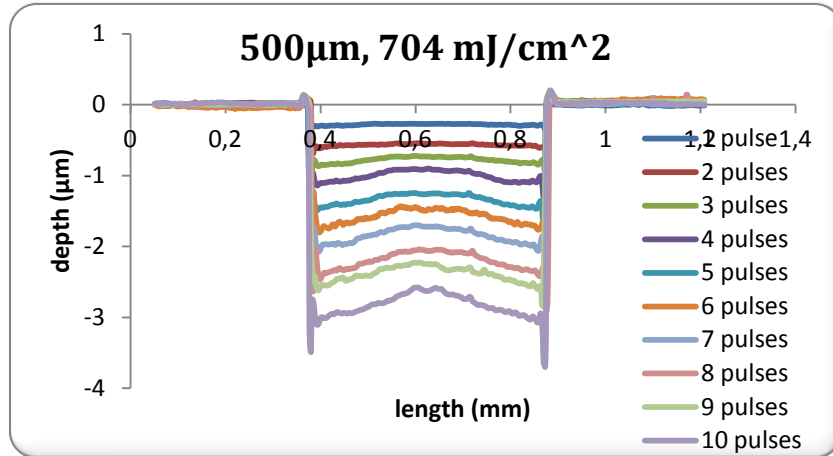
Εν κατακλείδι, αυτή η εξάρτηση ρυθμού αποδόμησης-μεγέθους τρύπας θα πρέπει να ληφθεί σοβαρά υπόψη στην κατασκευή των μικροδομών, διότι μπορεί να οδηγήσει σε αποκλίσεις από την προβλεπόμενη τελική κατασκευή.

9.2. Δημιουργία επιφανειακού φουσκώματος

Μια σοβαρή παραμόρφωση και συγκεκριμένα η δημιουργία ενός φουσκώματος στο κέντρο της επιφάνειας των κυκλικών κοιλοτήτων παρατηρήθηκε. Μια σειρά πειραμάτων πραγματοποιήθηκε για την καλύτερη κατανόηση αυτού του φαινομένου.

9.2.1. Εξέλιξη του σχήματος του φουσκώματος

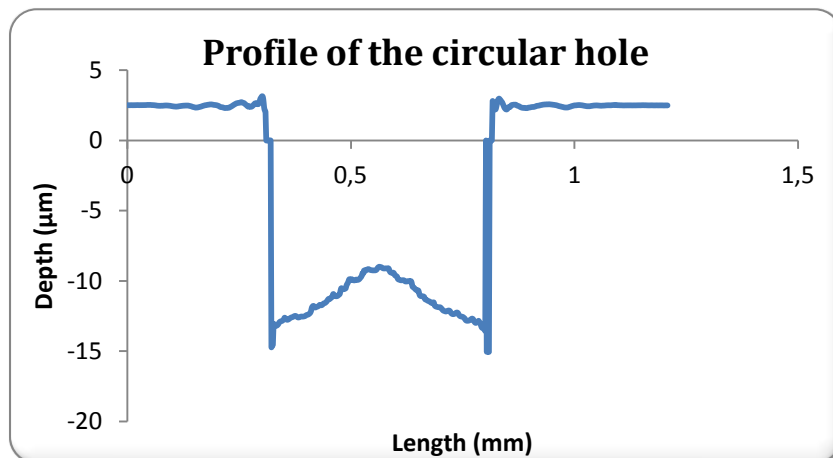
Ένα κυκλικό άνοιγμα με διάμετρο 500 μm ακτινοβολήθηκε με 704 mJ/cm² με 1 έως 10 παλμούς. Όπως φαίνεται και παρακάτω, υπάρχει συσσώρευση της παραμόρφωσης που αυξάνεται με την αύξηση του αριθμού των παλμών.



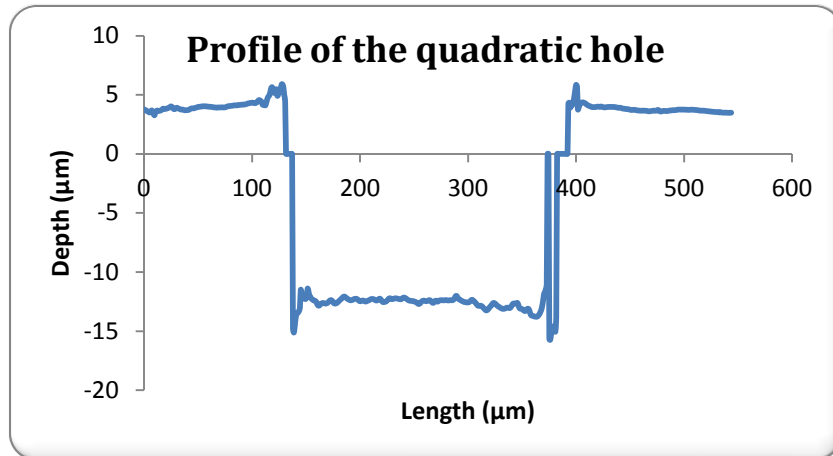
Γράφημα 3: Εξέλιξη της παραμόρφωσης με διαδοχική αύξηση των παλμών

9.2.2. Σύγκριση μεταξύ του προφίλ βάθους ενός κυκλικού και ενός τετραγωνικού ανοίγματος

Ένα κυκλικό άνοιγμα διαμέτρου 500 μm και ένα τετραγωνικό πλευράς 250 μm ακτινοβολήθηκαν με 100 παλμούς, 300mJ/cm² και 50 Hz. Παρακάτω παρουσιάζονται το προφίλ της επιφάνειας για την κυκλική και τετραγωνική κοιλότητα. Το βάθος (στο κέντρο της κοιλότητας) μετρήθηκε γύρω στα 11.7 μm για την κυκλική και γύρω στα 16.6 μm για την τετραγωνική κοιλότητα.



Γράφημα 4: Προφίλ κυκλικής τρύπας

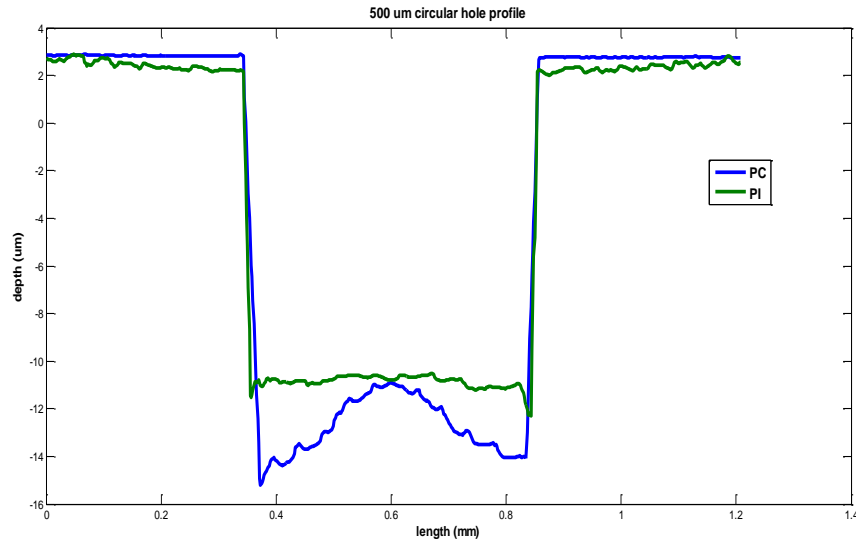


Εικόνα 5: Προφίλ τετραγωνικής τρύπας

Η διαφορά μεταξύ των δύο βαθών και των δύο τοπογραφιών είναι αξιοσημείωτη. Σε αυτό το σημείο υπάρχουν υποψίες ότι η παραμόρφωση μπορεί να προέρχεται από περιθλάσεις στο σύστημα.

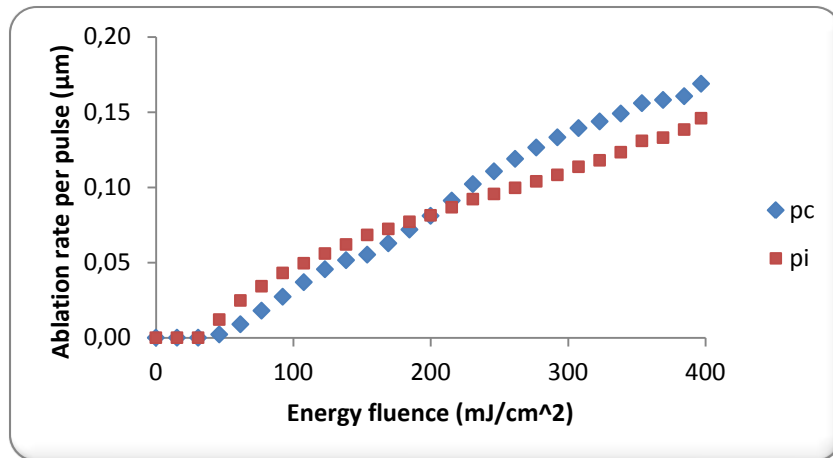
9.2.3. Σύγκριση polycarbonate με polyimide: Καμπύλη αποδόμησης και προφίλ βάθους

Προκείμενου να εξεταστεί αν αυτό το φαινόμενο του φουσκώματος παρατηρείται και σε άλλα υλικά (με σκοπό να εξαχθεί το συμπέρασμα ότι οπτικά φαινόμενα εξηγούν αυτή την παρατήρηση) επιλέχθηκε να ακτινοβοληθεί ένα πολυμερές με κοντινό ενεργό συντελεστή απορρόφησης, το polyimide (πάχος δείγματος: 140 μm). Στην παρακάτω καμπύλη φαίνεται το προφίλ βάθους μιας κυκλικής τρύπας διαμέτρου 500 μm που έχει ακτινοβοληθεί κάτω από τις ίδιες πειραματικές συνθήκες για το polyimide και το polycarbonate (400 mJ/cm², 50Hz, 100 παλμοί).



Γράφημα 6: Προφίλ polycarbonate (μπλε) και polyimide (πράσινο)

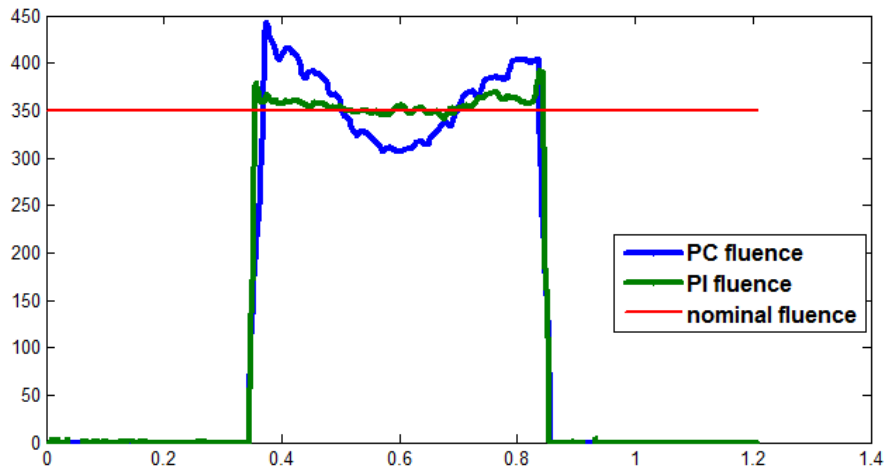
Στη συνέχεια κατασκευάστηκε η καμπύλη αποδόμησης (ρυθμός αποδόμησης vs ροή ακτινοβολίας) για τα δύο υλικά. Για την κατασκευή της χρησιμοποιήθηκε μια grayscale μάσκα από την οποία επιλέχθηκαν σημεία που είχαν από 0 έως 100% μετάδοση ακτινοβολίας. Αυτή η μάσκα ακτινοβολήθηκε και στα δύο υλικά με 400 mJ κάτω από τις ίδιες πειραματικές συνθήκες (50Hz, 100 παλμοί) και λήφθηκαν τα παρακάτω σημεία που φαίνονται στην καμπύλη.



Εικόνα 7: Καμπύλες αποδόμησης για polycarbonate και polyimide

Έπειτα, με χρήση της matlab, έγινε μια πολυωνυμική προσαρμογή 5^{ης} τάξης στα πειραματικά σημεία. Αντιστρόφως, κατά έναν ιδανικό τρόπο, από τα προφίλ βάθους, μέσω των καμπυλών

αποδόμησης, κατασκευάστηκε η παρακάτω καμπύλη που συνδέει τη ροή ακτινοβολίας που δέχθηκε κάθε σημείο κατά μήκος της κοιλότητας.

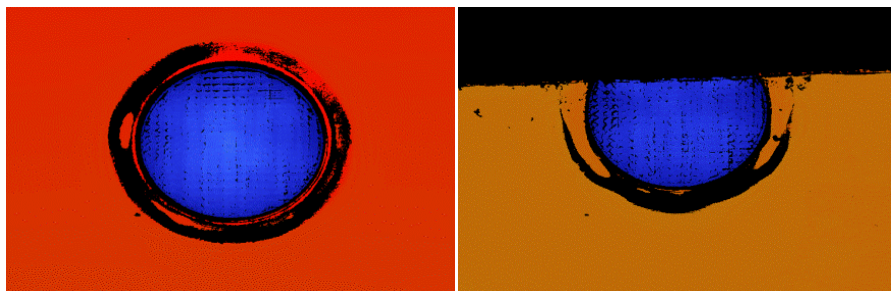


Εικόνα 8: Προφίλ ροής ενέργειας για polycarbonate και polyimide

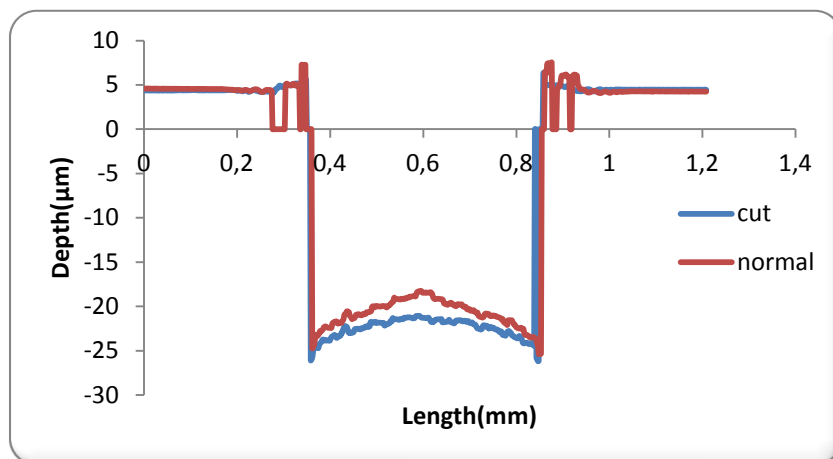
Όπως μπορεί να παρατηρηθεί από το παραπάνω γράφημα, φαίνεται ότι η κατανομή ενέργειας διαφέρει από την ονομαστική κατανομή και για τα δύο υλικά. Αν και θεωρητικά θα έπρεπε οι τρεις καμπύλες να ταυτίζονται, παρατηρείται ότι οι διαφορές στην ενέργεια στις δύο καμπύλες είναι σημαντικές. Αυτό ενισχύει την άποψη ότι το φαινόμενο του φουσκώματος δεν οφείλεται σε οπτικές ιδιότητες του συστήματος αλλά και σε ιδιότητες υλικών.

9.2.4. Μερική μετακίνηση της κυκλικής τρύπας έξω από το υπόστρωμα

Στο παρακάτω πείραμα μια κυκλική τρύπα διαμέτρου 500 μm χαραχτηκε στην άκρη του δείγματος, έτσι ώστε ένα τμήμα της ακτινοβολίας του laser να κατευθύνεται εκτός υλικού και να δημιουργηθεί η δομή που φαίνεται παρακάτω δεξιά. Αυτή συγκρίθηκε με τη δομή που φαίνεται παρακάτω αριστερά. Και οι δύο δομές παράχθηκαν κάτω από τις ίδιες πειραματικές συνθήκες.



Το προφίλ βάθους των δύο παραπάνω κοιλοτήτων φαίνεται παρακάτω. Παρατηρούμε ότι η δομή που παράγεται στην άκρη του δείγματος έχει μικρότερο φούσκωμα και λιγότερη παραμόρφωση από την κανονική δομή.



Γράφημα 9: Προφίλ μετατοπισμένης και πάνω στο υπόστρωμα τρύπας

9.2.5. Συζήτηση

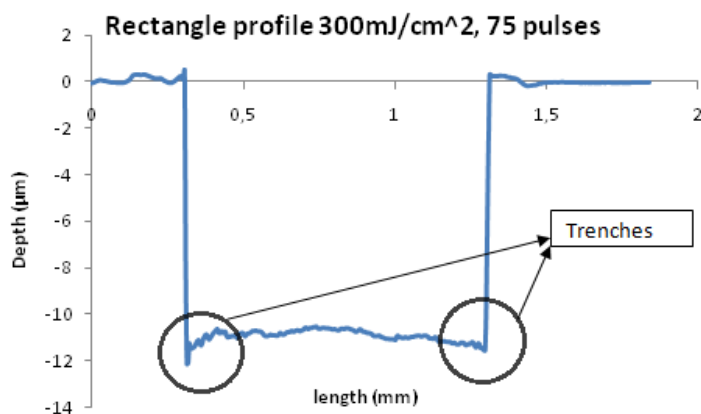
Από τα αρχικά πειράματα φάνηκε ότι η παραμόρφωση με το φούσκωμα προέρχεται από κάποιο οπτικό φαινόμενο όπως η περίθλαση που συμβαίνει στο σύστημα. Στη συνέχεια, όμως, από τη σύγκριση των δύο πολυμερών παρατηρείται ότι και οι ιδιότητες των υλικών παίζουν ρόλο. Επιπλέον, από το προηγούμενο πείραμα συμπεραίνουμε ότι και η εκτόνωση του νέφους μπορεί να παίζει κάποιο ρόλο. Πιθανότατα στην περίπτωση που μέρος της μικροδομής βρίσκεται εκτός του υποστρώματος, δημιουργείται και άλλη μια διέξοδο για το νέφος εκτός από τον κατακόρυφο δρόμο, στα πλάγια του υλικού. Έτσι μια διαφορετική εξάπλωση και εκτόνωση του νέφους μπορεί να οδηγήσει σε ασθενέστερο φαινόμενο ασπίδας, λιγότερη εξασθένηση της ακτινοβολίας και άρα μεγαλύτερο βάθος στη δομή.

Μία υπόθεση για την εξήγηση αυτού του φαινομένου μπορεί να είναι όντως κάποια οπτικά φαινόμενα που λαμβάνουν χώρα στο σύστημα. Πάραυτα, αυτά τα φαινόμενα δεν γίνονται αντιληπτά στο polyimide, γιατί πιθανότατα στην περίπτωση του polyimide εφαρμόζεται ένα μοντέλο που περιλαμβάνει περισσότερο θερμικούς μηχανισμούς από ότι φωτοχημικούς. Μια δεύτερη πιο πιθανή υπόθεση σχετίζεται με την εκτόνωση του νέφους και την εναπόθεση των θραυσμάτων. Το polyimide θεωρείται ότι δεν έχει θερμοκρασίας τήξης και εξαχνώνεται απευθείας σε αντίθεση με το polycarbonate. Έτσι, στην περίπτωση του polycarbonate, μπορεί να υπάρχει

κάποια επανεστεροποίηση και επανατοποθέτηση των θραυσμάτων μέσα στην κοιλότητα. Εάν όντως αυτή η παραμόρφωση οφείλεται στην επαναπόθεση των θραυσμάτων, τότε το σχήμα του νέφους θα παίζει ρόλο στη διαμόρφωση του σχήματος του πυθμένα. Σε αυτή την περίπτωση, ένα πείραμα σε διαφορετικό περιβάλλον από το ατμοσφαιρικό π.χ. στο He που έχει παρατηρηθεί ότι το νέφος έχει διαφορετικό σχήμα θα ήταν χρήσιμο για να δειχθεί αν η τοπολογία της επιφάνειας θα αλλάξει. Αν η μορφολογία της παραμόρφωσης αλλάξει, τότε θα ισχυροποιηθεί η προηγούμενη υπόθεση.

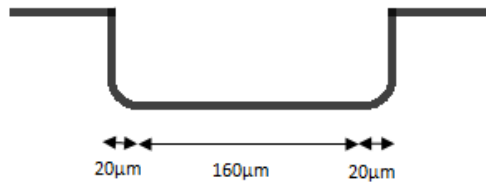
9.3. Χαντάκια

Ο χαρακτηρισμός αυτού του είδους της παραμόρφωσης είναι ιδιαίτερα δύσκολος λόγω των μετρήσεων μη ακριβείας στις άκρες των κοιλοτήτων. Η παραμόρφωση αυτή εμφανίστηκε και σε κυκλικές και ορθογωνικές τοπολογίες.

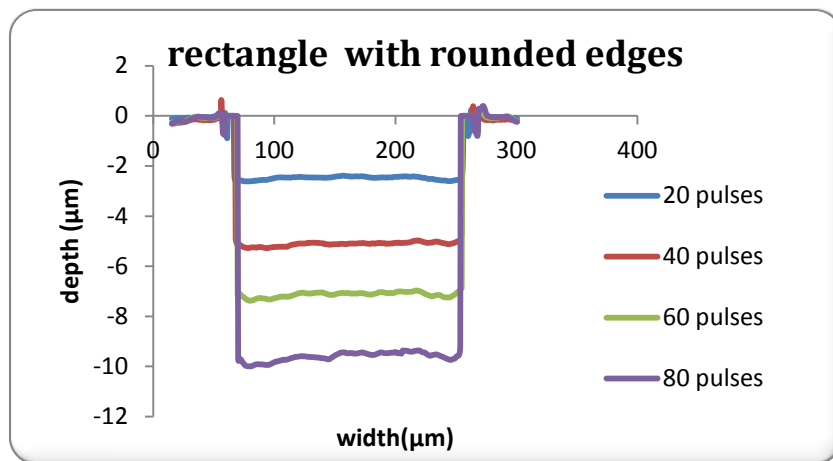


9.3.1. Χρήση ορθογωνικής μάσκας με grayscale άκρα

Σε αυτό το πείραμα χρησιμοποιήθηκε ένα ορθογωνικό άνοιγμα (200µm πλάτος x 400µm μήκος) του οποίου οι άκρες (20µm) έχουν λιγότερο από 100% μετάδοση. Η προβλεπόμενη τοπολογία είναι η παρακάτω:



Το πειραματικό αποτέλεσμα όμως δε συμπίπτει με το προηγούμενο σχήμα. Παρόλα αυτά, από το παρακάτω γράφημα φαίνεται ένας τρόπος αντιστάθμισης της παραμόρφωσης των χαντακιών.



Γράφημα 10: Προφίλ ορθογωνίου με εξομαλυμένες άκρες

9.3.2. Συζήτηση

Τα χαντάκια σε μερικές περιπτώσεις προκαλούνται από φαινόμενα περίθλασης και μπορούν να προσομοιωθούν ικανοποιητικά, αλλά σε άλλες περιπτώσεις το φαινόμενο της περίθλασης από μόνο του δεν αρκεί για να εξηγήσει αυτή την παραμόρφωση. Σε αυτές τις περιπτώσεις η εξήγηση με την ακτινοβολία που ανακλάται στα τοιχώματα και συνεισφέρει σε μεγαλύτερο ρυθμό αποδόμησης κοντά στα άκρα φαίνεται καταλληλότερη.

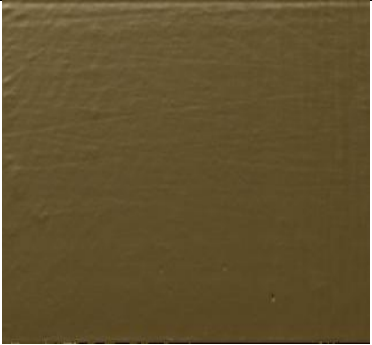

Από το προηγούμενο πείραμα, φάνηκε ότι, εάν αυτή η παραμόρφωση μπορέσει να γίνει προβλέψιμη και αναπαράξιμη, η προσθήκη ενός κατάλληλου χαρακτηριστικού grayscale στην μάσκα στο αρχικό σχέδιο μπορεί να την αντισταθμίσει.

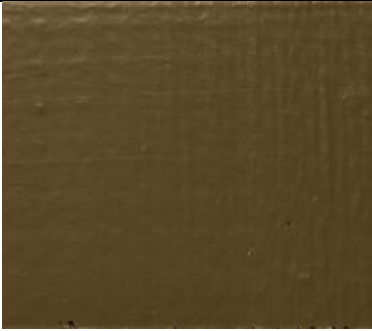




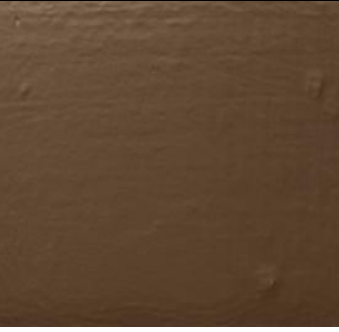



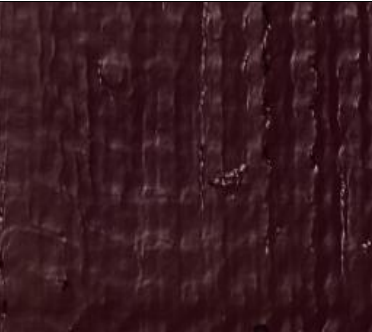

9.4. Μείωση τραχύτητας με μέθοδο σάρωσης

Στο παρακάτω πείραμα χρησιμοποιήθηκε η μέθοδος σάρωσης που περιγράφηκε προηγουμένως για να μειωθεί η τραχύτητα κατά της διαδικασία της αποδόμησης και συγκρίθηκε με την απλή μέθοδο step and repeat. Το μήκος αναφοράς για να γίνει ο διαχωρισμός της τραχύτητας θεωρήθηκε ίσο με 13 μm . Οι παραμορφώσεις με μέγεθος πάνω από 13 μm δεν συνυπολογίστηκαν στον καθορισμό της rms τιμής της τραχύτητας.

Χρησιμοποιήθηκε μια ορθογωνική μάσκα (πλευρά στον x άξονα: 2mm, πλευρά στον y άξονα: 400 μm). Η μετατόπιση του x άξονα ήταν $\Delta x=0.1$ και του y $\Delta y=0.02$. Οι μικροδομές που δημιουργήθηκαν κάτω από τις ίδιες πειραματικές συνθήκες (ενέργεια, συχνότητα, παλμοί). Η πρώτη στήλη δείχνει ένα τμήμα της επιφάνειας των μικροδομών που έχει παραχθεί με την μέθοδο step and repeat, ενώ η δεύτερη και τρίτη στήλη δείχνουν τμήμα της επιφάνειας των μικροδομών που έχει παραχθεί με τη μέθοδο σάρωσης για διαφορετικές παραμέτρους.

Η ροή ενέργειας που χρησιμοποιήθηκε στα επόμενα πειράματα ήταν 400 mJ. Όλα τα δείγματα ακτινοβολήθηκαν με 50 Hz. Στη δεύτερη στήλη χρησιμοποιήθηκαν 2 loops, ενώ στην τρίτη 8 loops.

	Step and repeat	Synchronized scanning 2 loops	Synchronized scanning 8 loops
20 pulses	 Rq=14 nm	 Rq=12 nm	

40 pulses	 <p data-bbox="347 548 483 583">Rq=21 nm</p>	 <p data-bbox="753 548 889 583">Rq=15 nm</p>	 <p data-bbox="1159 548 1295 583">Rq=11 nm</p>
80 pulses	 <p data-bbox="347 974 483 1010">Rq=42 nm</p>	 <p data-bbox="753 974 889 1010">Rq=13 nm</p>	 <p data-bbox="1159 974 1295 1010">Rq=15 nm</p>
160 pulses	 <p data-bbox="347 1400 483 1436">Rq=57 nm</p>	 <p data-bbox="753 1400 889 1436">Rq=22 nm</p>	 <p data-bbox="1159 1400 1295 1436">Rq=18 nm</p>
200 pulses	 <p data-bbox="347 1827 483 1862">Rq=66 nm</p>	 <p data-bbox="753 1827 889 1862">Rq=30 nm</p>	

9.4.1. Συζήτηση

Από τα πειράματα με τη μέθοδο σάρωσης, μπορεί να διαπιστωθεί ότι γενικά μειώνεται η τραχύτητα και βελτιώνεται η ποιότητα της επιφάνειας. Βέβαια φαίνεται ότι η βελτίωση είναι μεγαλύτερη για περισσότερους παλμούς. Πάραυτα, αυτή η μέθοδος δεν βελτιώνει την παραμόρφωση μεγάλης κλίμακας της μικροδομής. Το επόμενο βήμα είναι να βρεθούν οι κατάλληλες παράμετροι που βελτιστοποιούν τη μέθοδο σάρωσης, καθώς από τη σύγκριση της δεύτερης και της τρίτης στήλης δε μπορεί να εξαχθεί κάποιο συμπέρασμα.

10. Επίλογος

Στη συγκεκριμένη εργασία εξετάστηκαν τρία είδη παραμορφώσεων μεγάλης κλίμακας και μία μικρής κλίμακας (τραχύτητα) που συμβαίνουν κατά την αποδόμηση του polycarbonate με excimer laser. Έγινε φανερό ότι για την τραχύτητα υπάρχουν προοπτικές βελτίωσης είτε με τη μέθοδο που περιγράφηκε εδώ είτε με μεθόδους που υπάρχουν στη βιβλιογραφία. Εκεί, όμως, που αναδύονται οι μεγαλύτερες προκλήσεις είναι στη βελτίωση των παραμορφώσεων μεγάλης κλίμακας που αφορούν το σχήμα της μικροδομής. Σε αυτόν τον τομέα δεν έχει υπάρχουν ολοκληρωμένες προτάσεις λόγω της τυχαιότητας των παραμορφώσεων καθώς και της ιδιαιτερότητας της κάθε παραμόρφωσης για κάθε διαφορετική περίπτωση. Με την είσοδο, όμως, της τεχνολογίας των grayscale μασκών φαίνεται εφικτό, ότι αν η παραμόρφωση γίνει προβλέψιμη, με την εισαγωγή κάποιου παράγοντα αντιστάθμισης στη μάσκα να μπορεί να βελτιωθεί το τελικό σχήμα.

Contents

Introduction-Goal.....	33
1. Overview of the excimer laser ablation process.....	34
1.1. Introduction-chapter's goal.....	34
1.2. Introduction to pulsed laser micromachining.....	34
1.3. Excimer Laser ablation and applications.....	35
1.4. Principle of excimer laser ablation: A summary of the mechanisms.....	35
1.5. Laser matter interactions: Polymers.....	37
1.5.1 Important aspects of polymers' structure that play role during laser ablation.....	38
1.6. Thermal and photochemical models.....	39
1.7. Beer model for ablation depth prediction in polymers.....	39
1.8. Validity of a pure photochemical model.....	41
1.9. Plume dynamics.....	41
1.9.1. Plume shielding.....	42
1.9.2. Debris from the ablated plume.....	43
1.9.3. Modified Beer's model taking into account the plume.....	43
1.10. Angle dependence of the laser ablation.....	44
1.11.1 Modified Beer's model taking into account the angle dependence.....	44
2. Optics and Mask projection techniques for micromachining.....	45
2.1. Introduction-chapter's goal.....	45
2.2. Concept of mask projection.....	45
2.3. Aspects of beam quality and laser beam profile.....	46
2.3.1. Laser beam profile.....	46
2.3.2. Beam's homogenization.....	47
2.3.3. Telecentricity.....	47
2.4. Mask techniques.....	48
2.4.1. Binary masks.....	48
2.4.1.1. Stationary methods.....	48
2.4.1.2. Scanning methods.....	49
2.4.2 Gray scale masks.....	50
2.4.3 Hybrid masks.....	51
3. Deviations from the expected machined shape of the microstructure.....	52
3.1. Introduction-Chapter's goal.....	52
3.2. Deviations from the expected shape.....	52
3.3. Small scale irregularities (Roughness).....	53
3.3.1. Definition of roughness.....	53
3.3.2. Surface roughness in laser ablation process.....	53
3.3.3. Methods that deal with roughness.....	54
3.3.3.1. Optimization of the machining process.....	54
3.3.3.2. Post processing methods.....	55
3.4. Large scale irregularities.....	55
3.4.1. Trenches.....	55
3.4.2. Tapered sidewalls.....	56
3.4.3. Curved ablated cavity.....	56
3.4.3.1. Dealing with the curved ablated surfaces.....	57

4. Experimental Setup	58
4.1. Excimer M8000 workstation	58
4.2. Excimer workstation components –Description.....	58
4.2.1. Laser unit	58
4.2.2. Optical components.....	59
4.2.3. Software control of the system	62
5. Methods.....	63
5.1. Surface roughness evaluation by filter implementation.....	63
5.2. Introduction to roughness reduction technique with synchronized scanning	66
6. Results and discussion.....	71
6.1. Introduction-Chapter’s goal	71
6.2. Measurements setup	71
<u>Part A: Shape deformation</u>	
A.1. Ablation rate- size of the ablated area.....	72
A.1.1. Experiment with quadratic and circular mask aperture	72
A.1.2. Experiment with circular mask patterns of different diameter&73	
A.1.3. Experiment with rectangular slits	75
A.1.4. Discussion	76
A.2. Formation of surface bump	77
A.2.1. Evolution of the bump shape.....	77
A.2.2 Fluence – number of pulses tradeoff&77	
A.2.3. Formation of the bump for circular holes with different diameter	78
A.2.4. Comparison between the depth profile of circular and square aperture	80
A.2.5. Comparison with another excimer setup	82
A.2.6. Ablation curve of polycarbonate.....	83
A.2.7. Discussion	85
A.2.8. Comparison with a different polymer	85
A.2.9. Cross section of the bump	87
A.2.10. Repetition rate.....	88
A.2.11. Debris deposition	89
A.2.12. Discussion.....	89
A.3.Trenches	90
A.3.1. Experimentation with rectangular mask pattern with rounded edges	91
<u>Part B: Roughness reduction with the synchronized method</u>	
B.1 Experimentation with a large rectangular mask pattern&92	
B.1.1. Energy fluence 400mJ	92
B.1.2. Energy fluence 100mJ	94
B.2. Experimentation with a smaller ellipse.....	96
B.3.Discussion.....	98
7. Conclusions and future perspective.....	99
7.1. Introduction	99
7.2. Shape deformation	99
7.2.1. Tapered sidewalls	99
7.2.2. Curved bump	99
7.2.3. Trenches	100
7.2.4. Ablation rate- Mask area dependence	101
7.3. Roughness reduction	101

7.4. Final word.....	102
Acknowledgements.....	103
References	104
Appendix A: Principle of operation: Excimer laser and veeco interferometer	107
Appendix B: Excimer scripts.....	114
Appendix C: Matlab scripts.....	120
Appendix D: Ablation curve mask.....	123

List of graphs

Graph 6.1: Ablation rate of a “big” square aperture and a “small” circular aperture	73
Graph 6.2: Ablation rate of holes with different diameters.....	74
Graph 6.3: Ablation rate of holes with different diameters scaled to the ablation rate of 500µm hole diameter.....	74
Graph 6.4: Ablation rate for low number of pulses	75
Graph 6.5: Cavity profile of the different width slits that were irradiated by the same parameters	75
Graph 6.6: Evolution of the x axis cavity profile for low number of pulses.....	77
Graph 6.7: Profile for laser fluence- nopulses trade off	78
Graph 6.8: Evolution of the surface profile for a 500µm diameter hole	79
Graph 6.9: Evolution of the surface profile for a 150µm diameter hole	79
Graph 6.10: Surface profile of the circular cavity of 500 µm diameter, 100 pulses, 300 mJ/cm ²	81
Graph 6.11: Surface profile of the quadratic cavity of 250 µm side, 100 pulses, 300 mJ/cm ²	81
Graph 6.12: Topography of the circular topography	81
Graph 6.13: Topography of the quadratic cavity	81
Graph 6.14: Comparison of the used setup (red line) with another excimer setup (blue line) for a 500 µm diameter hole	82
Graph 6.15: Comparison of the used setup (red line) with another excimer setup (blue line) for a 400 µm diameter hole	83
Graph 6.16: Ablation curve of polycarbonate.....	84
Graph 6.17: Fluence distribution of polycarbonate.....	85
Graph 6.18: ablation curve of pc vs ablation curve of pi.....	86
Graph 6.19: Evolution of the cavity profile of polyimide	86
Graph 6.20: PC vs PI fluence distribution	87
Graph 6.21: Comparison of an ablated cavity on and away from the edge	88
Graph 6.22: Cavity profile for different repetition rates	89
Graph 6.23: Trenches in a rectangular cavity.....	90
Graph 6.24: Trenches in a circular cavity.....	90
Graph 6.25: Expected depth profile of the microstructure’s topology.....	91
Graph 6.26: Depth profile of rectangle with rounded edges pattern.....	91

List of tables

Table 1: Bump’s height for different holes’ diameters.....	80
Table 2: Synchronized scanning versus step and repeat for 400mJ/cm ²	92
Table 3: Synchronized scanning versus step and repeat for 100mJ/cm ²	94
Table 4: Synchronized scanning versus step and repeat for 300mJ/cm ²	96

Introduction – Goal

Excimer laser ablation of polymers is a powerful tool that can have a lot of applications especially in the field of microoptics machining. The quality of the ablated surface of the microstructure plays a critical role in the successful or not goal of the application. During the laser ablation process, a lot of surface irregularities are added to the topography of the ablated material.

This study is an attempt to give a better insight into the surface irregularities that are introduced during the laser ablation process. Most of these irregularities are categorized and examined separately. For one specific category of irregularities which is roughness, a method to evaluate it (in a quantitatively way) and another method to reduce this irregularity during the laser ablation process is developed.

The first and second chapter is a literature review about the excimer laser ablation process for polymers and the most popular ablation techniques used. Chapter 1 deals with material laser interactions aspects, whereas chapter 2 deals with the laser irradiation distribution and the techniques that are used to acquire a certain 2d or 3d pattern on the ablated material. In chapter 3 various surface irregularities are introduced and categorized into large scale and small scale irregularities, with respect to the length scale. Large scale irregularities are subdivided to tapered sidewalls, trenches and curved bottoms. Small scale irregularity is considered the well known roughness. Continuously, in chapter 4 the experimental setup of the excimer micromachining station is described. In chapter 5, a method for the evaluation of the surface roughness is described as well as a method for reducing the roughness during the ablation process.

Chapter 6 is an overview of the experimental results. Part A contains all the results related to the large scale irregularities as well as an attempt to determine the correlation between the ablation rate and the size of the ablated pattern. In part B of the chapter the roughness reduction method is examined and compared to the usual step and repeat process.

Finally in the last chapter, chapter 7, some conclusions are drawn and suggestions for future experiments are made.

Chapter 1: Overview of the excimer laser ablation process

1.1. Introduction-chapter's goal

Excimer laser ablation is a very complex process that combines a wide range of physical and chemical phenomena. There have been proposed several models for the simulation of the ablation process, but their implementation is limited to very specific experimental conditions and materials.

In this chapter, there is an attempt to summarize the most basic phenomena that happen during the laser ablation process and parameters that affect the process and consequently the final result. The former understanding of these phenomena will lead to a better understanding and insight into the procedures that determine the final ablated shape and provoke unwanted artefacts.

1.2. Introduction to pulsed laser micromachining

Pulsed laser micromachining has emerged as a powerful tool in scientific and industrial applications where the need for high aspect ratio features and accurate depth control is not met by conventional patterning techniques. Laser micromachining is based on the removal of material with short but intense laser pulses. Specific patterns, surface patterns or 3D structures, can be achieved by controlling motion of parts or mask image projection. In general, typical feature sizes are in the order of micrometer.

A key advantage of laser micromachining over other conventional patterning or etching techniques is the ability to remove materials ranging from ceramics and metals to semiconductors and polymers without the need to change tooling or chemical processing. Typical applications include drilling through vias, ink jet printer nozzle drilling, microscopic channels, direct-write patterning, surface cleaning, and retexturing. More recent developments in microelectromechanical systems (MEMS) fabrication have used ultraviolet (UV) laser micromachining to locally remove a polymer sacrificial layer in order to release the desired feature without the need for additional wet chemical processing.

Laser micromachining is a contactless process. It will not damage material surface except the pile-up effects for metal materials, debris redeposition for polymers and cracks due to additional

heating stress. But those effects can be avoided by some pre-process, post-process and deliberately setting machining conditions. The laser micromachining can be operated under atmospheric condition and at room temperature. Due to the contactless characteristics, there is no tool wearing in laser micromachining like conventional machining methods. Also laser machining is suitable for rapid prototyping even with complex geometric patterns because of its flexibility.

Pulsed laser micromachining forms an integral part of many micro-fabrication and manufacturing processes and enables a large degree of flexibility in materials processing by introducing a variety of parameters to control the roughness and depth of the micromachined structures. Examples of these parameters include incident laser fluence, position of focal plane, laser spot size and translation distance between subsequent laser pulses [1][2][3].

1.3. Excimer Laser ablation and applications

In the last decade, excimer laser ablation acquired the reputation of being a reliable technology for the fabrication of microstructures. This non resist technique does not require clean-room facilities, can be applied on a broad range of materials and is potentially fast since it allows parallel microstructuring by means of mask patterns. This means that the technique is suited both for prototyping and for fabricating microparts in small numbers, or for applications where conventional tools like mechanical drilling lack the necessary accuracy. Additionally, this fabrication technique can be applied for non contact precision tooling purposes in one of the last fabrication steps or in the post-processing of heterogeneously assembled opto-electronic or photonic components. In the microlens fabrication industry, the major advance of this direct writing technique lies in the potential to fabricate microlenses with characteristics that can be tailored for every lens individually [4].

1.4. Principle of excimer laser ablation: A summary of the mechanisms

Laser ablation is the removal of material from a substrate by direct absorption of laser energy. The onset of ablation occurs above a threshold fluence, which will depend on the absorption mechanism, particular material properties, microstructure, morphology, the presence of defects, and on laser parameters such as wavelength and pulse duration. Typical threshold fluences for metals are between 1 and 10 J/cm², for inorganic insulators between 0.5 and 2 J/cm², and for organic materials between 0.1 and 1 J/cm². With multiple pulses, the ablation thresholds may decrease due to accumulation of defects. Above the ablation threshold, thickness or volume of material removed per pulse typically shows a logarithmic increase with fluence according to the Beer–Lambert law.

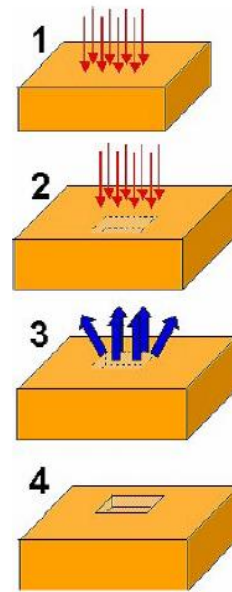


Figure 2.1: Excimer laser ablation process steps: 1) Irradiation of the material with laser pulse, 2) pulse energy is absorbed locally, 3) ejection of material particles, 4) microhole is realized [5]

A variety of mechanisms for material removal may be active during laser ablation depending on the particular material system and laser processing parameters such as wavelength, fluence, and pulse length. At low fluences, photothermal mechanisms for ablation include material evaporation and sublimation. For multicomponent systems, the more volatile species may be depleted more rapidly, changing the chemical composition of the remaining material. With higher fluence, heterogeneous nucleation of vapor bubbles leads to normal boiling. If material heating is sufficiently rapid for the material to approach its thermodynamic critical temperature, rapid homogenous nucleation and expansion of vapor bubbles lead to explosive boiling (phase explosion) carrying off solid and liquid material fragments. These thermal mechanisms can be understood as thermodynamic phase changes in response to the high temperatures. When the excitation time is shorter than the thermalization time in the material, non-thermal, photochemical ablation mechanisms can occur. For instance, with ultrafast pulses, direct ionization and the formation of dense electron-hole plasmas can lead to thermal phase transformations, direct bond-breaking and explosive disintegration of the lattice through electronic repulsion (Coulomb explosion). In certain non metals such as polymers and biological materials with relatively long thermalization times, photochemical ablation can still occur with short wavelength nanosecond lasers, producing well defined ablated regions with small HAZs (Heat Affected Zones). In all cases, material removal is accompanied by a highly directed plume

ejected from the irradiated zone. The dense vapor plume may contain solid and liquid clusters of material. At high intensities, a significant fraction of the species may become ionized, producing plasma. Also, with pulses longer than ps, interaction of the laser light with the plume may be significant. The plume can absorb and scatter radiation, changing the actual flux received by the surface. Recoil from the plume can generate shockwaves in the material, causing plastic deformation and work hardening. The recoil can also cause further expulsion of any remaining molten material as well as initiate shock waves. Resolidification of expelled liquid and condensation of plume material into thin films and clusters of nanoparticles can alter the topography at the rim and surrounding areas of the ablated region. During ns ablation, shielding of the surface by the ejected ablation plume can reduce the amount of energy absorbed by the material. Material responses often involve a combination of ablation, surface melting, and thermally activated processes, which can lead to cumulative changes in the material's surface texture, morphology, and chemistry. For instance, residual heat left after ablating material from a surface can lead to further melting or other thermally activated processes in the remaining surface and surrounding volume of material [6].

1.5. Laser matter interactions: Polymers

Polymers offer low ablation thresholds (0.01-0.5 J/cm²), high quality edge definition and surface finish, and there is little or no evidence of thermal damage to the surrounding material. The typical bonds in their molecular chains feature bond energies which are in the same range as the excimer photon energies. This property is responsible for their high absorption coefficients at UV wavelengths and the 'cold ablation' phenomenon: the absorbed photons excite electronic states in certain organic bonds and relaxation from the excited state can occur via direct dissociation. In practice the ablation process always features thermal and non-thermal material dissociation and evaporation [7]. For these reasons, polymers form a very eligible group for the excimer laser ablation process.

1.5.1. Important aspects of polymers' structure that play role during laser ablation

Polymers are macromolecules, which are synthesized from one or more different types of polymerization, i.e., radical or ionic polymerization, polycondensation, polyaddition, and special cases such as copolymerization. To start the polymerization reaction, starters have to be applied in many cases, e.g. molecules that form a radical upon reaction that is initiated by temperature or light or even complex initiators and enzymes. The polymerization type has a direct influence on the characteristics of the polymer, e.g., molecular weight and distribution, impurities, polymer structure (tacticity), or molecular form, and on decomposition mechanism. The molecular weight, M_w , of the polymer has a direct influence on the state of the polymer, i.e., low molecular weight polymers may still be liquids, while high molecular weight polymers are solid, which may even be insoluble in all solvents if the molecular weight is too high. The M_w influences subsequently the viscosity of the polymer (in the melt or solution), the glass transition temperature, T_g which is the temperature at which the polymer changes from the glass to rubber state, and possibly the melting and decomposition temperature. The M_w of a polymer is not one well defined number, but a range of molecular weights is obtained from the synthesis, and normally an average is quoted. The polymer synthesis and structure of the monomer have a direct influence on the chain regularity/conformation of the polymer, which is also called tacticity. A polymer can have an atactic (random), iso or syndiotactic structure, which again influences properties such as the T_g . Another aspect that is specifically important for the photon-polymer interactions is the possibility of the polymers to be partially crystalline, which results in light scattering (not absorption) in the polymer. Finally, it is also necessary to consider that most polymers cannot be vaporized (sublimed) intact and that many do not have a melting point prior to decomposition, which is the case for cross-linked or many polyimides [8].

Polymers that decompose into fragments are for example polyimides (figure 2) or polycarbonates (figure 3). These polymers show in the case of decomposition (thermally or photochemically) a tendency for a pronounced fragmentation into various small molecules. [8]

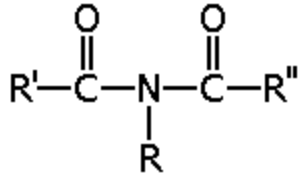


Figure 1.3: monomer of polyimide

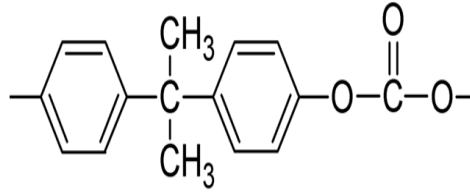


Figure 1.4: monomer of polycarbonate

1.6. Thermal and photochemical models

The physical and chemical mechanisms involved in the UV laser ablation of polymers are still under discussion [9]. It is generally agreed that in ns pulses in a primary step the energy of photons is transformed into the energy of electronic excitation. However, subsequent steps in the ablation process may be quite different. Ablation rates are measured by different techniques that yield non-equivalent results, in particular near the threshold fluence for ablation (F_{th}).

Different models are applied for the description of UV-laser ablation of polymers. One can distinguish between the *photochemical models* where electronic excitation results in direct bond breaking (without thermalization) and *photothermal models*, where the bonds are thermally broken. Thermal nature of the ablation process is supported by observation of the Arrhenius tails, the dependence of the ablation rate and threshold on the laser pulse repetition rate and pulse length. For *photophysical models* both thermal and non-thermal features are important.

From another perspective, the present models can be subdivided into volume and surface models. With surface models the processes responsible for material removal take place only within several monolayers from the surface. As a result, the velocity of the interface between the gaseous and condensed phase depends explicitly only on the surface temperature or laser-light intensity. With volume models, the processes, which lead to the decomposition of material, take place within the bulk material [10].

1.7. Beer model for ablation depth prediction in polymers

Depending on the laser pulse parameters and the material properties, photochemical and photothermal ablation mechanisms can be distinguished. In the first case, the energy of the photons is high enough to cause direct bond breaking, causing the ablation of the material. In the

second case, laser photons rapidly heat a certain amount of material up to the point where thermal processes result in the decomposition and ejection of material. In practice, both these primary processes are responsible for laser ablation. If, as in most polymers, the thermal diffusion length is very small compared to the absorption length of the laser light, the extent of material excitation is mainly determined by the optical absorption of the laser photons. This leads to a commonly used model for the ablation rate based on Beer's law [11].

$$d(F) = \frac{1}{a_{eff}} \ln \left[\frac{F}{F_{th}} \right] \quad (1.1)$$

The two main parameters that describe polymer ablation are the ablation rate $d(F)$ and the ablation threshold fluence F_{th} , which is defined as the minimum fluence where the onset of ablation can be observed. A third important parameter is the effective absorption coefficient, a_{eff} , which yields information on the mechanisms that take place in the ablation process when compared to the linear absorption coefficient, a_{lin} , that is measured on thin un-irradiated polymer films [8].

The surface reflectivity (R) is often ignored as it generally accounts for only a mere 6-10% of the total fluence. Reflectivity can be incorporated in the above Beer's formula as [7]:

$$d(F) = \frac{1}{a_{eff}} \ln \left[(1 - R) \frac{F}{F_{th}} \right] \quad (1.2)$$

The ablation rate $d(F)$ increases logarithmically if the laser fluence F exceeds the threshold fluence F_{th} . The effective optical absorption coefficient describes the modified optical absorption of the utilized polymer under intense laser photon irradiation. Differences in the measured values of their ablation parameters are quite common due to factors such as inconsistent chemical structures in the polymer and dissimilar experimental conditions. The determination of the actual ablation rate is therefore necessary in precision machining.

Also, photon irradiation of materials often changes the material properties, e.g. the absorption caused by the formation of color centers or radiation induced defects etc. This and similar processes influence the ablation rate, which may increase or decrease during the first pulses, resulting in incubation (ablation does not start with the first pulse, but after multiple pulses) and depletion effects [11].

1.8. Validity of a pure photochemical model

The question about the heating of the material during photochemical ablation is very important from the point of view of self-consistency of a pure photochemical model. With VUV photons, we have effective bond scission. However, the energy of the photon is much larger than the energy of the covalent bond. If the excess of energy went to heat, a temperature rise would be high enough to make the applicability of a pure photochemical model questionable [12].

The photochemical model usually fits the data within a very limited range. It is not valid for very low fluencies as ablation rates seem to be a non-linear function of log fluence close the threshold (the so-called Arrhenius tails) and neither applies to substantial fluencies of several J/cm². The model assumes that F_{th} is unambiguously determined by the material properties and laser characteristics. In practice accurate measurement of the threshold is quite difficult due to the Arrhenius tail and is also hindered by incubation and precursor effects [7].

Nevertheless, Beer model remains popular in literature due to its simplicity and the fact that the ablation-fluence curve of a polymer can be characterized by only two parameters. Additionally, for UV lasers which are operated with pulses of nanosecond duration, the ablation is considered a photochemical process with little photothermal phenomenon [2][7].

1.9. Plume dynamics

The ejection of particles from a surface induced by irradiation with a high intensity laser beam leads to the formation of a cloud of ablated material moving rapidly away from the surface. Usually, such a laser ablation cloud consists of excited or ground-state neutrals, electrons, and ions. An example of a plume as a strongly light emitting cloud growing in all directions, but preferentially along the target normal, is shown below.

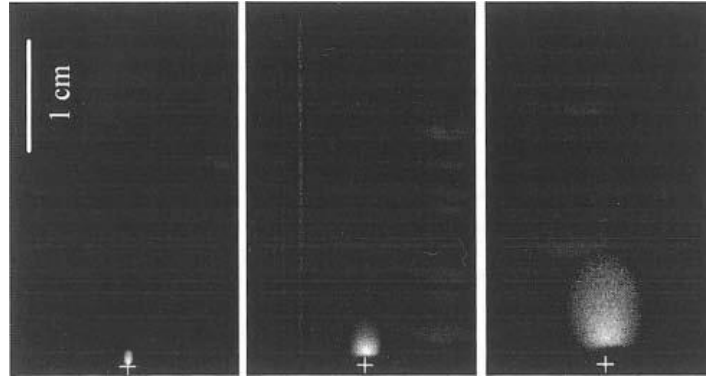


Figure 1.5: Images of the ablation plume produced during laser ablation of a LaMnO₃ target by 20 ns excimer laser pulse at 351 nm with a fluence of 1.5 J/cm² in vacuum [13]

The physical parameters in the plume, that is to say the mass distribution of plasma ejectants, velocity, the angular distribution of the plume species, plume shape, during the expansion from the target surface are under investigation ([14], [15]). Plasma plume expands in all directions but preferentially in normal directions to the surface. This expanding ablated material plasma plume is known as forward peaking [16]. With respect to the velocity, it is commonly accepted that the species travel with a speed ranging from 10^4 to 10^5 cm/s [7].

The complicated interactions between the species in the plume and the interaction between the species and the incident laser light mean that a detailed theoretical or computational treatment has not yet appeared for the comparatively simple case of a plume expanding in vacuum. An even more complex case occurs for a laser ablation process of a solid in a background gas ([17], [18]).

1.9.1. Plume shielding

The scattering and absorption of laser radiation by previously ablated plumes in laser ablation, which is known as the shielding effect, affect dramatically the efficiency of laser ablation process. Since the ejected plume interacts with laser irradiation, it leads to the attenuation of the energy deposited in the material and decreases the ablation rate during subsequent laser pulses.

One of the mechanisms responsible for the shielding effect is formation of the plasma above the irradiated target [20]. Even though the fluencies that are used in many micromachining applications are considered to be below the plasma formation threshold, ionization has been

shown to be present in virtually all laser ablation plumes, even those only slightly above the ablation threshold [19].

There are a lot of models that try to simulate the plume shielding effect ([20], [21]). Although these models are able to explain various aspects of ablation, in most cases they have a rather limited range of validity.

1.9.2. Debris from the ablated plume

Using various chemical and physical techniques, the plume composition has been found to be quite complex, with species ranging from low mass volatile gases to large polymer fragments and, in some cases, carbon rich clusters. Re-deposition of the ablation products on or around the ablation site is commonly observed. The magnitude of this “debris” problem is governed by the specific polymer involved as well as the processing environment (gas, vacuum), ablation fluence, and laser wavelength. The exact spread of debris is determined by the plume expansion dynamics and depends on the beam shape and size, the fluence and ablated depth.

Considerable effort has been directed at reducing the redeposited debris, which is undesirable in many applications. Gas dynamic models have been developed that relate the plume expansion to the re-deposited debris patterns, and the potential benefits of using gas streams for cleanup have been explored. Simple fume extraction techniques do not remove or avoid debris in a satisfactory fashion. There are several ways to counter debris deposition and they can be roughly divided into two categories: either deposition of the particles is prevented during processing or they are removed after finishing the structure [7], [22].

1.9.3. Modified Beer’s model taking into account the plume

Experimental etch rate-fluence plots often differ from the description provided by (1.1). One explanation for this is that the laser beam must propagate through the plume of ablation products that are expelled from the surface and this may have a significantly different mass absorption coefficient to the parent solid polymer. When this is accounted for by attributing different absorption properties to the solid and plume is modified such that:

$$d(F) = \frac{\mu}{\alpha\mu_p} \ln\left\{1 + \mu_p(F - F_{th})/\mu F_{th}\right\} \quad (1.3)$$

Here $\mu=\alpha/\rho$ and $\mu_p=\alpha_p/\rho_p$ are mass absorption coefficients for the solid polymer and plume, respectively. The etch rate per pulse is then dependent on whether the plume is less ($\mu_p < \mu$) or more ($\mu_p > \mu$) absorbing than the solid [22].

1.10. Angle dependence of the laser ablation

Whether variable surface height is machined, the shaping demanded often means the surface presented for ablation lies well off normal incidence. It has generally been assumed that the reduction in ablation rate on inclined surfaces can be accounted for by geometrical $\cos\theta$ reduction in the normal component of the fluence, but there are also some factors that should be taken into account

1.10.1. Modified Beer's model taking into account the angle dependence

Here, in addition to the basic $\cos\theta$ reduction in fluence, other factors influence the etch rate as θ increases. These are the longer beam path in the plume and increasing surface reflection loss, both generally leading to a reduction in the fluence coupled to the surface. Consequently, the following formula results [23]:

$$d(F) = \frac{\mu \cos\theta}{\mu_p \alpha_0} \ln \left[1 + \frac{\mu_p (1-R_\theta) F}{\mu (1-R_0) F_{T0}} - \frac{\mu_p \alpha_0}{\mu \alpha_\theta \cos\theta} \right] \quad (1.4)$$

Where R_θ is the surface reflection coefficient, α_θ is the effective absorption coefficient of the polymer along x for angle of incidence θ and α_0 and R_0 are the equivalent for normal incidence.

Chapter 2: Optics and Mask projection techniques for micromachining

2.1. Introduction-chapter's goal

In the previous chapter the laser material interaction was examined, but there wasn't any mention of the intensity and shape distribution of the laser irradiation that reaches the workpiece.

This chapter's goal is to provide a summarized overview about the profile of the laser irradiation that reaches the workpiece and plays a key role in the determination of the final shape.

For this reason, there is an introduction to the mask techniques that are currently applied for the construction of 3D microstructures and determine the laser beam profile at the workpiece plane. The technique plays a significant role in the quality of the machined microstructure since it can improve or deteriorate it. Furthermore, there is a reference to the raw laser beam intensity distribution and laser optics, which also can affect the final shape due to spatial and temporal inhomogenities.

2.2. Concept of mask projection

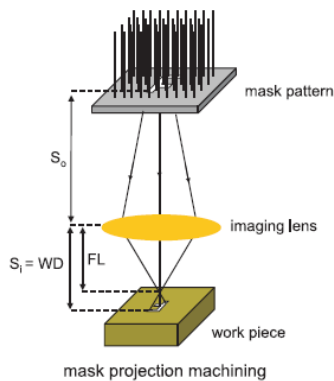


Figure 2.1: Fundamental setup of mask projection

As the beam of excimer lasers is highly multimodal, it does not focus very well. However, its large transversal dimensions make these lasers very suitable for mask imaging or projection purposes. A generic lay-out for a material machining workstation based on mask projection is given in figure beside. A laser beam is used to illuminate a mask consisting of opaque and transparent areas. The incident rays on the transparent parts will be transmitted through the mask, collected by the imaging lens and directed onto the part surface. If the latter is lying in the image plane, the irradiated geometry on the part will be identical to the pattern of the mask except for a constant factor called the demagnification of the system. The positions of the mask, part and lens plane are related by:

$$\frac{1}{S_o} + \frac{1}{S_i} = \frac{1}{FL} \quad (2.1)$$

The ratio S_o/S_i equals the demagnification DM.

Since the image dimensions are scaled with a factor $(DM)^{-1}$ with respect to the mask geometry, the intensity (or fluence) on the workpiece will increase with $(DM)^2$ except for transmission losses that might occur in the optical path [7].

2.3. Aspects of beam quality and laser beam profile

There are many types of lasers with different gases available in the market including high power infrared Nd:YAG and CO₂ lasers which are mainly used in industry, but excimer lasers which emit in the UV range 157-355nm depending on gases, prevail where mask projection techniques are used. For UV lasers which are operated with pulses of nanosecond duration, the ablation is a photochemical process with little photothermal phenomenon, while for high power lasers such as CO₂ lasers, the ablation always happens in both ways. Compared with CO₂ lasers, UV lasers can generate smaller structures due to the smaller wavelength. Another advantage of UV laser is that heat effects are confined in a very limited volume since only part of ablation happens due to photothermal phenomenon and pulse duration is very short.

The parameters regarding to laser include pulse energy (E[mJ]), fluence (F=E/Spot [J/cm²]), intensity (I[W/cm²]), pulse length (η[ns]), repetition rate (f[Hz]), output power (P=fE[W]), wavelength (λ[nm]), and beam quality (M²).

2.3.1. Laser beam profile

One big concern about the laser is the shape and energy profile of output laser beam. The shape and energy profile of laser beam directly determine the shape of etched cavity.

For excimer laser, the shape of the beam is a rectangle and the energy profiles in two directions are different. In one direction the energy profile is normal distribution or like normal distribution. In the other direction, the energy profile can be approximately described as the top-flat function. With this type of energy profile, the laser beam cannot be focused on one small circular spot but a rectangular-like shape with oval on both ends. So, it is suitable to remove material in large areas due its relative large focused beam size [2].

2.3.2. Beam's homogenization

Some homogenous optical devices are utilized to make the energy distribute more evenly and take advantage of both energy profiles. Beam homogenizer is one of those devices. It can change energy profile in a laser beam to a more evenly distribution almost without much energy loss via reducing the standard deviation of laser energy over the beam area. Homogenizers split up the beam and then superimpose them in the mask plane by using optical devices. The homogenized energy profile is very similar to top-flat function, but more evenly distributed with large flat area.

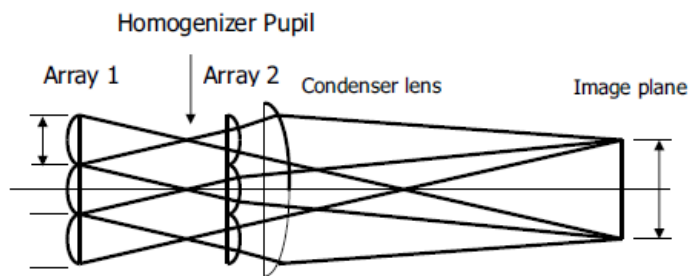


Figure 2.2: Fly's eye homogenizer

A very common homogenizer's setup is the fly's eye configuration. The homogenizer consists of two arrays of microlenses. The first array splits the beam into a large number of sourcelets, each of which is projected onto the mask from a different direction with the aid of the condenser lens. Overlapping different portions of the beam in this way improves the uniformity of the illumination at the mask plane, which is essential for a uniform material removal rate.

2.3.3. Telecentricity

An important aspect of mask imaging systems is telecentricity. A single lens is perfectly capable of imaging a mask pattern on the part surface. As the pattern is drilled into the material, the rays' angle of incidence determines the drilling direction.

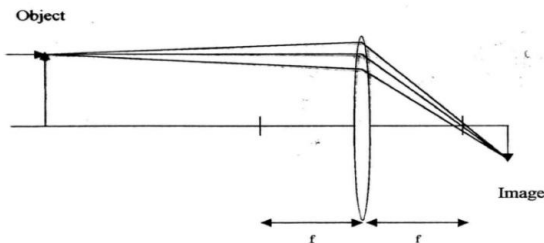


Figure 2.3: Non telecentric setup

Using a single lens for imaging will result in non perpendicular incidence of the rays on the substrate for mask features which are not on the optical axis of the system (figure 7).

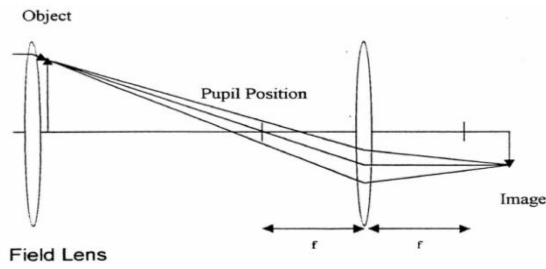


Figure 2.4: Telecentric setup

This behavior is generally not desired and can be solved by inserting a lens that focuses the beam in the focal plane of the projection lens. This second lens is the field lens (figure 8).

2.4. Mask techniques

All 2.5D-machining techniques use specific mask designs. In principle, two basic mask families are employed in 2.5D-processing: the contour or binary mask and the gray scale mask. When projected onto a workpiece, both, along with other parameters, control the machining process of the 2.5D-topographies to be etched. The contour mask defines an area on the workpiece with a homogenous fluence where laser etching takes place. It can be used either at one location or scanned over the workpiece. The gray-scale mask locally controls the transmitted laser fluence onto the workpiece and consequently the local etch rate of the material.

2.4.1. Binary masks

With a standard binary mask (zero or 100% transmission), each laser pulse removes material to the same depth in all exposed regions of the workpiece. Several methods can be used to produce features with variable surface height in such systems.

2.4.1.1. Stationary methods

There are two extensions of the basic process which can enhance the applicability of stationary projection. One involves the lateral motion of the sample in between the production of structures: the laser is fired with a static mask and workpiece to produce a structure; the laser is turned off; the sample is moved laterally in X or Y; the laser is fired again to produce the same structure again. By repeating this procedure, large areas can be covered with

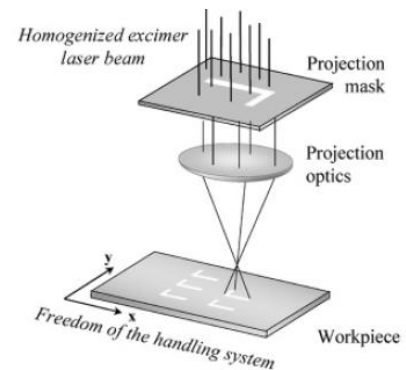


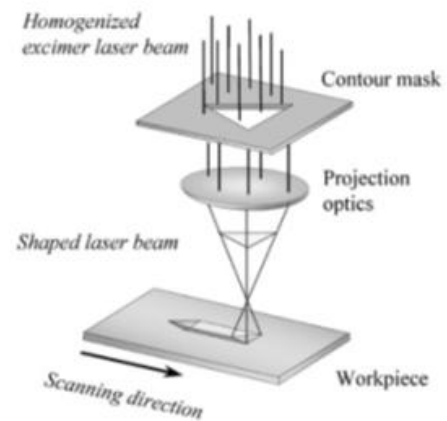
Figure 2.5: Step and repeat processing [6]

the same structure. This technique is called step-and-repeat processing. The second extension of stationary projection involves the positioning of a new mask pattern in between production of the structures: the laser is fired with a static mask and workpiece to produce a structure; the laser is turned off; the mask is moved laterally to position another pattern under the laser beam; the laser is fired again over the same workpiece area to superimpose the new mask pattern over the previous one. This techniques id called indexed mask projection. [24]

2.4.1.2. Scanning methods

If the mask is moved during the firing of the laser, then structures can be produced which have varying depth profiles, thereby introducing simple depth information into the features. This can be achieved by ensuring that an aperture moves across the laser beam in a precisely controlled manner during the laser firing – hence, the static workpiece is exposed to a continually-varying amount of energy across its exposed area which produces a depth gradient in the sample. This technique is also known as mask dragging.

This is one of the most common extensions of the mask projection technique and involves the movement of only the sample during the laser firing. It is usually associated with the production of micro-channels or micro-grooves which may be used in various biomedical or optical applications. The concept of workpiece dragging, as this technique is also often called, involves using a static mask while moving the sample under the laser beam during firing. The laser processing conditions such as fluence and number of shots define the depth of the feature as with all other mask projection methods but the mask shape determines the depth profile of ablated structure. **Figure 2.6: Workpiece dragging [6]**



Therefore, the 2D layout of the channels can be defined by the motion of the workpiece and the cross-sectional profile by the mask shape – since these two aspects can be chosen independently, the technique allows a great deal of diversity in the details of the micro-structures which can be machined. Workpiece dragging is well suited to producing periodic structures over large areas, and has been widely used in the fabrication of structures such as gratings, microchannel arrays and anti-reflection surfaces.

Synchronised image scanning is a variant of the above techniques in which the workpiece is dragged beneath a linear array of mask apertures (the information for the ablation of a specific 3D feature is stored as a linear array on a chrome-on-quartz mask), all of which are illuminated by the laser beam. The laser firing pitch (distance traveled by workpiece between laser pulses) is set equal to the spacing between mask apertures so that each site on the workpiece is exposed to a single pulse with each of the apertures in turn.

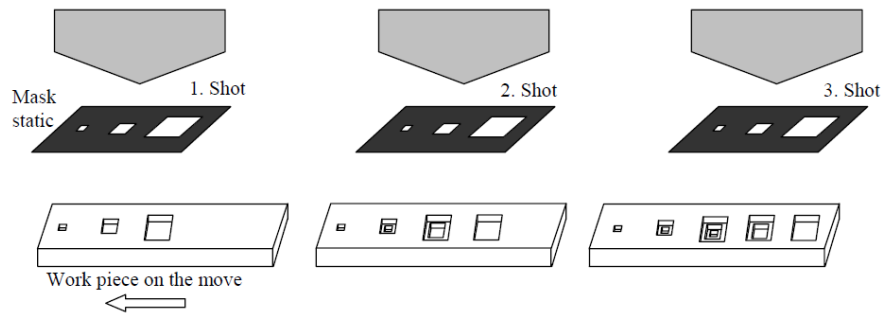


Figure 2.7: Concept of SIS method [33]

SIS offers higher throughput than indexed mask projection by virtue of parallel processing. Also, because each site receives only one pulse with each SIS aperture, the stepping in the surface that arises from using a discrete set of masks can be minimized. The above techniques achieve variable depth by exposing different parts of the workpiece to different numbers of laser pulses. The fluence in the exposed regions is usually independent of position [25], [24].

2.4.2. Gray scale masks

Processes with binary masks are well suited and optimized for producing planar microstructures in a variety of materials, including ceramics and polymers. However the demand for non-planar microstructures in MEMs and lab-on-chip devices, for example microlenses and other micro-optical components or contoured microfluidic channels, requires alternative, non-planar fabrication processes to be developed. Greyscale or half-tone masks are used instead of binary masks and existing equipment and processes can be used to fabricate complex, non-planar structures in a single step.

Laser machining is very flexible in that it machines the workpiece directly so does not require a photosensitive

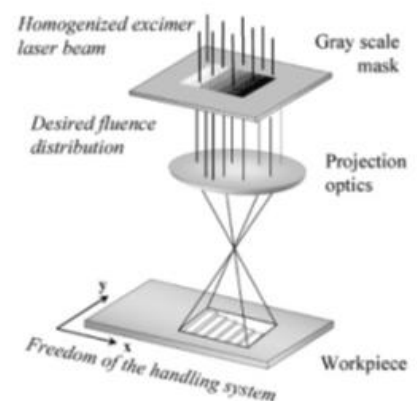


Figure 2.8: Gray scale mask technique

workpiece material such as in photolithography. The critical property of such greyscale masks is that the pixel dimensions are smaller than the resolution limit of the optical exposure system, otherwise the mask pattern will be resolved and conventional planar machining will result [26]. Provided that the pixel structure is not resolved by the projection optics, the mask behaves as an attenuator, with the local transmission depending on the aperture size in each pixel. In this way a conventional binary mask can be made to behave like a continuously variable or gray scale mask. Half-tone ablation can produce a wider range of geometries than mask or workpiece dragging, and is less costly in terms of mask real estate than indexed mask projection. On the other hand, the mask design process is more complex, requiring detailed knowledge of the material ablation characteristics [27].

2.4.3. Hybrid masks

The combination of gray scale masks and synchronized image scanning technique is very promising. The use of linear arrays of grayscale masks has the advantages of parallel processing that the SIS method provides, but also eliminates the step effects at the edges from SIS.

Chapter 3: Deviations from the expected machined shape of the microstructure

3.1. Introduction-Chapter's goal

In this chapter there is an attempt to describe the most severe deviations from the expected machined shape of a microstructure that were observed during the experiments.

3.2. Deviations from the expected shape

Even though laser ablation is a high precision technique and polymers are suitable materials to accomplish a controllable and optimal final result, there are always deviations from the desirable and predicted shape of the final structure of the sample. These deviations may derive from the laser ablation process itself or a deficient mask design (e.g. for grayscale mask design, quantization errors due to small number of different transmission levels). As the mask design is not part of this study, we will focus on the surface irregularities that are taking place during the laser ablation process.

Moreover, as it was mentioned in the previous chapter the material properties of the ablated area and more specifically the laser ablation properties of each polymer play a prominent role in the shape formation of the ablated cavity. For that reason, new polymers ([13], [20]) have been developed to further improve the quality of the ablation process, i.e., to achieve higher ablation rates, lower threshold values and better quality structures. Our study will be limited to polycarbonate because of the specific applications that it is needed.

The purpose of 3D-machining is the generation of the desired topography of the structure but also the retention of a smooth surface. This is particularly important for applications in micro-optics and micro-fluidics. Consequently, a convenient way to deal with the surface irregularities is to classify them with respect to their length scale. Roughness may be considered as a small scale irregularity, whereas the tapered cavity walls instead of perpendicular to the surface or bumps and shape errors may be considered as large scale irregularities.

3.3. Small scale irregularities (Roughness)

3.3.1. Definition of roughness

Roughness relates to the closely-spaced irregularities left on a surface from a production process. Roughness is a measure of the fine, closely spaced, random irregularities of surface texture. Surface texture refers to the locally limited deviations of a surface from the ideal intended geometry of the part.

A way to evaluate roughness quantitatively is to use the root mean square parameter (R_q). R_q is the root mean square average of the roughness profile ordinates and it can be calculated as follows:

$$R_q = \sqrt{\frac{1}{l} \int_0^l Z^2(X) dX} \quad (5.1)$$

where l , X and Z are depicted below:

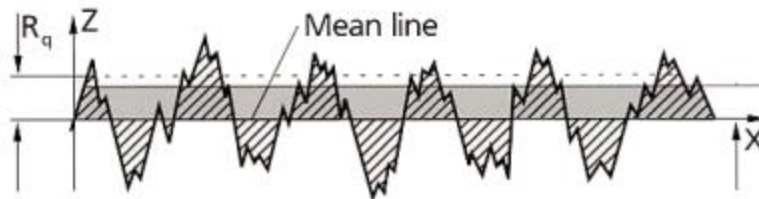


Figure 6: Surface profile measurement

For a digital image, R_q is obtained by squaring each height value in the dataset, then taking the square root of the mean. The digital approximation for the three-dimensional R_q is given by:

$$R_q = \sqrt{\frac{1}{MN} \sum_{i=1}^M \sum_{j=1}^N Z^2(x_i, y_j)} \quad (5.2)$$

3.3.2. Surface roughness in laser ablation process

An analysis of the limiting factors that govern the roughness of an excimer laser ablated polymer surface needs to take account of both material aspects (e.g. intrinsic inhomogeneity, capillary

wave excitation) and optical factors. In general, if the laser pulse hits a surface with a locally varying composition, different ablation depths are unavoidable. Occasional shadow effects, e.g. from re-deposited debris, may lead to the formation of macroscopic cones. In addition, self-organizing microstructures and surface instabilities on laser-ablated polymers lead to the development of surface roughness. The diffracted and reflected light on already ablated structures is also involved in the formation of roughness at the bottom surface [11]. At the optical level it has been proposed that statistical fluctuations in the spatial fluence distribution associated with the highly multi-mode beam of the excimer laser set a fundamental limit. These pulse-to-pulse fluctuations produce a theoretical surface roughness in ablation that scales as $m^{1/2}$ where m is the number of exposure pulses and for deep etching may be expected to produce roughness of hundreds of nanometres. A second more practical limitation relates to random fluence variations in a nominally uniform fluence beam which produce roughness scaling directly as m . These might easily be introduced by optical imperfections in excimer laser beam delivery optics. That 'stationary' fluence variations rather than pulse-to-pulse mode fluctuations are dominant [22].

3.3.3. Methods that deal with roughness

To meet this challenge the laser machining process must be optimized or a tailored post process is needed.

3.3.3.1. Optimization of the machining process

As it was stated above, fluence variations in a nominally uniform fluence beam is a main factor for producing roughness. A simple idea that has been developed is to average out the beam's spatial fluence in the ablated area by irradiating the workpiece from different regions of the laser beam.

Rotation of the sample can average out the slightly uneven laser fluence distribution over the projected area and assure a truly symmetrical surface profile. The center of the mask is aligned with the rotation center of the sample table. Rotating the sample and firing the laser pulse continuously produce a 3D axially symmetrical structure. The profile of the machined structure depends on the design of the mask pattern and machining parameters [29]. This method, as well as an improved version of this method, which is called planetary scanning method [30], is facing

certain constraints such as the machining of axially or circularly symmetrical microstructures only.

3.3.3.2. Post processing methods

To reduce the roughness of microstructured surfaces there are at least three different post processing methods. The first group of techniques uses an additional layer of material for the planarization process. Planarization is based on the reduction of the surface energy of a viscous film applied to the rough surface. In practice, the additional liquid layer is spread over the entire surface and dried afterwards. A second group of techniques uses the reflow of material either by the softening of the material at increased temperatures, or by melting a thin surface layer by pulsed application of energy. A third group of new techniques for reducing the roughness is based on high energy ion bombardment of surfaces. A planarization process reduces the high spatial frequencies by nearly the same amount whether they originate from the desired topology or from the roughness.

3.4. Large scale irregularities

3.4.1. Trenches

A very common deformation is the bad quality shape of the surface near the edges. As it can be observed, the area near the sidewalls is deeper and a structure that seems like a trench is formed. This “trench” effect is quite observable in every single experiment of this study. This feature has been observed in other studies also [31]. It was observed also as a simulation result of a model that predicts the topology formation after laser ablation [31]. It is described as a circular trench making an outer ring at the bottom of the hole and an island of uncut material that remains in the center of the hole. The explanation of the formation of this feature is claimed to be the reflection of light from the steep walls of the hole which results in an increased cutting speed. The light hits the substrate’s steep walls and is mostly reflected down into the bottom of the hole. This light “piles up” at the bottom adjacent to the wall, and consequently over cuts this region by a small amount. An explanation involving light diffraction has also been put forward to explain these features, but there are several reasons to put into question this argument [31]. The “reflection from walls” approach presupposes a non perpendicular wall, something that is common case in polymers’ laser ablation. At this point a further insight to the tapered sidewalls is needed.

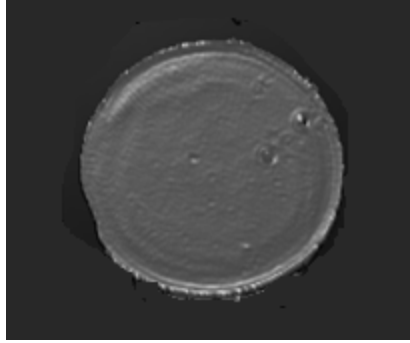


Figure 3.1: Top view of an ablated circular hole

3.4.2. Tapered sidewalls

Although the cavity wall angle of the ablated polymer should be perpendicular to the surface, it has some slope. Initiation of finite wall angles in real systems is a result of the blurring of the edge due to effects which may include diffraction, imperfections in the optical imaging system, heating, and possibly mechanical jitter [31], so that the wall angle of the ablated site is dependent upon many factors. The most important of them are the incident fluence, the numerical aperture of the projection system, the material composition and the laser wavelength.

For some materials, at small fluences the hole tapers inwards (positive taper) due to diffraction effects at the entrance. At higher fluences the taper angle reduces until the walls undercut the surface (negative taper). Since the NA of the objective is high, some of the light rays forming the image of the aperture are incident upon the surface at high angles. As machining proceeds these rays can ablate the material provided they do not suffer excess attenuation due to diffraction at the ablation site entrance i.e. provided the fluence is high enough. The path of these rays through the material causes undercutting [32].

For polycarbonate, it has been shown that the wall angle (negative taper) decreases with the increase of fluence [28] and depends on the number of the pulses [34].

3.4.3. Curved ablated cavity

When binary masks are used, the bottom of the ablated cavity is intended to be perfectly flat. Nonetheless, the ideal flat shape is never attained experimentally. Instead of a flat surface, there was observed a curved surface bottom in many cases (figure 3.2). This curved bottom is much more pronounced in circular ablated holes than rectangular and can be characterized as a bump.

To the best of our knowledge, this bump is not mentioned in literature with regard to polycarbonate, to this fluence range ($\sim 100\text{J}/\text{cm}^2$ - $800\text{J}/\text{cm}^2$) and to this depth range (several to tens of microns). According to [35], below the fluence threshold, the formation of a nm range hump is observable for polyimide.

For rectangular ablated cavities, this type of bump wasn't observed, but other type of surface irregularities were observed, not such dramatic, like curved surface bottom.

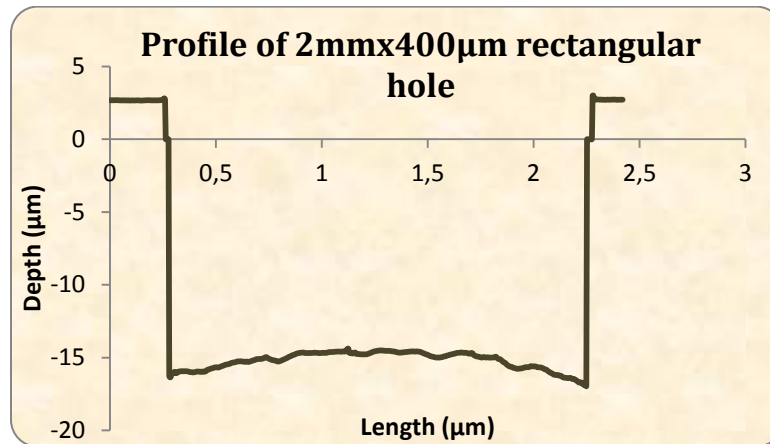


Figure 3.2: Profile of the long axis of an ablated rectangular hole

3.4.3.1. Dealing with the curved ablated surfaces

For this kind of surface irregularities there is no common treatment, since the shape error, most of the times, isn't predictable and depends on factors that are questionable till now. So, to deal with such a shape error, initially, there is a need for further study and better prediction of the surface abnormality. With the introduction of grayscale masks in laser ablation, new potential has been appeared. If the shape error is predictable and reproducible, it can be incorporated to the grayscale mask design in a way that the final structure won't contain it.

Chapter 4: Experimental Setup

4.1. Excimer M8000 workstation

The machining aspect of this work was performed using a KrF excimer laser system Series M8000 (Exitech Limited, UK) equipped with a LPX210 (Lambda Physik, Germany) laser source for 248 nm exposure and 20 ns pulse duration. The beam delivery system contained beam shaping and homogenization optics to create a uniform, square beam at the plane of a mask (chrome-on-quartz mask). All the experiments were achieved at ambient air. The irradiated polymer that was used was polycarbonate (thickness: 1mm).

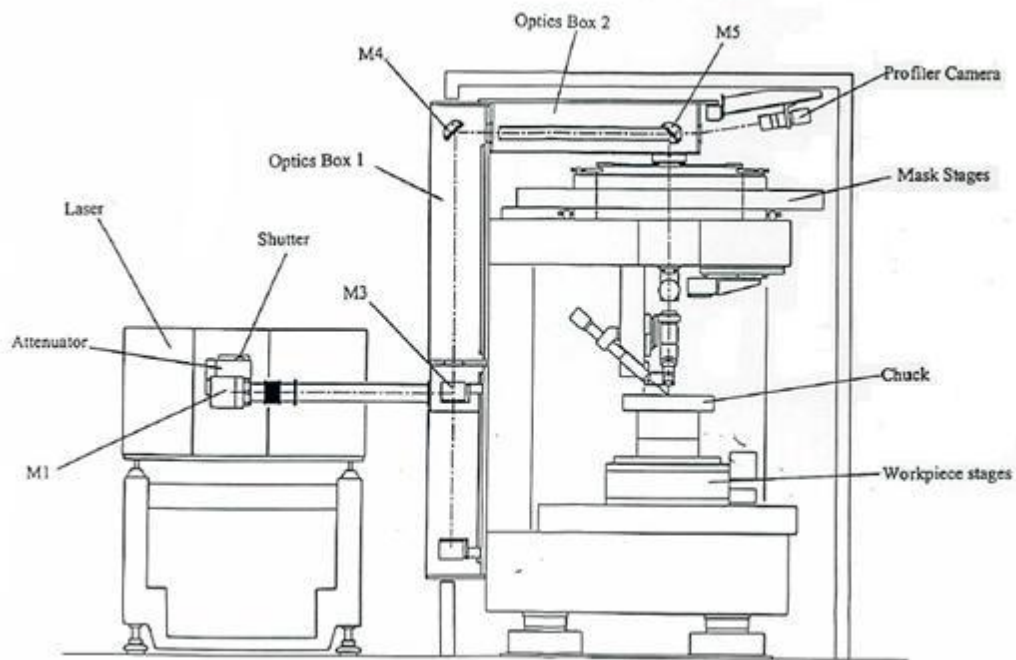


Figure 4.1: Side view of M8000 Excimer workstation

4.2. Excimer workstation components -Description

4.2.1. Laser unit

The excimer gas mixture is Kr, F and He. He is used as a buffer gas. Gas pressure is kept constant at around 3000 mbar. The discharge voltage was adjusted at 21.3kV. The excimer workstation uses a motorized attenuator that uses rotating dielectric -coated plates to produce variable attenuation of the excimer laser beam. The dielectric layer transmission varies depending on the angle at which the laser beam passes through the plate. Laser energy which is reflected from the

plate is safely dumped on a specifically ribbed internal surface which is in direct contact with the attenuator body heat sink.



Figure 4.2: Excimer's laser unit

4.2.2. Optical components

The optical components of the system consist of the following items: a two lens beam relay telescope, a double array beam homogenizer, a fluorescer plate which is used by the beam profiler camera to image the laser beam at the mask, projection lenses for 248nm operation, a diode laser based workpiece height sensor system and workpiece viewing and alignment cameras.

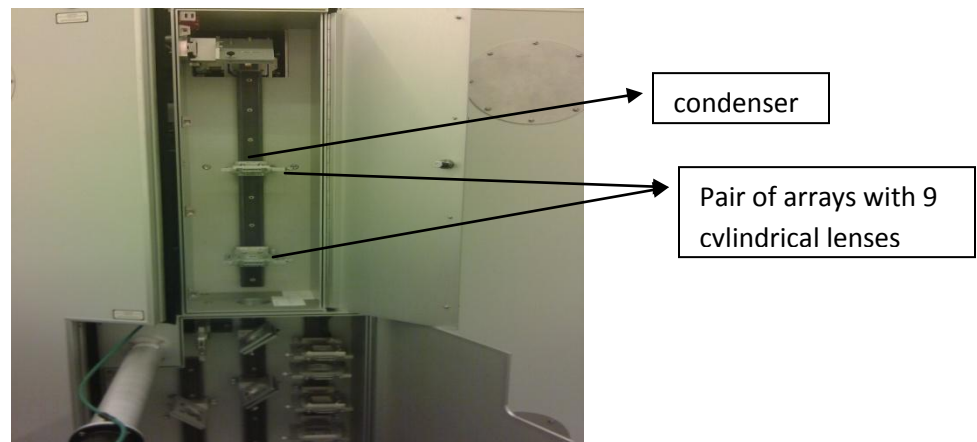


Figure 4.3: Long axis homogenization of the beam

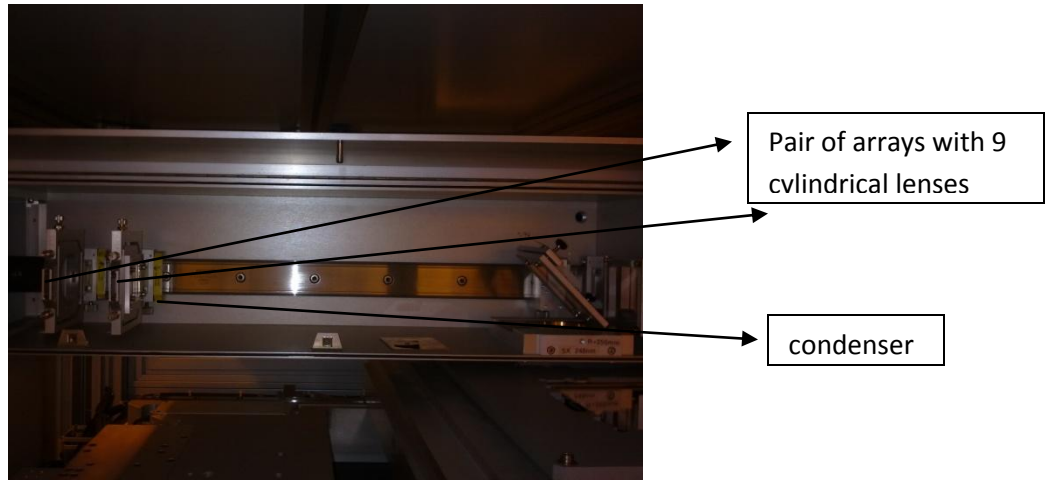


Figure 4.4: Short axis homogenization of the beam

The homogenizer optics shape the initial laser beam (figures 4.5, 4.6) in a homogeneous square beam (figures 4.7, 4.8).

Homogenizer

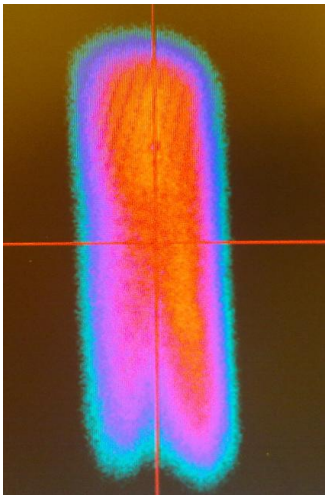


Figure 4.5: 2d laser beam intensity distribution

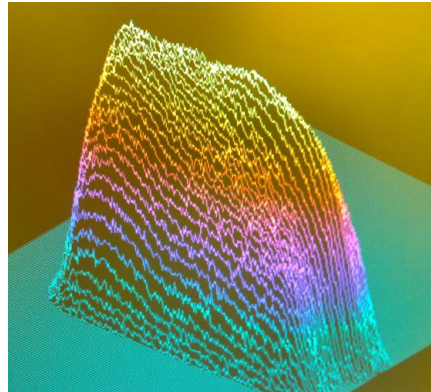


Figure 4.6: 3d laser beam intensity distribution

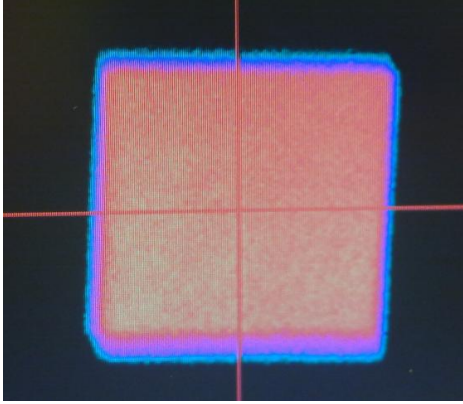


Figure 4.7: 2d homogenized beam intensity distribution

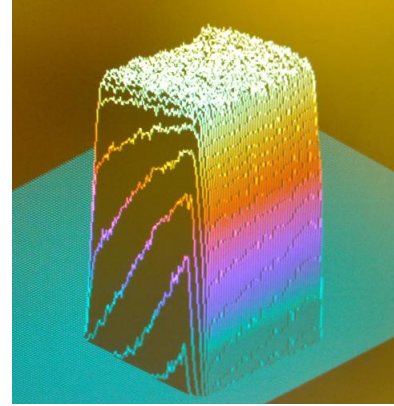


Figure 4.8: 3d homogenized beam intensity distribution

The mask is held on an open frame with a CNC (Computer Numerically Controlled) Z-U stage-set.

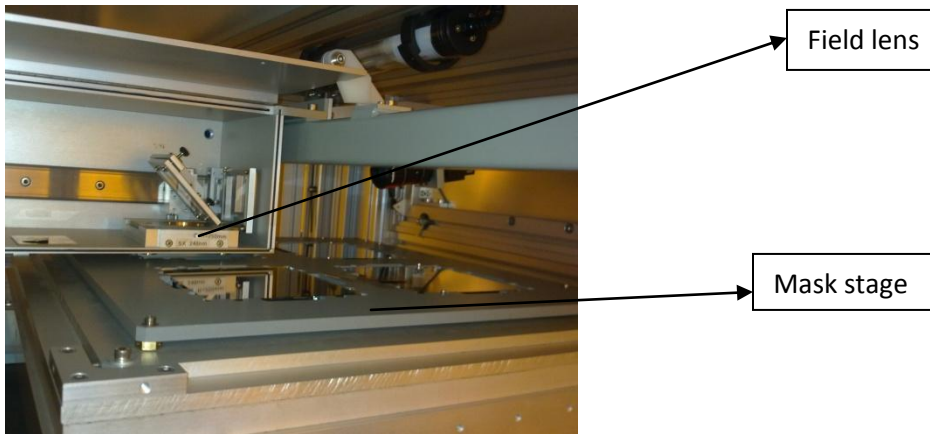


Figure 4.9: Mask stage

The projection lens used for this work had a 1:5 demagnification factor, a numerical aperture (NA) of 0.15 and DOF 50 μ m. Due to the continuous decay of the laser power and to the lack of a self-correction feedback mechanism, it was needed to measure the energy fluence and suitably adjust the attenuator before each experiment. Owing to damage threshold precautions of the energy meter (NOVA II, bfi Optilas), the measurement of fluence took place above the projection lens and not on the stage of the workpiece. The fluence, then, was calculated by the below formula:

Fluence on the workpiece's stage = 0.7 x 5₂ x fluence above the projection lens,

Where the factor 5₂ derives from the 5x demagnification and the factor 0.7 is the percent transmission of the laser light that comes out from the projection lens.

The workpiece stage can move in x-y axis, can rotate from -45° to 45° and can elevate in z axis from 0 up to 25mm.

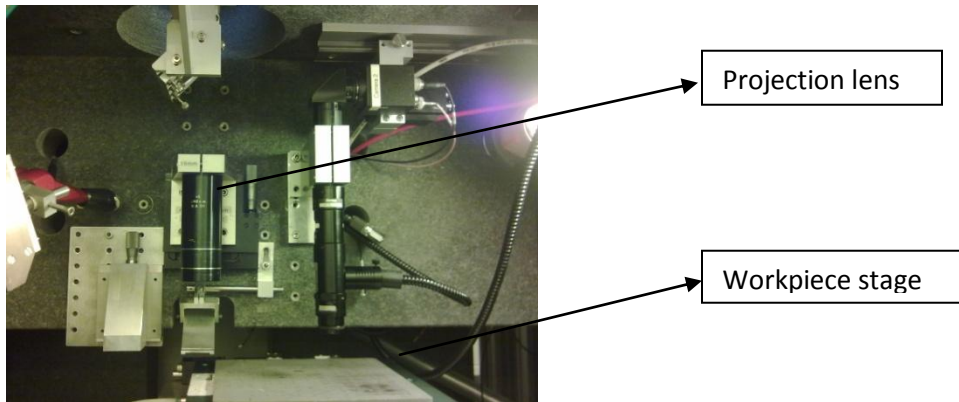


Figure 4.10: Workpiece chamber

4.2.3. Software control of the system

The PC controls the laser via an RS232 communication interface unit, linked by fiber optic cables to the laser. The machine control system Exitech MMI(EMMI) runs under Microsoft Windows NT and the front end MMI is constructed using Visual Basic.

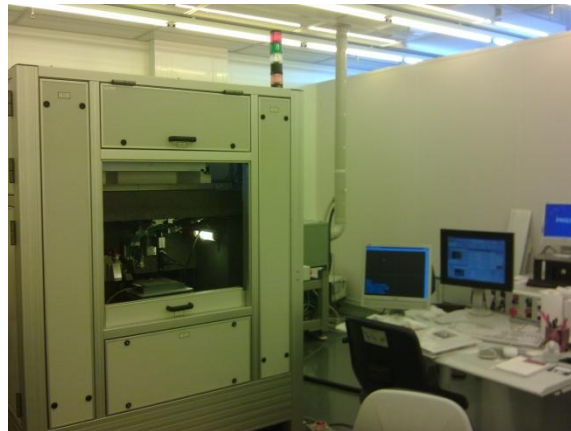


Figure 4.11: Control console system

Chapter 5: Methods

5.1. Surface roughness evaluation by filter implementation

If the variable Z from the rms formula of roughness (2.2) is calculated by subtracting the ideal flat surface from the acquired machined surface, the surface roughness will be overrated. This will happen because the shape deformation is incorporated into the roughness calculation. In order to avoid this, the shape error must be excluded from the calculation.

For this reason, a two dimensional ideal low pass filter is applied to the surface and the outcome of that filter is a smoothed surface that incorporates the shape error. The Z is estimated by subtracting the smoothed surface from the machined surface, so only the factor of roughness remains. The steps of the roughness evaluation method that was used are described below:

Initially a subregion inside the ablated cavity is selected from the wyko dataset, preferably an area with the less or no invalid data.

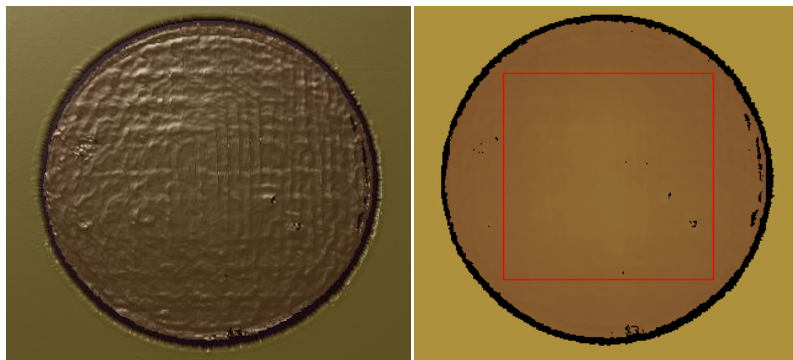


Figure 5.1: Selection of a subregion inside the ablated cavity

The surface of the selected subregion is depicted below. As it can be seen the surface is pretty rough.

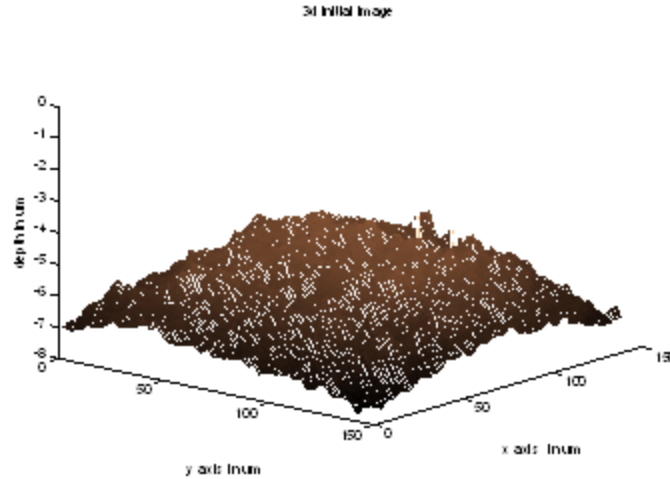


Figure 5.2: Initial surface of the subregion

Then the Fast Fourier transform of the surface is calculated and an ideal rectangle low pass filter is implemented (matlab).

The sample interval is the spatial separation of the sampling points and depends on the magnification. Due to the fact that the sample interval differs in the x and y axis, there can be a different cut off frequency in the x and y axis. The cut off frequency defines the length scale of roughness (above that value the irregularities are considered shape deformation) and should be selected with respect to the sample interval in a way that the length scale of roughness will be the same for all the samples independently from the magnification.

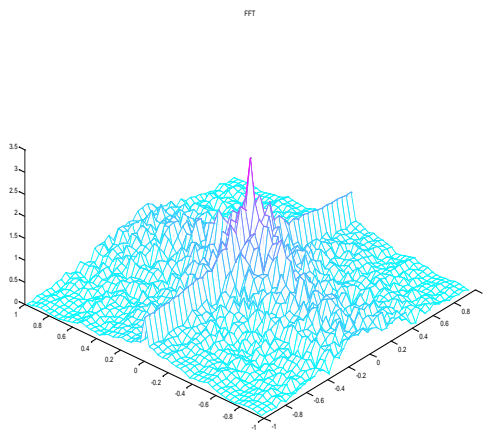


Figure 5.3: FFT of the surface

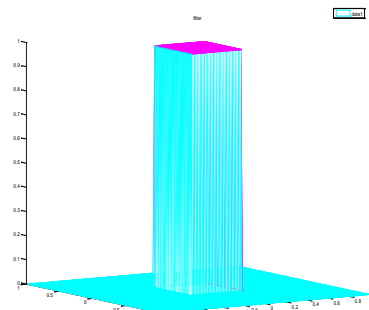


Figure 5.4: Rectangular ideal low pass filter in the frequency domain

The filtered surface will be smooth like the one that is depicted below .

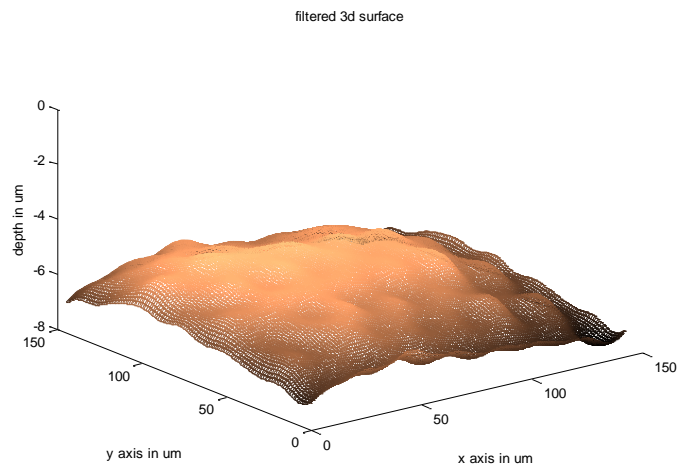


Figure 5.5: Filtered surface

Now, the Z value can be calculated from the subtraction of the two surfaces and the rms value of roughness is estimated. It should also be mentioned that this technique should not be applied to tilted surfaces because the outcome will be invalid.

5.2. Introduction to roughness reduction technique with synchronized scanning

As it was mentioned in previous chapter, even though the laser beam intensity profile should be totally homogeneous as a top hat function, there are temporal and spatial inhomogeneities. Since there is no method to deal with the temporal irregularities, we will deal with the spatial intensity distribution.

Due to the bad quality superimposition between the 9 beamlets from x axis and the 9 beamlets from y axis and the diffraction effects through the homogenizer, the laser beam intensity profile is inhomogeneous. The inhomogeneities of the laser intensity are depicted on the substrate like an imprint. There is created a spatial grid (figure 5.6) of different depths in the plane of workpiece that corresponds to the laser's beam intensity grid. This "grid" contributes to the surface roughness.

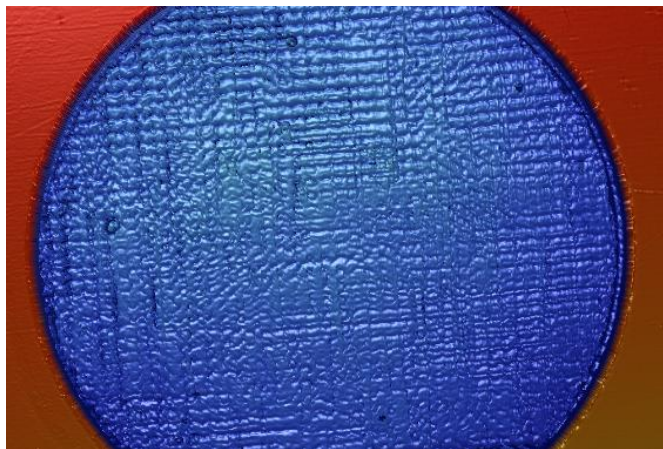


Figure 5.6: 2mm circular hole produced by direct firing

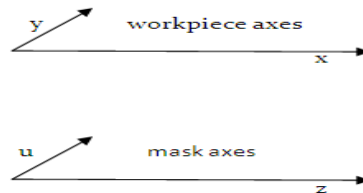
The basic idea of the following technique is reducing the surface roughness by averaging out the uneven laser fluence distribution by irradiating the workpiece from different areas of the laser beam.

Setup configuration

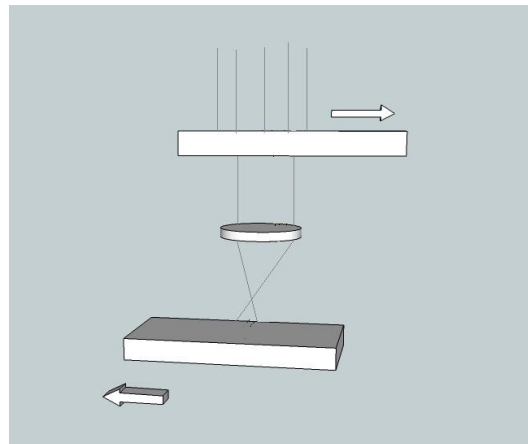
In this technique, a synchronized scanning method is used. The sample is placed on a motorized table that can move in 3d space through a computer controlled rotation (r) and translation (x - y - z) stage controller. The mask is held on an open frame and can move in 2d space through a computer translation (u - v) stage controller. The u and x axes are horizontal, whereas the y and v axes are vertical. Below a simplified model of the setup is available:

The process relies on the repetition of certain number of loops, which are determined by the user.

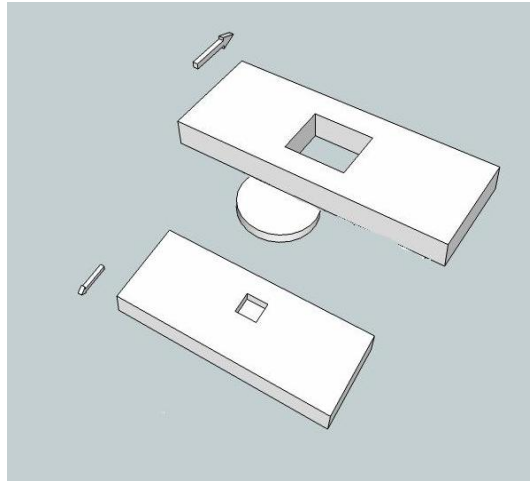
One loop consists of the following movements:



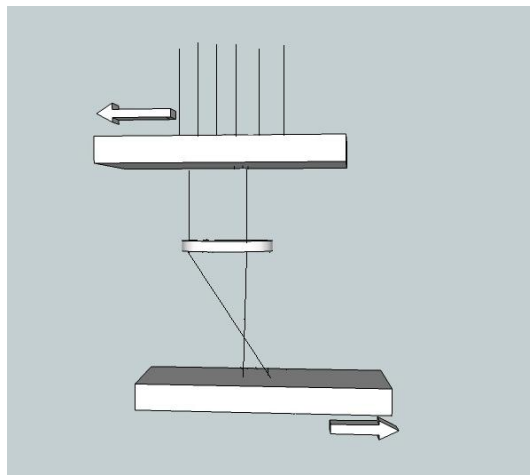
a) In the first step, there is a horizontal shift (Δx) of the workpiece stage at x axis and simultaneously an opposite to the direction of x-shift, a shift of the mask stage at u axis (Δu). The speed of the mask stage (speed_m) is 5 times the speed of the workpiece stage (speed_w). It should be mentioned that the speed is always constant. Due to the demagnification factor, the relationship between Δu and Δx should be: $\Delta u = 5x \Delta x$. During this mask-workpiece synchronized movement, the laser pulse firing is triggered.



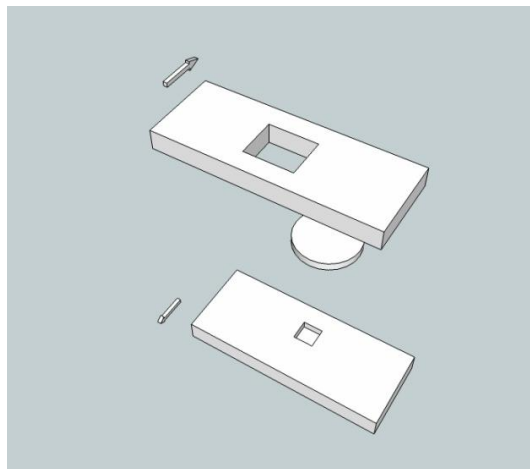
b) In the second step, there is an equivalent movement laterally. That means that instead of x-u, there is y-v axis shift (Δy and Δv).



c) The third step is an identical repetition of the first step but this time backwards.



d) Finally, the last step is also an identical repetition of the second step.



The user inserts the attenuator parameters (to define fluence), the total number of pulses that there will be irradiated on the workpiece, the repetition rate, the number of loops and the Δx and Δy stage translation. Then the firing pitch (distance that the mask stage travels between successive laser pulses)) and the scan speed of the mask stage are calculated by the following equations:

$$\boxed{distance = 2\Delta z * noloops / nopulses}$$

$$\boxed{speed_m = distance * rebrate}$$

noloops: number of loops

nopulses: number of pulses

rebrate: repetition rate

speed_m = speed of the mask stage

Δz : translation of the z axis

distance: distance that the mask stage has traveled between successive pulses (firing pitch)

Because of the potential that the following set of commands provide :

```
PSOP,0,10
PSOD,0,distance
PSOF,3,x,z
G91 G1 x( $\Delta x$ ) z( $\Delta z$ ) f(speedm)
```

the computer sets the laser pulse train at fixed incremental distance which is activated and locked by the movement of x and z axis. By this way, the synchronized movement of the first and third step is accomplished. The synchronized fireless movement of the second and forth step is realized by a simple opposite translation between the axis like:

```
G91 G1 y( $\Delta y$ ) u( $\Delta u$ ) f(speedm)
```

This process is repeated noloops times by the value that the user has entered.

Distribution of the laser fluence at the workpiece

A very simplified way to describe the distribution of the laser fluence at the workpiece is by ignoring the wave nature of the light and accepting the following simplified model:

We consider the unknown intensity distribution of the laser as a $I(x,y)$ function in space that is time independent. Because we consider that there are no temporal inhomogenities, we will consider a continuous fluence intensity distribution $F(x, y)$ which is the same for every pulse. The

binary mask aperture can be described as a $G(x,y)$ spatial function, where it is 1 for the open area and 0 for the rest.

Because a pulsed laser is used, time is described as a discrete variable : $t=t(n)$ where n is the number of pulses that have been irradiated ($n=0$, the laser ablation hasn't started yet).

The fluence that the workpiece receives in a simultaneous translation of the z axis of the mask stage and of the x axis of the workpiece stage is:

$$F_{workpiece}(x/5, -y/5) = 25 * \sum_{n=0}^{nopulses} F(x + ut(n), y) * G(x, y)$$

$$-L_x < x < L_x$$

$$-L_y < y < L_y$$

Where $L_x, -L_x$ are the borders of the mask aperture in x axis and $L_y, -L_y$ in y axis.

Restriction

Because the number of pulses should be integer in each step, the number of pulses should be multiple of the firing steps and more specifically should be multiple of $2 * noloops$. Of course, this can be solved with a trade-off in the energy.

Chapter 6: Results and discussion

6.1. Introduction-Chapter's goal

This chapter is divided into two parts. The first part is related to shape deformation experiments and is subdivided into three parts who deal with different shape deformations. The second part is devoted to roughness reduction experiments with the technique that was described previously.

6.2. Measurements setup

The measurements of the samples' topography were achieved by the Wyko NT1100 interference profilometer system.

The vertical measurement range of wyko NT1100 system is 0.1 nm to 1mm. The vertical scan speed is up to 7.2 $\mu\text{m}/\text{sec}$ and the lateral spatial sampling is from 0.08 up to 13.1 μm .

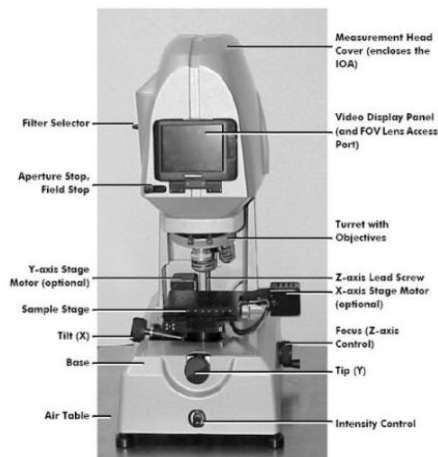


Figure 6.1: Wyko NT1100

Part A: Shape deformation

A.1. Ablation rate- size of the ablated area

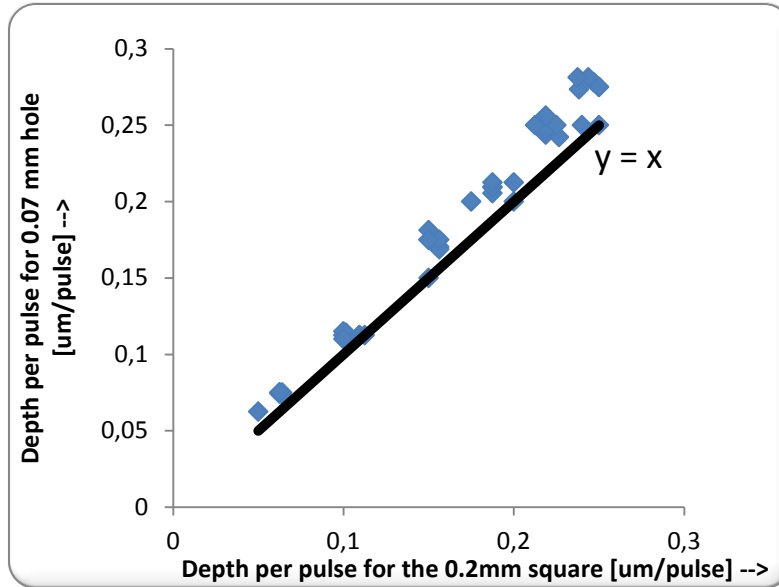
In this part the relationship between the ablation rate and the size of the ablated area of the workpiece is examined. Here it isn't examined a "pure" shape deformation, but a connection between two variables that may lead to shape deformation if it won't be taken into account.

A series of experiments with holes of different size was performed. The intention was to check the assumption that the ablation rate increases with the decrease of the ablated area. According to [36], a dependence of polycarbonate's depth rate on laser spot size has been observed when the laser's spot diameter is less than about 200 μm . So, the ablation rate seems to increase with the decrease of the laser spot's diameter and the influence of the ablation plume on the ablation is claimed to be the main cause of this behavior.

A.1.1. Experiment with quadratic and circular mask aperture

Initially, a simple experiment with two different mask patterns was performed. A quadratic and a circular aperture that was comparatively smaller, were selected from the contour mask, and were irradiated with five different fluences in the range of 100-700 mJ/cm^2 . For each fluence, holes of 2,4,8,16,32,64 and 128 pulses were ablated. The diameter of the hole was 70 μm and the side of the square was 200 μm .

To present all the data into one graph, the x and the y axes were selected as it is displayed below. If the aperture's size does not affect the ablation rate, an almost $y=x$ line should be formed due to the fact that the depth rate in x axis (square) should be equal to the depth rate in y axis (hole). On the contrary almost all the points are located in the $y>x$ region. This fact implies that the y values (depth rate for the hole) are greater than x values (depth rate for the square). This means that the ablation rate is lower in the "big" square hole than in the small "circular" hole for identical laser parameters. Consequently, the assumption is confirmed.



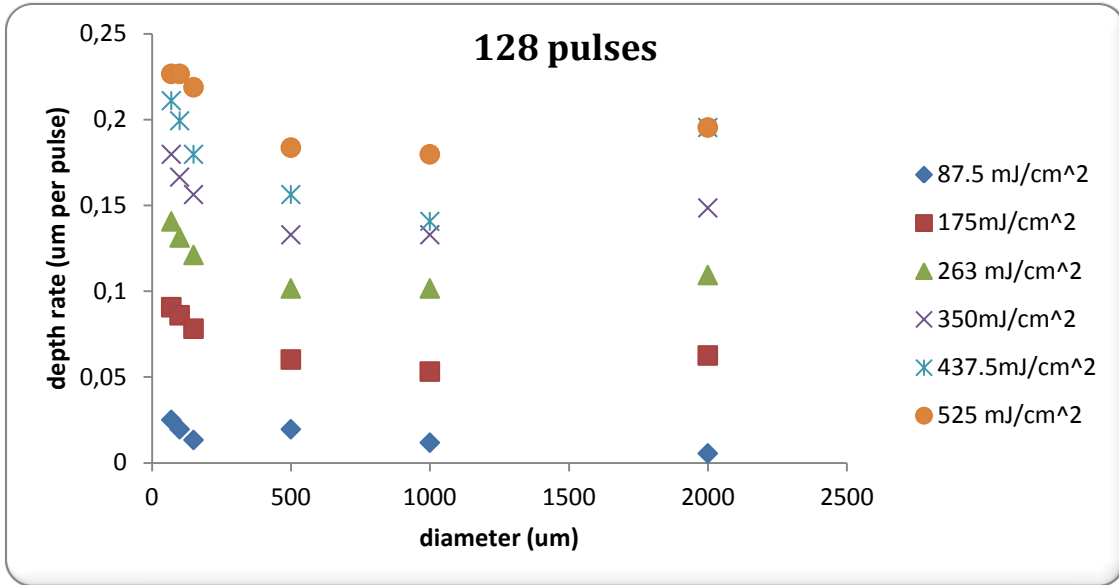
Graph 6.1: Ablation rate of a “big” square aperture and a “small” circular aperture

A.1.2. Experiment with circular mask patterns of different diameter

Another experiment, but this time, with six circular apertures of different diameter from the contour mask, was performed. The diameters of the holes were 75 μm , 100 μm , 150 μm , 500 μm , 1mm and 2mm. Each mask aperture was irradiated with 2, 4, 8, 16, 32, 64, 128 and 256 pulses and the repetition rate was 50Hz. The fluence varied between 87.5 mJ/cm², 175mJ/cm², 263 mJ/cm², 350 mJ/cm², 437.5 mJ/cm² and 525 mJ/cm².

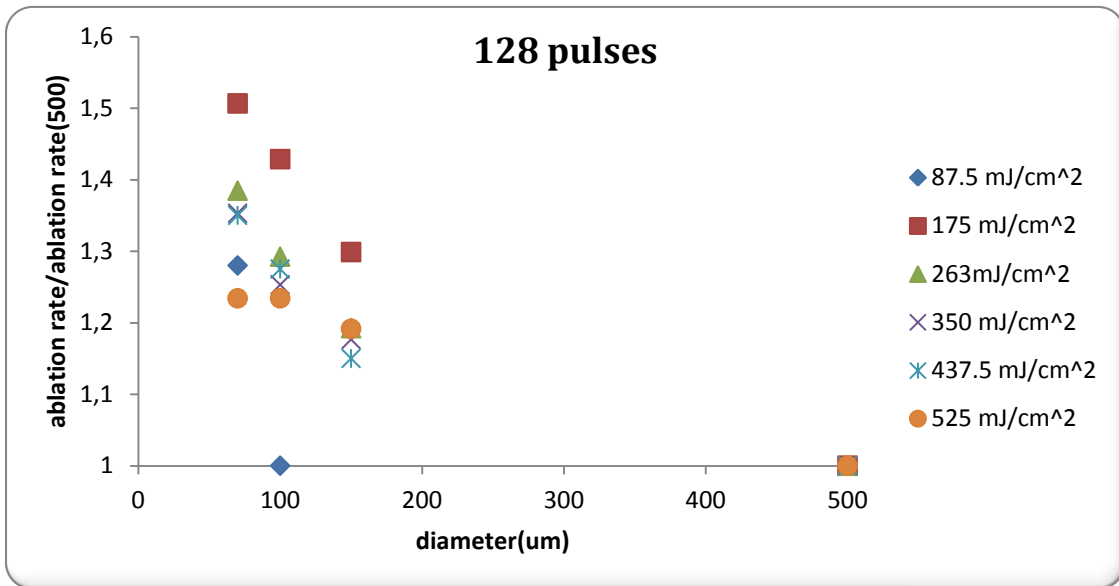
The following graph represents the different depth rates for each fluence for 128 pulses. This number of pulses was selected on purpose, since for 256 pulses there are a lot of invalid data in the measurements and for 2,4,8 and 16 pulses the measurable depth in low fluences is close to the accuracy limits of the wyko instrument. For 32 and 64 pulses a graph that exhibits similar behavior was created but it is not presented here.

From the graph below, it is observable that the depth rate decreases as the hole’s diameter increases until the diameter of 500 μm , while such a relation does not exist for the two bigger holes (diameters of 1 and 2mm). That is in accordance with the previous study [36] where the critical value was determined around 200 nm.



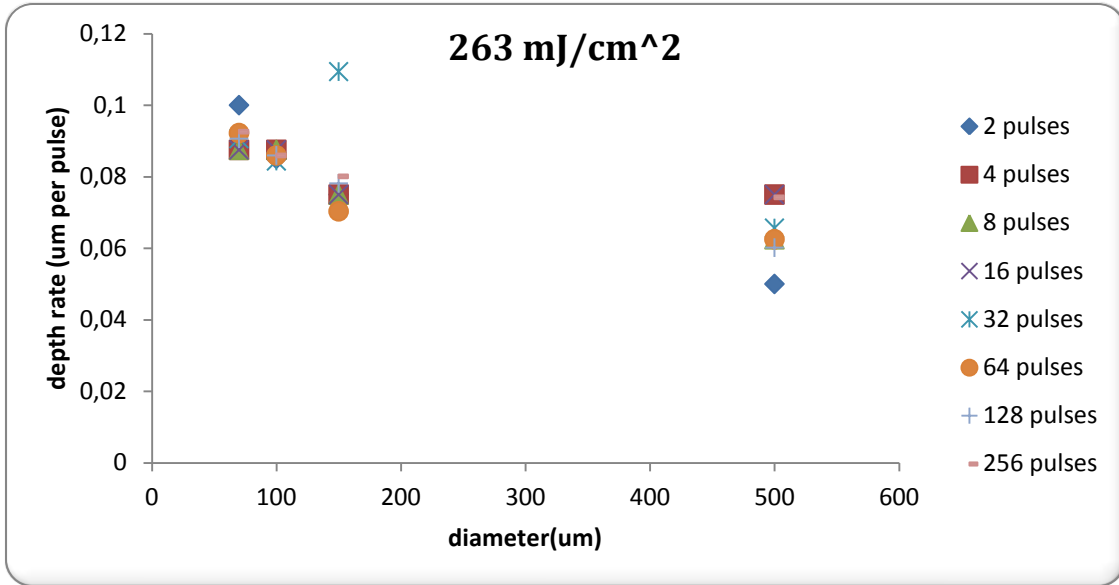
Graph 6.2: Ablation rate of holes with different diameters

For a better visualization of the previous result, a graph of ablation rate divided by the ablation rate of the 500µm hole versus diameter was created.



Graph 6.3: Ablation rate of holes with different diameters scaled to the ablation rate of 500µm hole diameter

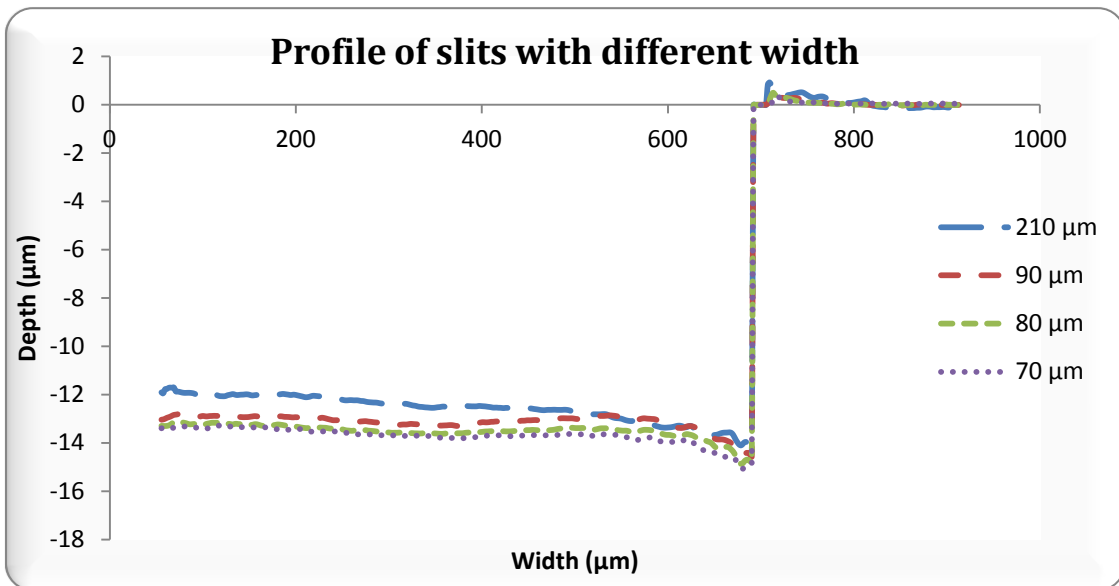
In order to check the assumption that for less number of pulses the depth rate will be almost the same for all the different hole sizes, the below graph was created. It depicts the depth rate for different number of pulses of fixed fluence 263mJ/cm² versus the diameter. As it can be seen, there is no verification of the previous assumption.



Graph 6.4: Ablation rate for low number of pulses

A.1.3. Experiment with rectangular slits

As a sequel of the previous experiment, this experiment was performed with slits of different width instead of circular holes of different diameter. As it can be seen from the surface profile of each slit, there is a certain decrease of the cavity's depth as the slit gets wider.



Graph 6.5: Cavity profile of the different width slits that were irradiated by the same parameters

A.1.4. Discussion

According to the previous experiments, there was observed a certain behavior that dictates an increase of the ablation rate with the decrease of the mask area. We should also mention that this observable ablation rate- ablated size dependence exists for different mask patterns and it is not limited to a certain shape like circular or quadratic. Also, as it was mentioned above, this behavior was valid for diameters below 500 μm , something quite sensible since the drilling depth is of the order of some decades of microns. This means that above 500 μm , the aspect ratio is so low that the ablated area may not be considered as a cavity but as an open area.

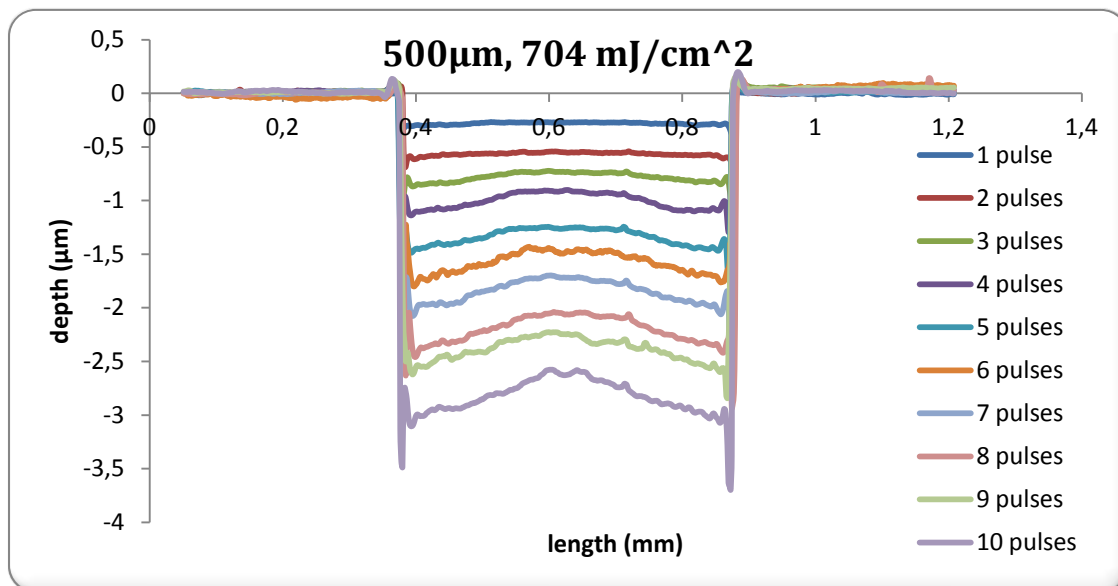
The explanation of this observation isn't very clear, but there is a high probability that relies in the plume expansion behaviour. There is evidence that as the aspect ratio increases, the degree of ionization increases [37] and the size of the ejected clusters of the ablated material decreases [19]. The bigger the clusters, the more attenuation the ejected plume provides and the ablation rate decreases [38]. Another explanation has to do also with the plume again, but this time with the plume kinetics. Different pattern size provokes different shape of plume expansion and this means different degree of attenuation.

A.2. Formation of surface bump

A serious surface deformation and more specifically the creation of a surface bump in the centre of circular ablated holes was observed. A series of experiments was performed in order to have a better insight in this type of deformation.

A.2.1. Evolution of the bump shape

In order to have an insight in the starting point of the bump's formation, an experiment with low number of pulses was performed. The circular aperture of $500\mu\text{m}$ was irradiated with $704\text{mJ}/\text{cm}^2$ from 1 up to 10 pulses. There is an obvious accumulated shape deformation while the number of pulses and consequently the depth is increased.

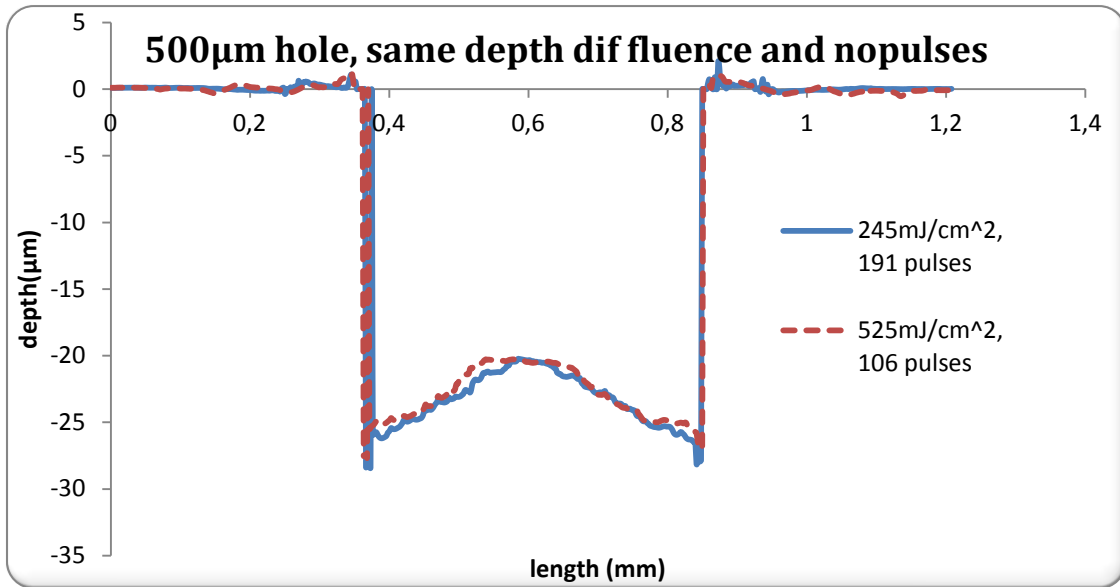


Graph 6.6: Evolution of the x axis cavity profile for low number of pulses

A.2.2. Fluence – number of pulses tradeoff

In this part, the tradeoff between number of pulses and fluence was examined with respect to bump formation. A fixed depth was chosen and in the first case a combination of $245\text{mJ}/\text{cm}^2$ and 191 pulses was tested, whereas in the second case $525\text{mJ}/\text{cm}^2$ and 106 pulses. The shape of the bump seems to be almost the same. So in the question if this deformation depends more on the energy fluence or on the number of pulses, this graph indicates that the deformation is equivalent

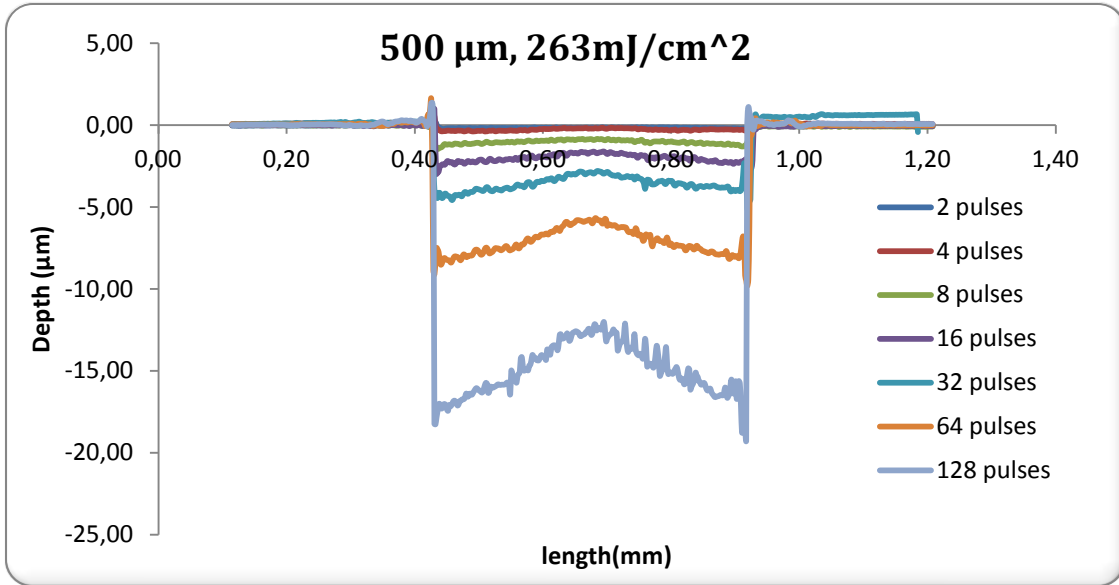
for these different parameters. Of course, more experiments are needed for the deduction of a solid conclusion.



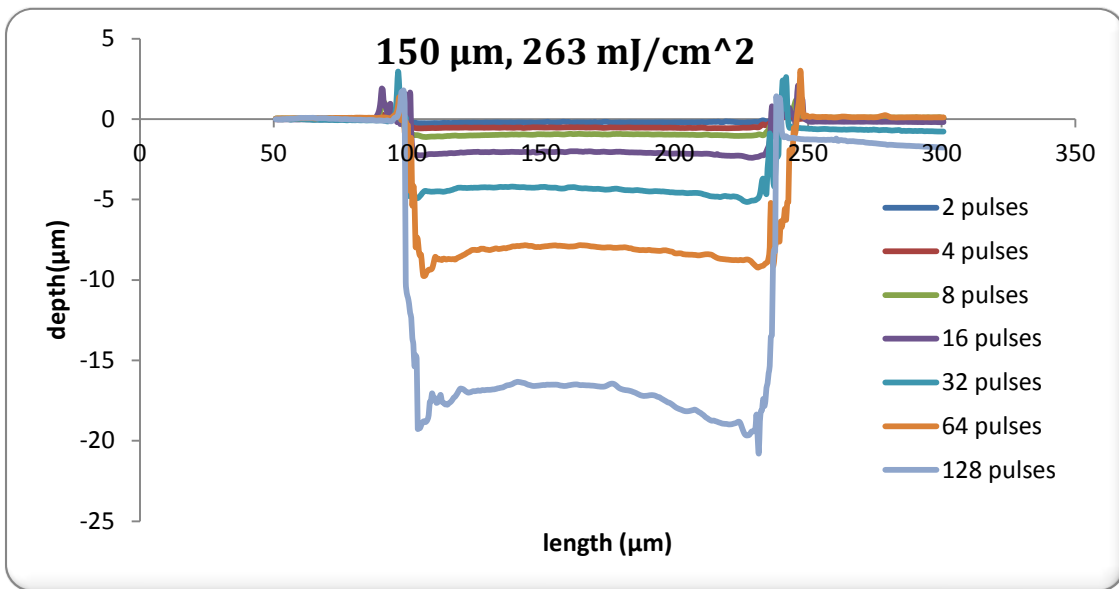
Graph 6.7: Profile for laser fluence- n pulses trade off

A.2.3. Formation of the bump for circular holes with different diameter

The following two different holes were irradiated under exactly the same conditions (263mJ/cm², 50Hz). The difference between the two different circular holes relies on the diameter. As it can be observed from the two profiles, the formation of the bump is more dramatic for the 500 μm aperture and less for the 150 μm.



Graph 6.8: Evolution of the surface profile for a 500µm diameter hole



Graph 6.9: Evolution of the surface profile for a 150µm diameter hole

Following the previous experiments, the ablation depth and the height of the bump were measured for circular holes with different diameter under identical experimental conditions (300mJ/cm², 100 pulses, 50 Hz). The measurements are summarized below:

Hole's diameter	Cavity's depth	Bump's height	Height/Depth
2 mm	12.4 μm	2.0 μm	0.14
1 mm	11.8 μm	3.4 μm	0.29
500 μm	11.5 μm	3.2 μm	0.28
400 μm	11.5 μm	3.7 μm	0.32
140 μm	14.1 μm	2.0 μm	0.14
100 μm	14.6 μm	1.5 μm	0.1
70 μm	16.4 μm	1.2 μm	0.07

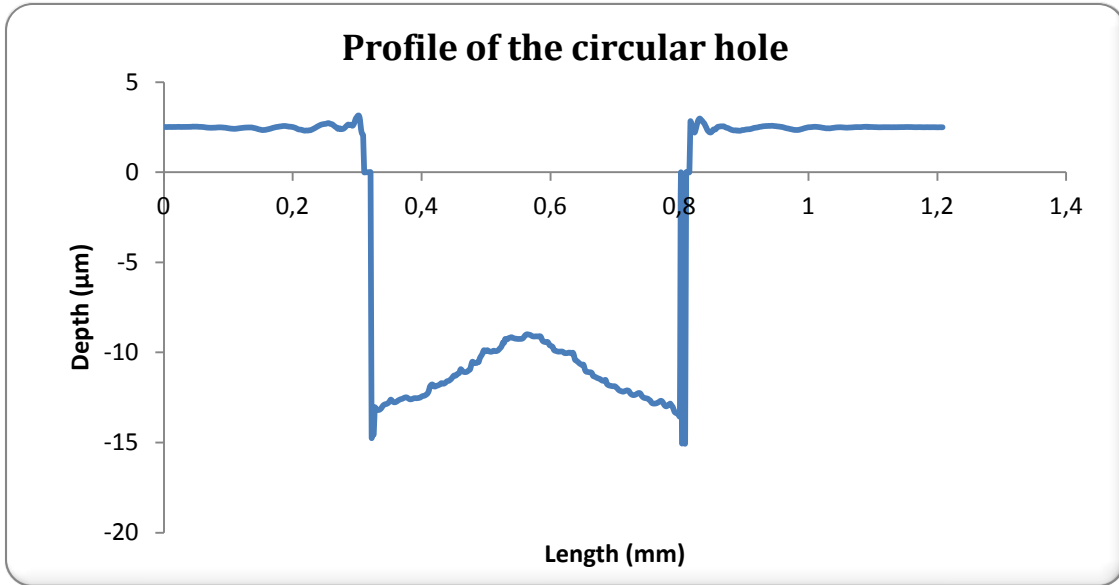
Table 1: Bump's height for different holes' diameters

From the profiles of the two circular apertures, it can be seen a different bump's evolution. The bump is less dramatic for the smaller hole. But from the above table it cannot be concluded that the bump is reduced along with the decrease of the hole's diameter proportionally. There is no linear relation between the hole's diameter and the depth to height ratio, but there is an obvious reduction of the bump's height for smaller hole's diameters.

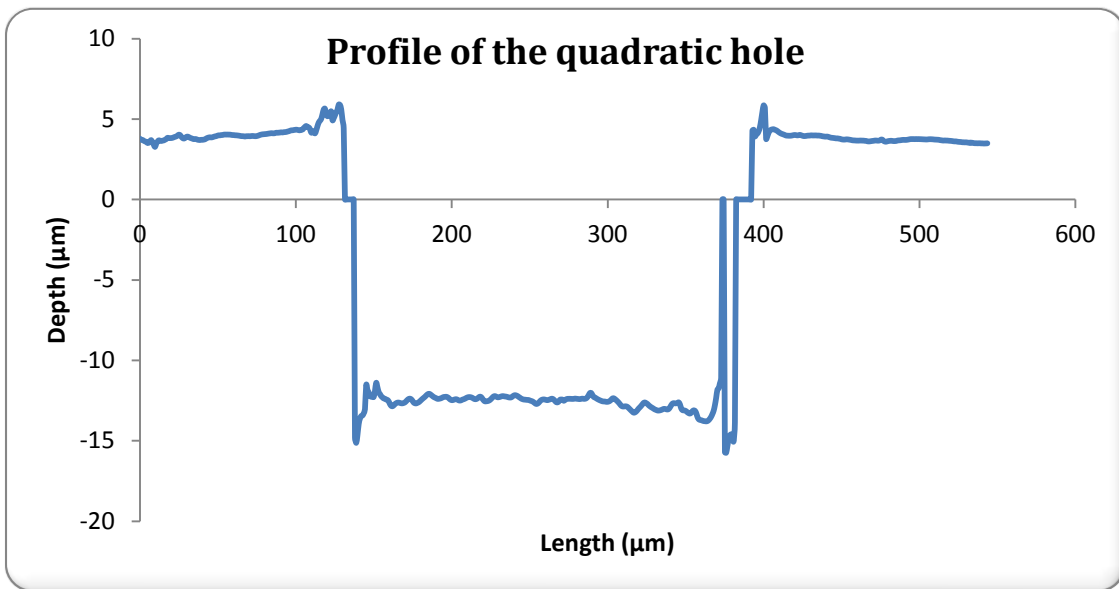
A.2.4. Comparison between the depth profile of circular and square aperture

A hole of 500 μm diameter and a square of 250 μm side were irradiated with 100 pulses, 300 mJ/cm² and 50 Hz. Below, there are presented the surface profile and the topography of the ablated cavity. The depth was measured (in the centre of the cavity) at 11.7 μm for the circular and 16.6 μm for the quadratic cavity.

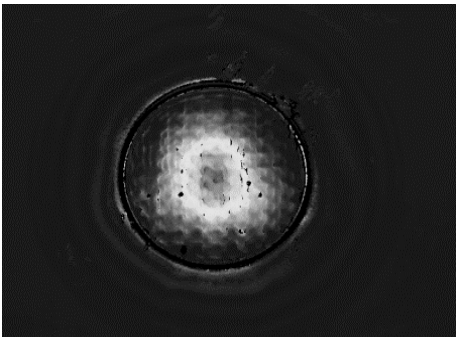
The difference between the two depths is significant. Apart from the bump in the circular cavity, there is a discernible deformation in the topography of the quadratic square, which it is more visible in the graphs with the top view of the ablated holes (Graph 6.13).



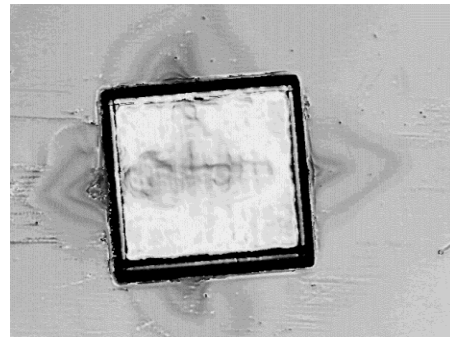
Graph 6.10: Surface profile of the circular cavity of 500 µm diameter, 100 pulses, 300 mJ/cm²



Graph 6.11: Surface profile of the quadratic cavity of 250 µm side, 100 pulses, 300 mJ/cm²



Graph 6.12: Topography of the circular topography



Graph 6.13: Topography of the quadratic cavity

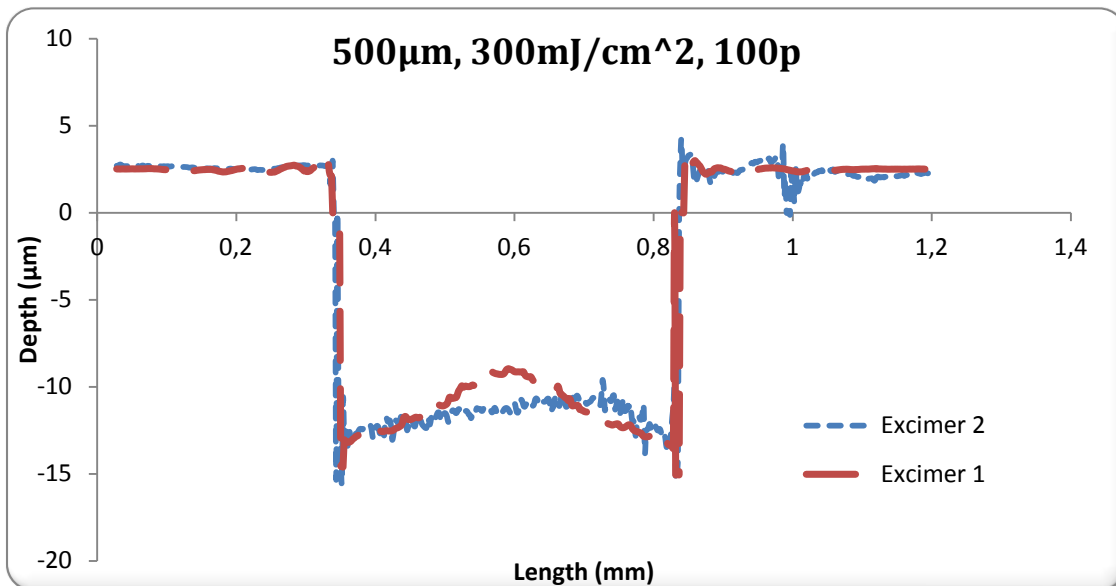
From the above graphs with the top view, we observe indications that this type of deformation derives from diffraction effects.

A.2.5. Comparison with another excimer setup

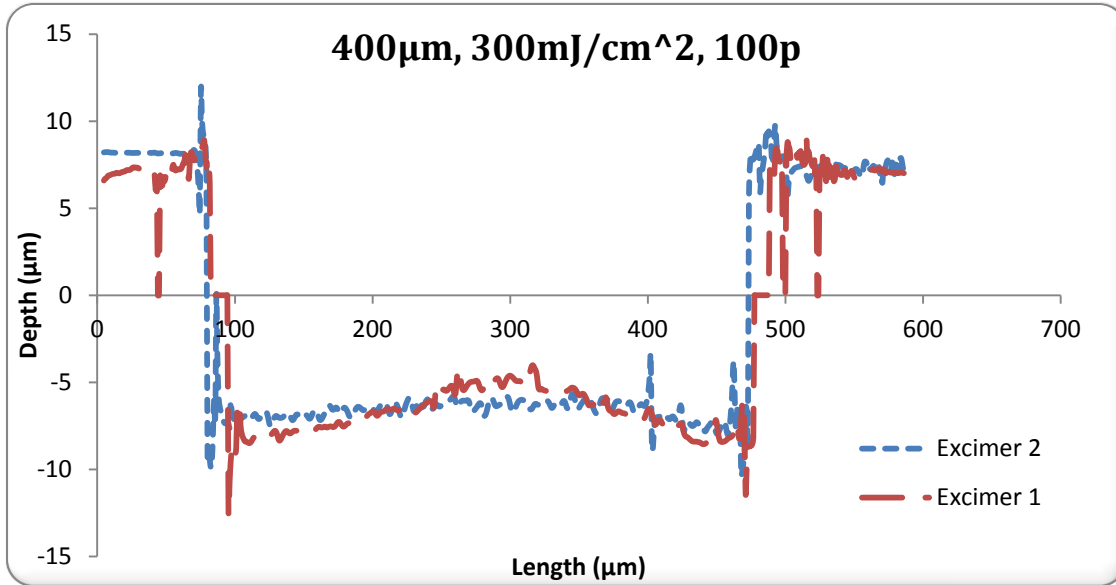
An experiment with the same mask and the same mask apertures was performed in another excimer setup (excimer 2) and the results were compared with the ones from this study's excimer (excimer 1).

The formation of the bump was examined for the same fluence (300 mJ/cm^2), the same number of pulses (100) and the same circular apertures ($400 \mu\text{m}$, $500 \mu\text{m}$) for which the bump was more dramatic. The second excimer setup has a different beam shape (rectangular instead of quadratic), more beamlets in the homogenizer (12×13 instead of 9×9) and a different NA of the projection lens (0.13 instead of 0.1).

As it can be seen from the below graphs, even if there is no flat surface in the cavity by using the second setup, there is no such a bump. The surface has still irregularities, but they differ.



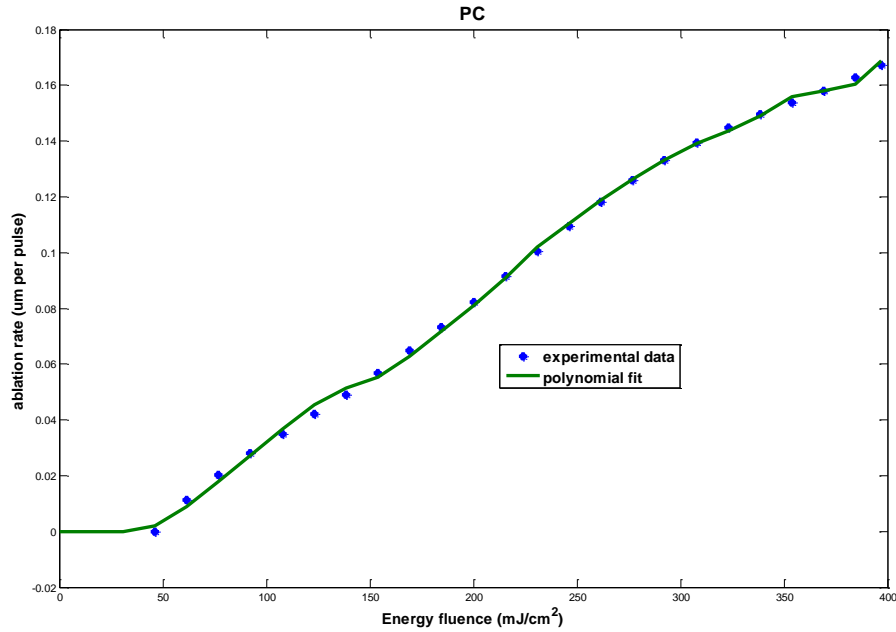
Graph 6.14: Comparison of the used setup (red line) with another excimer setup (blue line) for a $500 \mu\text{m}$ diameter hole



Graph 6.15: Comparison of the used setup (red line) with another excimer setup (blue line) for a 400 μ m diameter hole

A.2.6. Ablation curve of polycarbonate

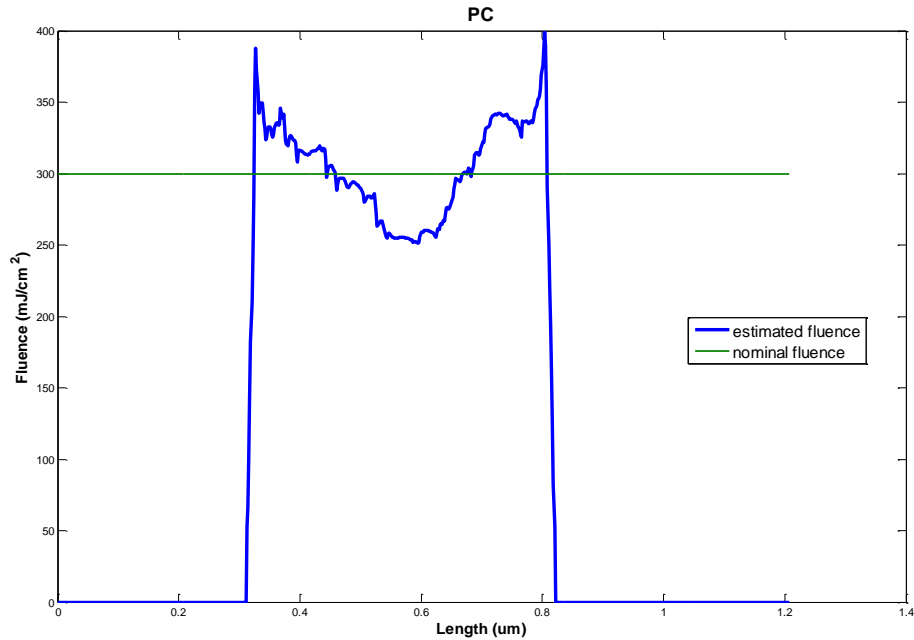
With the use of a grayscale test mask (see appendix), the ablation curve (ablation rate vs fluence) for polycarbonate was obtained from 0 till 400 mJ/cm². Then, with the use of matlab, polynomial fit of 5th order was implemented to the experimental data points and the below curve was produced. The fluence threshold was estimated around 50 mJ/cm².



Graph 1.16: Ablation curve of polycarbonate

Then, if we make the assumption that the ablated depth corresponds in an ideal way to the irradiation that was absorbed by the surface and no other phenomena take place, we can estimate the irradiation profile that will correspond to the depth profile from the 5th order polynomial equation.

An ablated 500 um diameter hole by 100 pulses and with 300 mJ/cm² nominal fluence was created. The hypothetical fluence profile of the ablated cavity is depicted below. As it can be seen, it seems that in the center of the cavity the fluence is less than the nominal, whereas as we head towards the edges the fluence is more than the nominal.



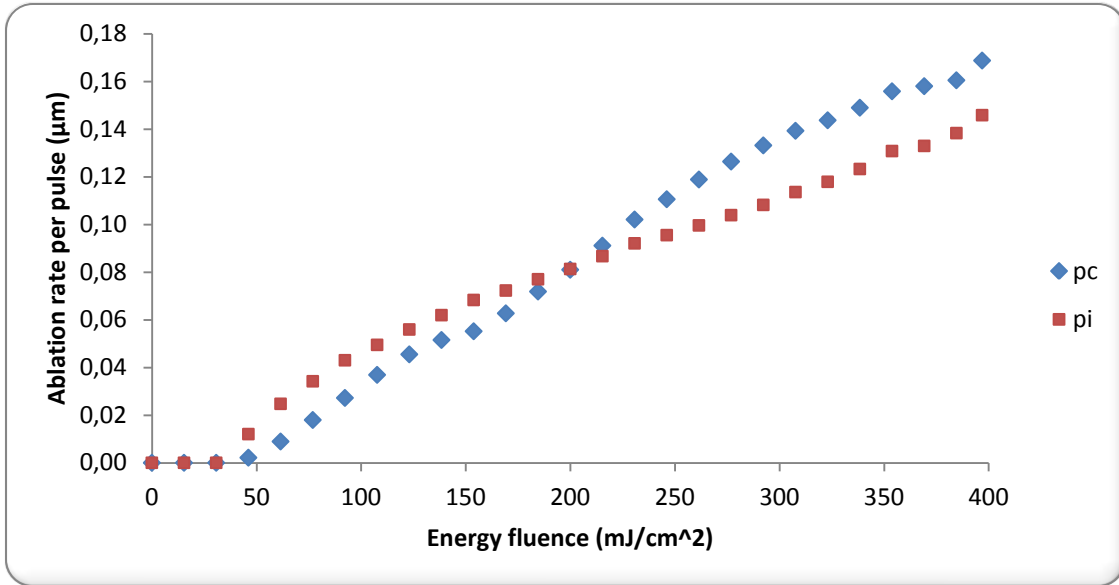
Graph 1.17: Fluence distribution of polycarbonate

A.2.7. Discussion

From the previous experiments, there are strong indications that optical effects like diffraction etc affect and are responsible for that kind of deformation. Before we investigate further the optical elements of our system, some more experiments were performed that make doubtful a total optical explanation of the problem.

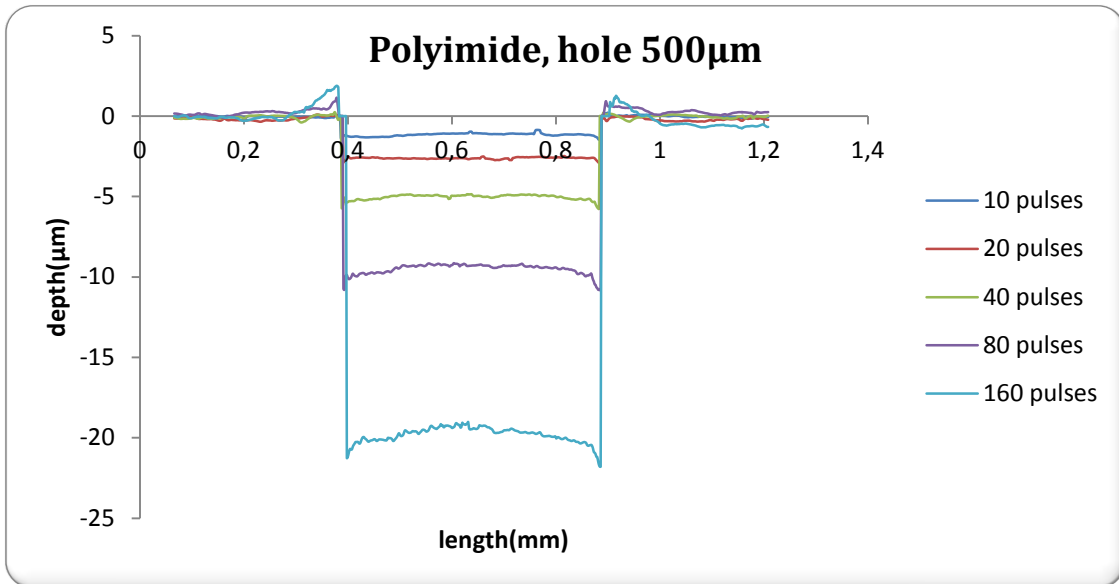
A.2.8. Comparison with a different polymer

In order to check the assumption that the main cause of the bump deformation is due to a system's internal optical error, another polymer with similar ablation behavior (the effective absorption coefficients are very close [11]) was tested. The graph below shows both the ablation curve of polycarbonate and polyimide. The ablation curve for polyimide was obtained by the same way as for polycarbonate.



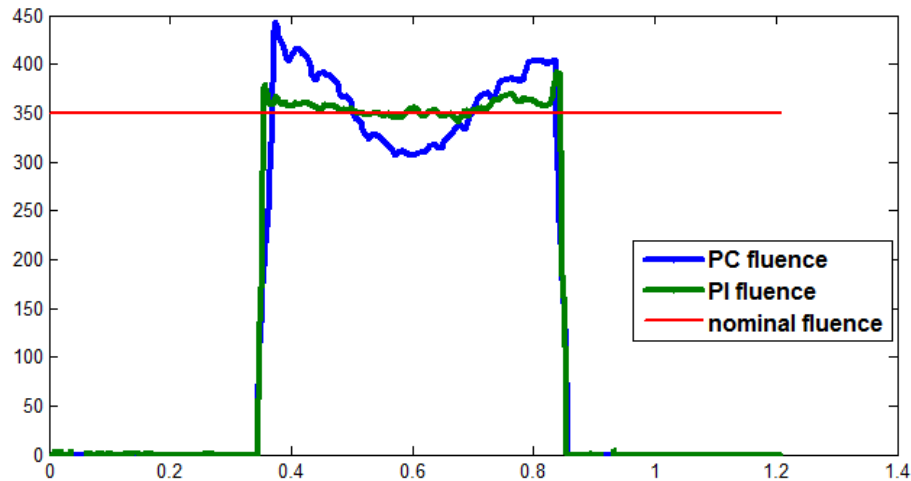
Graph 6.18: ablation curve of pc vs ablation curve of pi

The circular aperture for which the bump formation was more apparent was that of 500µm. For that reason, this particular hole was used for this experiment. A sample of polyimide instead of polycarbonate was selected to be irradiated. As it can be seen, the formation of the bump is not so obvious and in some cases the existence of the bump is doubtful.



Graph 6.19: Evolution of the cavity profile of polyimide

An ablated 500 μm diameter hole by 100 pulses and with $350 \text{ mJ}/\text{cm}^2$ nominal fluence was created on polyimide and polycarbonate. The hypothetical fluence profiles of the ablated cavities are depicted below.

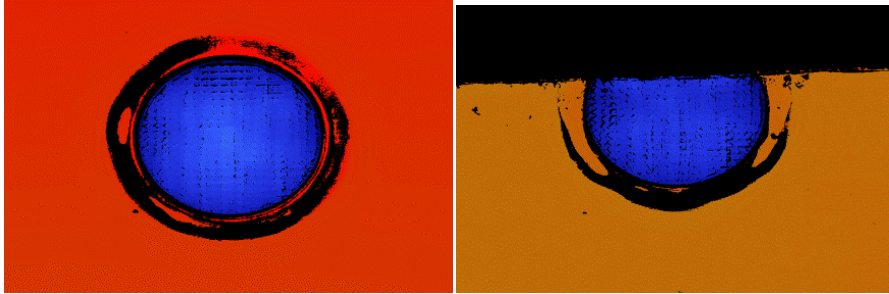


Graph 6.20: PC vs PI fluence distribution

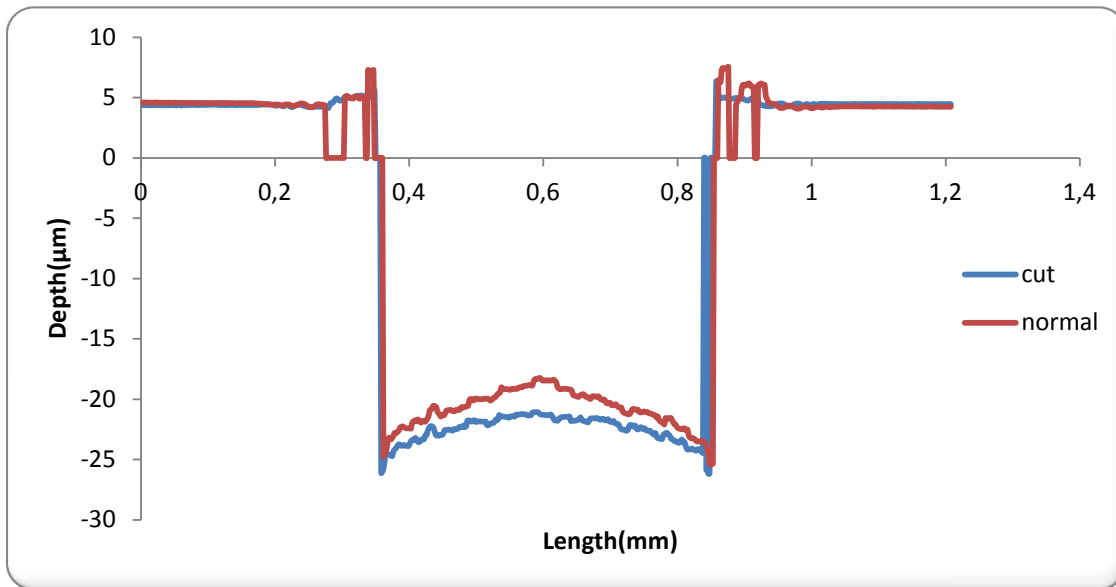
As it can be seen from the above graph, the energy distribution of polycarbonate and polyimide differs from the nominal energy distribution, but in polyimide's profile the difference isn't such dramatic. Moreover, the energy distributions between the two polymers differ a lot, although theoretically should be identical.

A.2.9. Cross section of the bump

In order to get a cross section of the cavities and avoid the noise that is introduced by the cutting, in the next experiment a circular aperture of 1 mm was ablated on the edge of the sample, so that one portion of the laser energy would be directed outside of the material's region. An aperture with exactly the same parameters was also ablated inside the sample's region. The top view of these ablated regions can be seen below:



The center's profile of the two cavities (integral and cut) is displaced below.



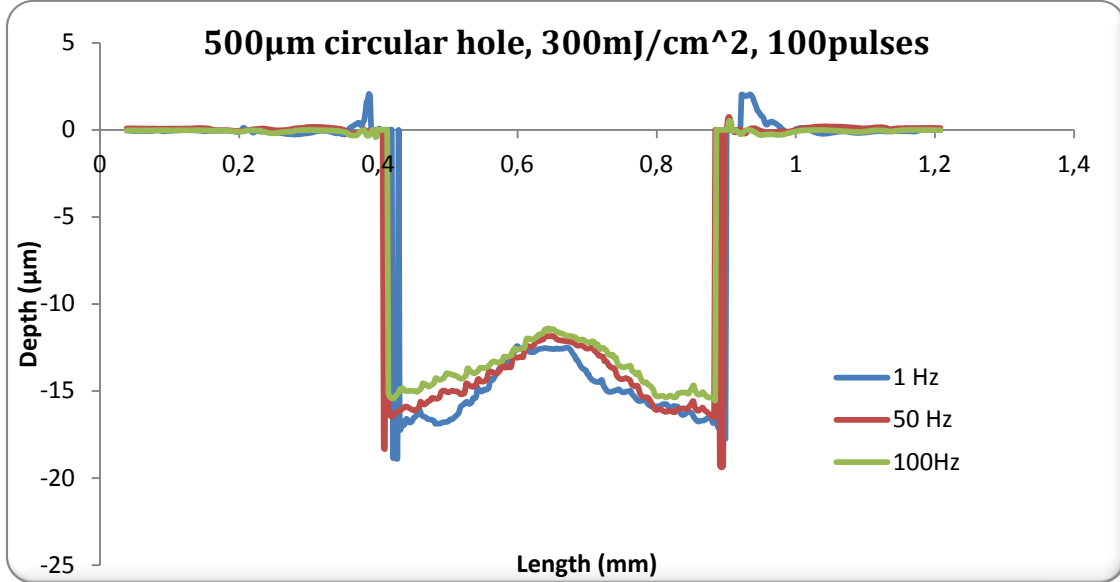
Graph 6.21: Comparison of an ablated cavity on and away from the edge

It is observable that the bump formation is less pronounced when a part of the ablated cavity is outside the borders of the sample.

A same experiment was performed with a rectangular aperture, but there wasn't observed any noticeable difference in the two profiles like in the graph 18.

A.2.10. Repetition rate

In order to examine the possibility of a thermal effect that is responsible for this deformation, some experiments with different repetition rate were performed. The bump formation was obvious in every experiment and no significant change in the topography was observed.



Graph 6.22: Cavity profile for different repetition rates

A.2.11. Debris deposition

In order to check the assumption that there is debris deposition inside the ablated cavity and not only at the surrounding surface the samples were cleaned by liquid wash and by ultrasonic cleaner. The topography around the cavity slightly became smoother but no significant change reported inside the cavity.

A.2.12. Discussion

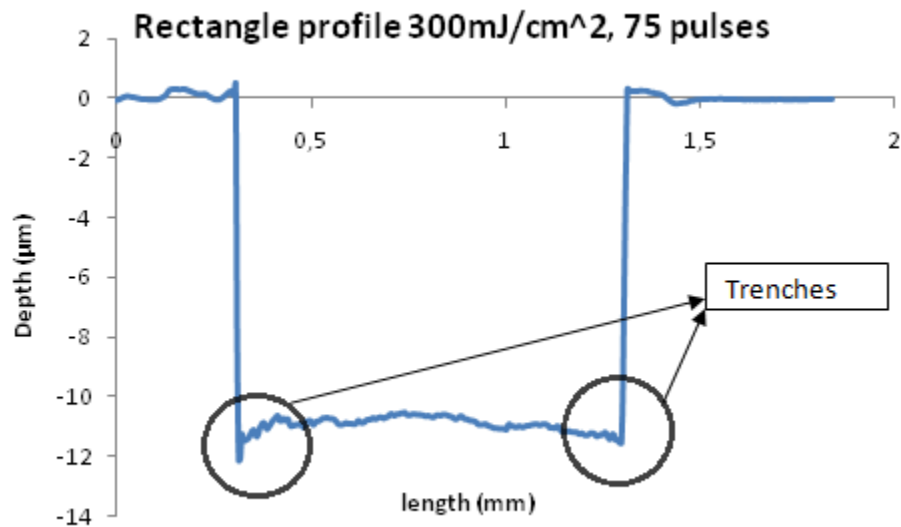
From the previous comparison between the two polymers, a total different behavior is observed with regard to the shape deformation, under the same experimental conditions. An explanation based on diffraction effects seems improper in the case of polyimide. So, it seems that material properties should be taken into account in the bump formation.

The experiment at the edge of the sample indicates that the bump is probably correlated with the plume expansion. When a portion of the ablated cavity is outside the borders of the substrate, the expansion of the plume might differ. There is another passage at the side of the cavity for plume expansion, so that a less pronounced plume shielding effect takes place. This means less energy attenuation and higher ablation rate.

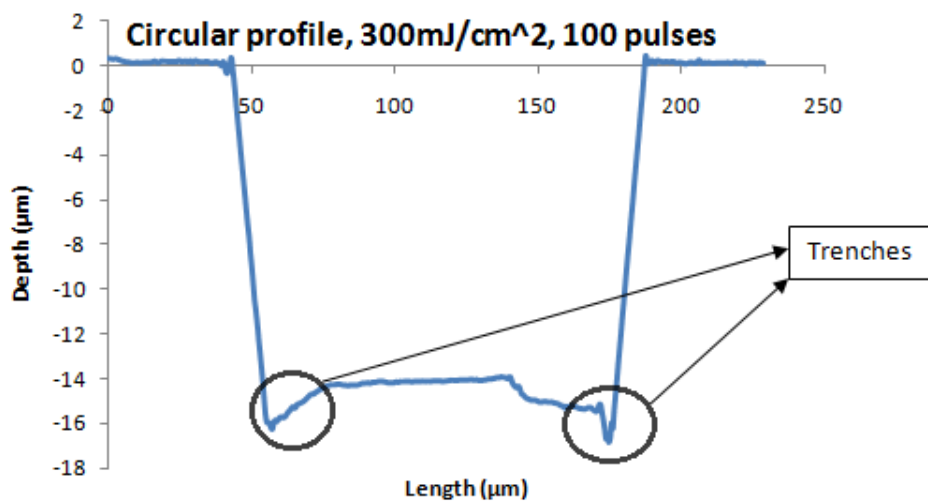
A.3. Trenches

The characterization of this type of surface deformation was very trivial because of the lack of accurate measurements. Especially, for the setup that was used for this study (wyko interferometer), the observation of the area near the sidewalls wasn't accurate and was depending on the magnification.

The trenches were observable both in rectangular and circular topologies.



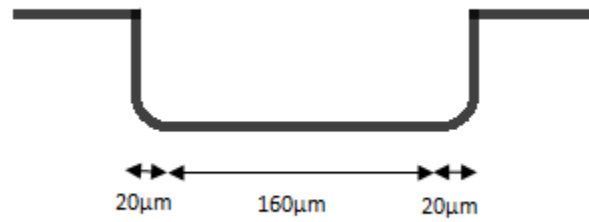
Graph 6.23: Trenches in a rectangular cavity



Graph 6.24: Trenches in a circular cavity

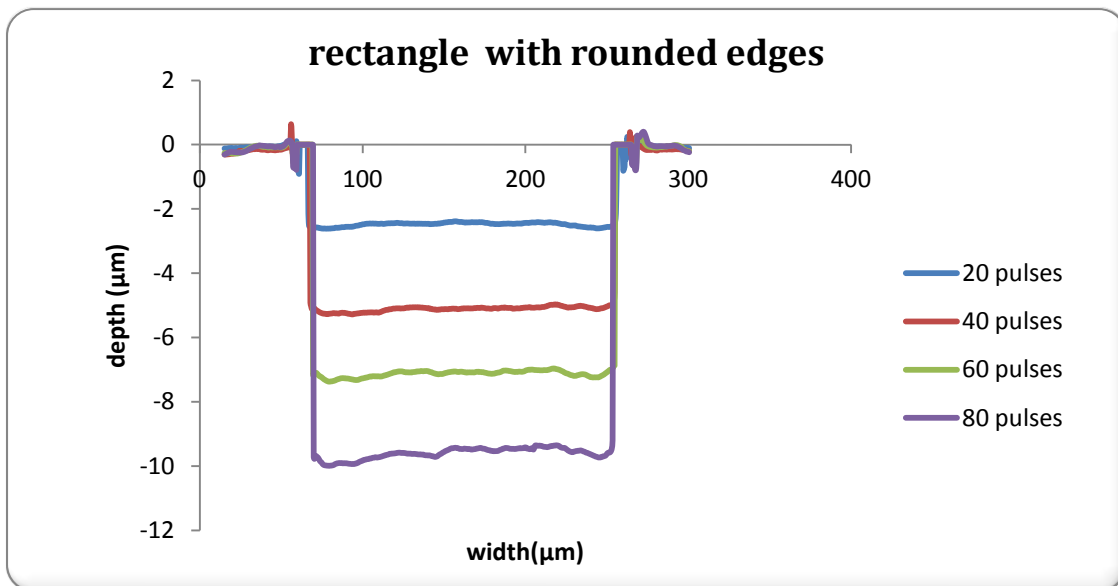
A.3.1. Experimentation with rectangular mask pattern with rounded edges

In this experiment, a rectangular aperture (200 μm width x 400 μm length) whose edges (20 μm) had less transmission than 100% (grayscale design) was used, in order to acquire a rectangular surface with rounded edges on the sample. The intended designed topology is depicted in the graph below.



Graph 6.25: Expected depth profile of the microstructure's topology

The result from the ablation process was not the expected (graph), but it revealed a way to compensate with the trench deformation. The incorporation of a parameter in the grayscale design that compensates with this irregularity seems to be a valuable tool in the laser ablation process.



Graph 6.26: Depth profile of rectangle with rounded edges pattern

Part B. Roughness reduction with the synchronized method

In the following experiments the synchronized reduction method was compared with the step and repeat method for different parameters. The length scale of roughness was determined around 13 μm . So, everything less than 13 μm is filtered. The irregularities above 13 μm are considered shape deformation and remain intact in the smoothed surface.

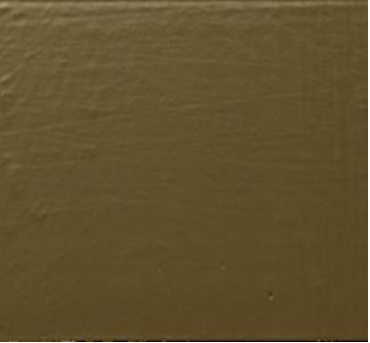

B.1. Experimentation with a large rectangular mask pattern

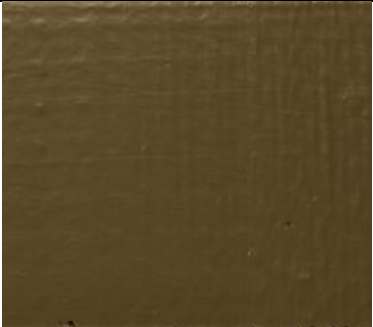




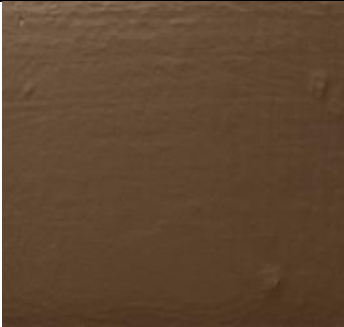



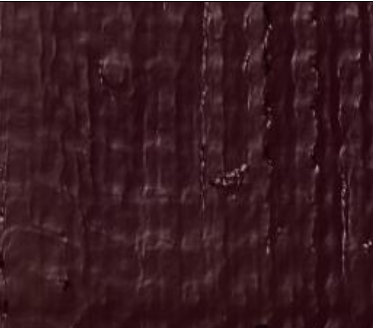

In this part the synchronized roughness reduction method was examined with different parameters with a rectangular mask pattern (side at x axis: 2mm, side at y axis: 400 μm).

The translation of the x axis was $\Delta x=0.1$ mm and of the y $\Delta y=0.02$. The ablated patterns were compared with patterns that were produced with the simple step and repeat method under identical experimental conditions (energy fluence, repetition rate, number of pulses). The first column shows the ablated topographies that have been produced by the simple method and the second (and third occasionally) column shows the corresponding ablated topographies that have been produced by synchronized scanning. Each row corresponds to a certain number of pulses.

B.1.1. Energy fluence 400mJ

The energy fluence that was used for the following experiments was 400mJ. All the samples were irradiated at 50 Hz. In the second column the synchronized method has been used with 2 loops and in the third with 8 loops.

	Step and repeat	Synchronized scanning 2 loops	Synchronized scanning 8 loops
20 pulses	 <p>Rq=14 nm</p>	 <p>Rq=12 nm</p>	

40 pulses	 <p>Rq=21 nm</p>	 <p>Rq=15 nm</p>	 <p>Rq=11 nm</p>
80 pulses	 <p>Rq=42 nm</p>	 <p>Rq=13 nm</p>	 <p>Rq=15 nm</p>
160 pulses	 <p>Rq=57 nm</p>	 <p>Rq=22 nm</p>	 <p>Rq=18 nm</p>
200 pulses	 <p>Rq=66 nm</p>	 <p>Rq=30 nm</p>	





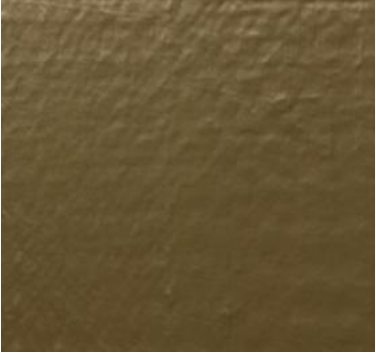

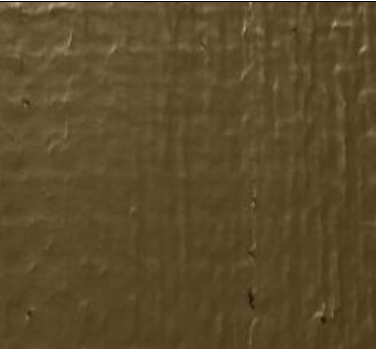

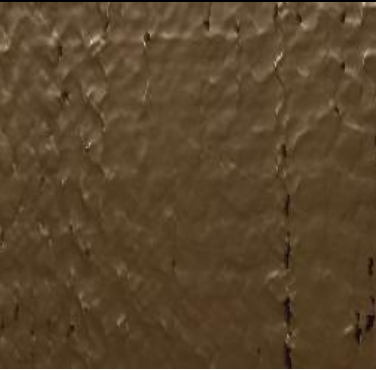

224 pulses	 Rq=63 nm		 Rq=19 nm
-------------------	--	--	--

Table 2: Synchronized scanning versus step and repeat for 400mJ/cm²

B.1.2. Energy fluence 100mJ

The energy fluence that was used for the following experiments was 100mJ. All the samples were irradiated at 50 Hz. In the second column the synchronized method has been used with 4 loops.

40 pulses	 Rq=17 nm	 Rq=8.4 nm
------------------	--	--

80 pulses	 <p data-bbox="354 590 493 625">Rq=39 nm</p>	 <p data-bbox="781 590 920 625">Rq=14 nm</p>
160 pulses	 <p data-bbox="354 1064 493 1100">Rq=50 nm</p>	 <p data-bbox="781 1064 920 1100">Rq=20 nm</p>
240 pulses	 <p data-bbox="354 1545 493 1581">Rq=64 nm</p>	 <p data-bbox="781 1545 920 1581">Rq=27 nm</p>



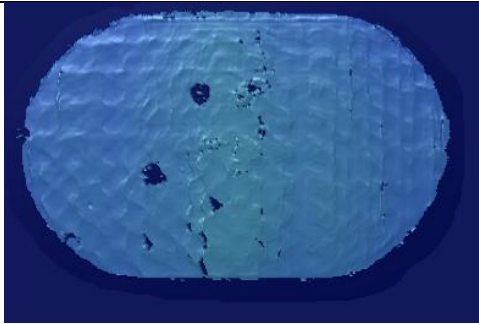
320 pulses		
	Rq=92 nm	Rq=34 nm

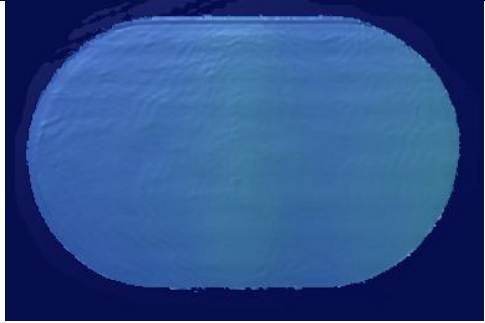
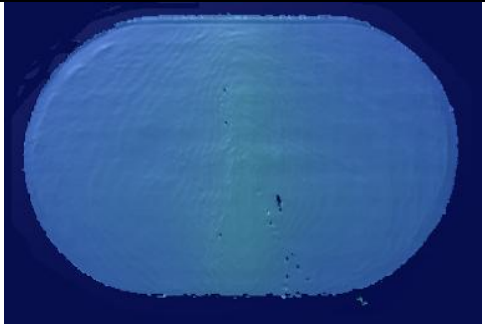
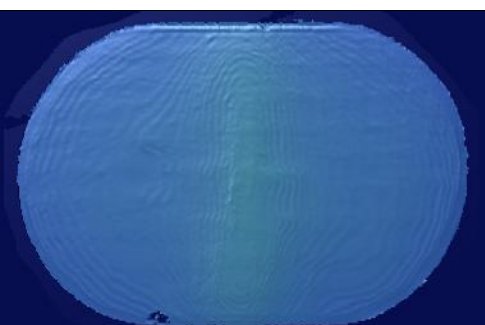
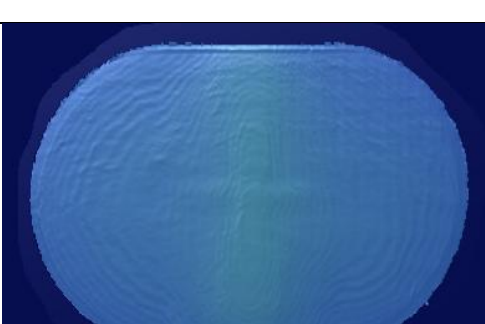
Table 3: Synchronized scanning versus step and repeat for 100mJ/cm²

B.2. Experimentation with a smaller ellipse

In this part the synchronized roughness reduction method was examined for different parameters with an elliptical mask pattern (major axis at x: 600µm, minor axis at y: 400µm).

All the samples were irradiated by 120 pulses, with 300 mJ/cm² and 50 Hz repetition rate. Below there are presented the ablated topologies for different Δx and Δy translations of a synchronized scanning with 4 loops and are compared with the topology of a simple ablation process.

	<p>Step and Repeat method Rq= 67 nm</p>
---	---

	<p>Synchronized</p> <p>$\Delta x = 1, \Delta v = 0.04$ mm</p> <p>Rq = 13 nm</p>
	<p>Synchronized</p> <p>$\Delta x = 0.5, \Delta v = 0.02$ mm</p> <p>Rq = 21 nm</p>
	<p>Synchronized</p> <p>$\Delta x = 0.4, \Delta v = 0.1$ mm</p> <p>Rq = 20 nm</p>
	<p>Synchronized</p> <p>$\Delta x = 0.8, \Delta v = 0.1$ mm</p> <p>Rq = 22 nm</p>

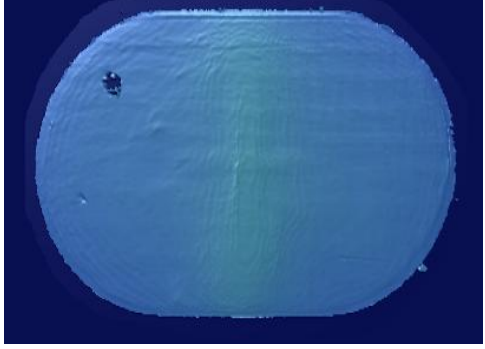
	<p>Synchronized</p> <p>$\Delta x=0.2, \Delta v=0.1$ mm</p> <p>Rq=19 nm</p>
---	---

Table 4: Synchronized scanning versus step and repeat for 300mJ/cm²

B.3. Discussion

In the first experiment with 400 mJ/cm² we can see that the rms roughness as well as the top view of the ablated cavity of the step and repeat and synchronized method for low number of pulses (20 and 40 pulses) are comparable. So there is no significant improvement with the synchronized scanning. For higher number of pulses there is an obvious improvement of roughness and can be seen both qualitatively and quantitatively. Between the one synchronized method that used two loops and the other that used eight, no significant difference is observed. Even though there is a slightly reduction of roughness in 8 loops than 2, no conclusion can be reached with respect to loops increment.

In the second experiment with 300 mJ/cm², the improvement of roughness is obvious for all the number of pulses. It should also be noted that for both step and repeat and synchronized methods the roughness is accumulated as the number of pulses increases.

In the experiment with the ellipse pattern, different Δx and Δy translations were tested. It was presumed that as Δx increases, the roughness would be improved due to a larger area of the fluence distribution. This assumption wasn't confirmed as we can see that the surface roughness is comparable.

Generally from the above experiments, it is clear that the surface roughness is improved by the use of the synchronized scanning method.

Chapter 7: Conclusions and future perspective

7.1. Introduction

In this chapter we will summarize some of the previous experimental results and we will give some conclusions and some proposals for future experiments. The previous separation between shape deformations and roughness will carry on also here.

7.2. Shape deformations

In this study, an attempt was made to classify the surface irregularities of the machined samples that are created during the laser ablation process into three categories (tapered sidewalls, trenches, curved bumps). Moreover, not exactly a shape deformation problem, but a parameter (mask size-ablation rate) that makes the prediction of cavity's depth quite ambiguous was examined.

7.2.1. Tapered sidewalls

The problem of the tapered sidewalls of the ablated region wasn't investigated. It is very common problem that is expected during laser ablation and can be tolerable with respect to the applications that laser machined workpieces are used. For this reason, no particular analysis was done.

7.2.2. Curved bump

From the previous experiments, the behavior of the bump deformation in circular holes was examined. The initial experiments lead to a behavior that could be explained by optical effects such diffraction that derive from the specific machining system. However, the subsequent experiments didn't confirm that assumption, but they made it more controversial. If there were diffraction problems, they should also be detectable to a material with similar behavior, but this doesn't seem to be the case. The polyimide seems to have a totally different behavior. Two assumptions were made for the explanation of this behavior.

Assumption 1:

An explanation that is based on optical effects such as diffraction that derive from systematic optical errors may be used. The reason that these effects are not visible on polyimide may rely on

a quite different model (for laser mater interactions) that applies in the case of polyimide. It has been reported [40] the probability of a thermal mechanism that takes part into the ablation process.

Assumption 2:

Another more possible explanation is related to the plume expansion and the debris deposition inside the cavity. Polyimide has no melting temperature and only evaporates, whereas polycarbonate does melt. So, there might be some kind of resolidification of polycarbonate's ablated debris and redeposition in the cavity. That debris adhere to the ablated surface and they contribute to the deformation. So, the deformation is only observable in the case of polyimide.

This assumption is reinforced by the fact that there was no mechanism for debris extraction in the system, but in the other excimer system there was an exhaust.

If this deformation derives from the debris redeposition inside the cavity, the shape of the expanded plume should affect the final pattern. So, in order to test this assumption, an experiment with a gas that provide a different plume expansion shape (like helium [41]) instead of ambient air is recommended. If a different deformation pattern will be observed, this assumption will get closer to confirmation.

7.2.3. Trenches

The trenches around the ablated cavity, that were mentioned above, is another shape deformation problem.

In some cases it is caused by diffraction effects and can be simulated satisfyingly, but in other cases only the diffraction by itself cannot explain this phenomenon. There comes an explanation with laser irradiation that is reflected from the sidewalls and it contributes to the radiation near the edges, as it was stated above. This contributes to a higher ablation rate near the sidewalls.

It seems that if this problem will be done predictable and reproducible, it can be compensated by adding some grayscale features at the initial design. The grayscale will attenuate the irradiation at the edges at first place, in a way that the extra energy that will be added won't contribute to the final result. But to do so, more experiments are required and more accurate measurements near the sidewalls, because the reliable estimation of the trenches' problem is a remaining problem.

7.2.4. Ablation rate- Mask area dependence

From the previous experiments, an ablation rate-mask area dependence was confirmed. It seems also to exist for both mask shapes (circular/rectangular). The ablation rate increases as the ablation area decreases, but that seems to take place under a critical value size. This size was determined in a previous study [36] around 200 μm diameter.

The explanation of this behavior is really trivial but it seems that is related with the expansion of the ablation plume and the plume shielding. It seems also that for fs laser this dependence doesn't exist ([36]) and the ablation rate is the same for all the different hole diameters. This could be explained by the fact that the plume expansion needs time of ns order to happen and the pulse duration is in the order of fs. That means that the laser irradiation reaches the surface before the plume shielding effect take place.

The question that arises then is why the plume attenuates less the irradiation when the hole has smaller size. An assumption is that inside the smaller holes the size of the clusters that are contained in the plume is smaller than those in the larger holes and they absorb and scatter less the laser irradiation or that the density of the plume is less([19], [38], [39]). Another assumption has to do with the kinetics of the plume which may change for different aperture sizes. In both cases, the bottom line of the explanation is the less attenuation of the laser radiation inside the smaller cavities.

One step further, even if the understanding of this phenomenon is still under discussion, this dependence should be taken into account during the ablation process. The possibility of a predictable estimation of this dependence and the adjustment of the suitable laser parameters in order to achieve the desired depth should be considered.

The ablation curve should be changed every time with regard to the size of the area that will be ablated. So, in the case of a smaller aperture, the new ablation curve will be left from the original ablation graph.

7.3. Roughness reduction

From the experimentation with the synchronized technique for roughness reduction, we can say that generally improves the quality of the surface and reduces roughness. However, it doesn't

improve the shape deformation of the microstructure. The next step concerning that technique will be the optimization of it by finding the proper laser parameters.

Another technique that should also be used for roughness reduction in the future is the irradiation with energy under the threshold after the laser ablation, which is the post processing method of laser polishing.

7.4. Final word

In this report some of the shape deformations that are introduced in the microstructure during the laser ablation process were examined. However, in the case of grayscale mask, deformations of the final microstructure shape can result from improper design, quantization errors etc, which were not examined here.

It seems that even though the laser ablation is a technology that has been used for many years, a lot of questions remain unanswered and there is not a clear understanding of it. New challenges are created continuously as the need for more accurate micromachining increases and more research is needed to be done. The entrance of the grayscale technology gives new potential to the laser ablation technology and it may contribute to the solution of some deformation issues. But still, a lot of evaluation tests and experiments are needed to be done first.

Acknowledgements

First of all, I would like to express my gratitude and deep appreciation to my supervisor Mr Rene Sanders for his valuable contribution to my work. I sincerely thank him for the precious guidance, constant support, useful advices and the time he spent helping me, from the beginning till the end of my internship. I would also like to thank all the members of the mesooptics team (Siebe de Zwart, Marcel Krijn, Wil Michiels, Hans van der Schaft, Ruslan Sepkhanov et al.) for their thankworthy contribution and ideas to my work and generally to the project. I wish also to thank a lot Hans Kroes for his support and assistance during my time in Philips. Last but not least I would like to express a special thanks to Longfei Shen for the beautiful collaboration that we had and the useful advices that he offered me during our conversations.

In closing, I am grateful to my supervisor in ntua, Mrs Ioanna Zergioti for her support and for giving me this great opportunity to participate in this project.

References

- [1] B. Pratap, C.B. Arnold, A. Piqué, “Depth And Surface Roughness Control On Laser Micromachined Polyimide For Direct-Write Deposition”, SPIE MF, 4979, 217-226, 2003
- [2] Deyao Ren , “Laser Micromachining and Its Applications in Manufacturing of Micro Medical Devices”, dissertation, North Carolina State University, 2009
- [3] Laser micromachining seminar, resonatics
- [4] H Ottevaere, R Cox, H P Herzig, TMiyashita, K Naessens, MTaghizadeh, R Volkel, H J Woo, H Thienpont, “Comparing glass and plastic refractive microlenses fabricated with different technologies”, J opt A-Pure Appl. Op. 8, 7, 407-429, 2006
- [5] Emir Mutapcic , “Optimised Part Programs for Excimer Laser-Ablation Micromachining Directly from 3D CAD Models”, thesis, Swinburne University of technology, Hawthorn, Victoria, Australia, 2006
- [6] Koji Sugioka, Michel Meunier , Alberto Piqué, “Laser Precision Microfabrication”, Springer, 2010
- [7] Kris Naessens, “Excimer laser ablation of microstructures in polymers for photonic applications”, Gent university, 2004
- [8] Thomas Lippert, “UV Laser Ablation of Polymers: From Structuring to Thin Film Deposition”, 2009
- [9] N. Bityurin, B. S. Luk’yanchuk, M. H. Hong, T. C. Chong, “Models for laser ablation of polymers”, Chem. Rev., 103, 519-552, 2003
- [10] N. Arnold, N. Bityurin, “Model for laser induced thermal degradation and ablation of polymers”, Appl. Phys. A 68, 615-625 , 1999
- [11] K. Zimmer, A. Braun, “Excimer laser machining for 3D-surface structuring, PEPDA, 301-338, 2003
- [12] M.C. Castex, N.Bityurin, “ Is the VUV ablation a pure photochemical process?”, Applied Surface Science, 197-198, 805-807, 2002
- [13] Claude Phipps, “Laser ablation and its applications”, Springer, 2007
- [14] A N Panchenko, M A Shulepov, A E Telminov, L A Zakharov, A A Paletsky, N M Bulgakova, “Pulsed IR laser ablation of organic polymers in air: shielding effects and plasma pipe formation”, J. Phys. D: Appl. Phys., 44, 385201, 2011
- [15] Leonid V. Zhigile, Barbara J. Garrison, “Velocity distributions of molecules ejected in laser ablation”, Appl. Phys. Lett., 71, 4, 1997
- [16] Khurshid Aslam Bhatti, “Plume Dynamics and Radiation Emission from Laser Plasmas”, Phd thesis, University of Engineering and Technology, Lahore-Pakistan, 2010
- [17] S. S. Harilal, C. V. Bindhu, M. S. Tillack, F. Najmabadi, A. C. Gaeris, “Internal structure and expansion dynamics of laser ablation plumes into ambient gases”, J. Appl. Phys., 93, 5, 2003
- [18] Gert Callies, Henrik Schittenhelm, Peter Berger, Helmut Hugel, “Modeling of the expansion of laser-evaporated matter in argon, helium and nitrogen and the condensation of clusters”, Appl. Surf. Sci., 127-129, 134-141, 1998
- [19] M. S. Tillack, D. Blair and S. S. Harilal, “The effect of ionization on cluster formation in laser ablation plumes”, University of California, San Diego, 2003

- [20] Igor Zinovik, Alex Povitsky, "Dynamics of multiple plumes in laser ablation: modeling of the shielding effect", *J. Appl. Phys.* 100, 024911, 2006
- [21] Ultraviolet laser ablation of polymers: spot size, pulse duration, and plume attenuation effects explained, *J Appl Phys*, 83, 10, 5458-5468, 1998
- [22] P.E.Dyer, "Excimer laser polymer ablation: twenty years on", *Appl. Phys. A* 77, 167-173, 2003
- [23] J. E. A. Pedder, A. S. Holmes, P. E. Dyer, "Improved model for the angular dependence of excimer laser ablation rates in polymer materials", *Appl. Phys. Lett.* 95, 174105, 2009
- [24] Nadeem H. Rizvi, Phil T. Rumsby, Malcolm C. Gower, "New Developments and Applications in the Production of 3D Micro-structures by Laser Micro-machining"
- [25] Andrew S. Holmes, James E.A. Pedder, Karl L. Boehlen, "Advanced Laser Micromachining Processes for MEMS and Optical Applications", *Proc. of SPIE*, 6261, 6261E-1, 2006
- [26] C J Hayden, "Three-dimensional excimer laser micromachining using grayscale masks", *J. Micromech. Microeng.*, 13, 599-603, 2003
- [27] A.S. Holmes, "Excimer laser micromachining with half-tone masks for the fabrication of 3-D microstructures Holmes", *IEE Proc., Sci. Meas. Technol.*, 151, 2, 85-92, 2004
- [28] Sexton, B.A., Hayes, J.P., Dempster, B., Harvey, E.C., "Electroplated Microstructures from Excimer Laser Micromachined Moulds", *Proceedings of 12th International Conference on Heat Treatment and Surface engineering*, Vol. 3, Melbourne, Australia, 2000
- [29] Yung-Chun Lee, Shi Hoa Kuo, "Miniature conical transducer realized by excimer laser micromachining technique", *Sensors and actuators A*, 93, 57-62, 2001
- [30] Yung-Chun Lee, Chun-Ming Chen, Chun-Ying Wu, "A new excimer laser micromachining method for axially symmetric 3D microstructures with continuous surface profiles", *Sensors and Actuators A*, 117, 349-355, 2005
- [31] T. W. Hodapp, P. R. Fleming, "Modeling topology formation during laser ablation", *J. Appl. Phys.* 84, 577, 1998
- [32] Erol C Harvey, Phil T Rumsby, Malcolm C Gower, Jason L Remnant, "Microstructuring by Excimer Laser", *Proc. SPIE*, 2639, 266, 1995
- [33] Karl L. Boehlen, Ines B. Stassen Boehlen, "Laser micro-machining of high density optical structures on large substrates", *Proc. SPIE*, 5339, 118, 2004
- [34] Emir Mutapcic, Pio Iovenitti, Jason P. Hayes, "Overlay error effects on polycarbonate structures produced by 248 nm UV laser ablation tool", *Proc. SPIE*, 5339, 118, 2004
- [35] M. Himmelbauer, E.Arenholz, D.Bauerle, K. Schilcher, "UV-laser-induced surface topology changes in polyimide", *Appl. Phys A*, 63, 337-339, 1996
- [36] B.Wolff, J.Ihlemann, H.Schmidt, A.Scholl, "Influence of the laser-spot diameter on photo-ablation rates", *Appl.Phys. A* 60, 13-17, 1995
- [37] Xianzhong Zeng, Samuel S. Mao, Chunyi Liu, Xianglei Mao, Ralph Greif, Richard E. Russo, "Plasma diagnostics during laser ablation in a cavity", *Spectrochim Acta B*, 5, 867-87, 2003
- [38] M. Mendes, R. Vilar, "Influence of the working atmosphere on the excimer laser ablation of Al₂O₃-TiC ceramics", *Appl Surf Sci*, 206, 196-208, 2003
- [39] M. Eyett, D. Bäuerle, "Influence of the beam spot size on ablation rates in pulsed laser processing", *Appl. Phys. Lett.* 51, 2054, 1987
- [40] J. Wei, N. Hoogen, T. Lippert, O. Nuyken, A. Wokaun, "Novel Laser Ablation Resists for Excimer Laser Ablation Lithography. Influence of Photochemical Properties on Ablation", *J. Phys. Chem. B*, 105, 1267-1275, 2001

- [41] Z.L.Li, S.Z. Yow, L.Lui, N.L. Yakovlev, Y.Sun, E.J. Swenson, P.M.Moran, "SIMS study of plumes generated from laser ablation of polymers", *Appl. Phys. A* 78, 611–616, 2004
- [42] John F.Ready, "LIA Handbook of laser materials processing", Laser institute of America, 2001
- [43] Dirk Basting, "Excimer Laser Technology: laser sources, optics, systems and applications", Lambda Physic, 2001
- [44] Introduction to industrial laser material processing:
<http://www.primross.com.mx/laser/Laserbook.pdf>
- [45] Breck Hitz, J.J. Ewing, Jeff Hecht, "Introduction to laser technology", Wiley-IEEE Press, 3d edition, 2001

Appendix A

Principle of Operation : Excimer laser and Veeco interferometer

1. Excimer Laser

1.1 Introduction to excimer lasers: Basic principles

Excimer lasers are pulsed gas lasers that use a mixture of gases to provide emission at a series of discrete wavelengths in the ultraviolet region of the spectrum. The word excimer is a contraction of the term “excited dimer”, which refers to a diatomic molecule bound in its electronically excited upper state but repulsive or only weakly bound when in the lower ground state. Excitation of the laser gas mixture is usually by means of a fast electric discharge with a duration of a few tens of nanoseconds. This causes the formation of the excited molecule appropriate to the mixture of gases selected. Laser action takes place as a result of the transition of this short-lived species back to the repulsive ground state, where the atoms recombine to their original individual components, enabling the process to be repeated.

The mixture of laser gases is confined within a pressure vessel, usually at a total pressure between 3000 and 5000 millibar. The electrodes used in the excitation process are typically between 50 and 100 cm long and between 1 and 2 cm wide, to provide an adequate gain volume, and are separated from each other by a centimeter or more. The resultant laser beam is rectangular in cross section with an aspect ratio between 1 and 3.

All excimer lasers use a noble gas, a halogen gas, and an inert buffer gas whose function is to transfer energy efficiently to the excited dimer molecules composed of one noble and one halogen gas atom. In a typical gas mixture, approximately 2% of the gas will be the noble gas, 0.2% will be the halogen gas, and the balance of several thousand millibars the buffer gas, usually helium or neon. Neon is often preferred, despite its higher cost, because it is the most efficient in transferring energy from the discharge to the lasing molecule [42].

A typical excimer laser gas mixture is a Kr:F₂:Ne blend with neon constituting most of the volume. The neon acts as a third body collision partner in the formation of the excited KrF molecule. The voltages and currents required for excimer laser operation test the limits of electronic technology. Consequently, excimer lasers are more complex than other types of lasers, require more maintenance and are more expensive to maintain. Some more disadvantages of excimer lasers are that the laser gas is toxic and corrosive, so that the components inside the laser

require routine replacement and cleaning, changes in the gas chemistry affect beam shape and quality, and resonator optics and beam delivery optics degrade with the exposure to uv light and require replacement.

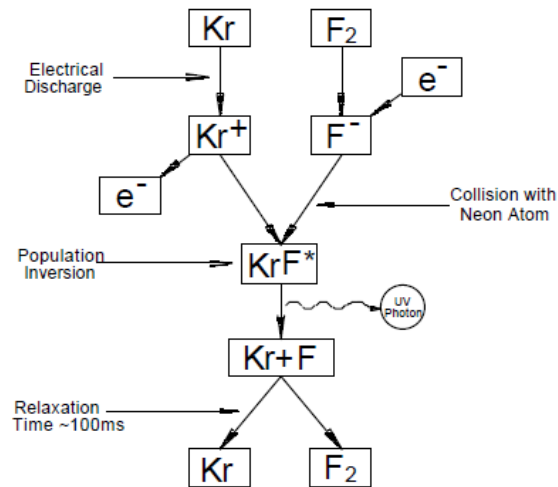


Figure 7: Simplified diagram of molecular transition in the KrF excimer laser [17]

1.2 Wavelengths

The wavelength emitted depends upon the selection of rare and halogen gas mixture. The most commonly used rare gases are argon, krypton, and xenon and the halogen gases fluorine or chlorine (supplied in the form of HCl). The halogen gases are usually supplied diluted by the buffer gas in concentrations of between 5 and 10% [42].

1.3 Resonator configurations

Most excimer lasers are used with stable resonators, usually with plano-plano high reflector and output coupler mirrors. The resonator mirrors are normally attached to the laser pressure vessel and form part of the gas seal. The high gain of the excimer medium requires output coupling reflectivities of 10-30% for most efficient energy extraction. Typical beam divergencies are then of the order of 3 mrad (50% energy points).

When lower divergence is required, excimer laser may be equipped with unstable resonators with a high magnification (up to 10x) to take account of the relatively few number of round trips that the discharge duration will support. This will reduce the beam divergence to a value between 200 and 400 microradians in a beam with 60-70% of the energy obtained with a conventional stable resonator.

1.4 Power sources

Excimer lasers are energized by the deposition of charge stored in a capacitor array into the volume of gas between the main laser electrodes. To ensure that a glow discharge is achieved between the main electrodes, a preionization discharge provides ultraviolet photons to initiate photoionization of the laser gas between them. Usually, this takes the form of a spark discharge between an array of small, secondary electrodes that run the full length of the main electrodes.

Switching of energy from the main storage capacitor into the discharge has often been effected by a hydrogen thyratron. In early excimer lasers, the fast discharge with its associated high peak currents and current reversals caused these thyratrons to have a life limited to few tens of millions of pulses. This formed a major component of the cost of operating an excimer laser. More advanced circuit designs, including the use of saturable magnetic materials, pulse compression stages, and suppression of reversed currents, have extended thyratron lifetimes into the region of several billion pulses, with a consequent reduction of operation costs. Recently, solid-state switching devices (SCRs) have been used in conjunction with multiple stages of magnetic compression of the current pulse to provide the source for energizing the excimer laser gas. [42]

1.5 Optical configurations

The specific excimer laser based optical system is a mask illumination and imaging set up. The feature to be ablated is first made in a mask which contains the enlarged pattern. This has considerable advantages, especially if small features are to be produced. In the mask, dimension 5 to 10 times larger can be selected, simplifying the manufacture. Using 5:1 image reduction, the structure can be projected onto the sample. If high resolution imaging is required this will, however, place very high demands on the quality of the projection lenses. The mask must be made of a material that can resist the energy densities during illumination.

The illumination optics typically include a telescope beam forming anamorphic telescope, the homogenizer optics and a field lens. The field lens couples the illumination optics to the imaging optics. Thus the light source is imaged to the stop of the imaging lens.

1.6 Attenuators

The simplest way of attenuating excimer laser light is by putting UV-transparent windows in the beam path. There are losses of approximately 8% per window. Using several windows allows the

appropriate variation option to be obtained; but with a large attenuation factor this is very costly. A less costly method is the use of neutral filters. Neutral filters, which consist of coated metal layers can be used at low energy densities only, because of the existing absorption of the UV light by the metal. For the substrate, a UV-transparent material has, of course, to be used. Varying the thickness of the metal layer allows very different degrees of filter transmission to be obtained. For the UV range, either quartz or CaF_2 substrates have to be used. Aluminum, gold or nickel layers may be used in the UV range as neutral filters. The layer thickness is in the region of a few nanometers.

A very elegant attenuating method which allows variable reduction is the use of dielectric cut off filter. Cut off filters, like dielectric mirrors, consist of various $\lambda/4$ layers which have a very steep transmission cut off with the corresponding arrangement [43].

1.7 Beam guidance

Beam guidance components refers to all components which guide the laser beam from the source to the machining head. This may include, for example, external telescopes for diverging the beam, beam switching modules (also called beam splitters) and energy-shaping modules as well as mirror elements for bending the beam.

1.7.1 Beam telescope

Telescopes can be used for controlling the diverging the raw beam generated by the laser. They can be used, for example to adjust the beam diameter to the free aperture of a focusing optics system. By means of adaptive telescope configurations, constant input beam diameters can be generated on the focusing optics. This can compensate for effects that result from different operating conditions of the beam source or from variable lengths of the beam path in processing systems [44].

The telescope preferably is arranged as a Galilean telescope from two positive lenses. The conjugate planes are to be arranged close to the laser exit (distance < 1000mm) and at the homogenizer entrance aperture. Alternatively, the Kepler telescope (positive and negative lens)

can also be used to save space. The disadvantage of this telescope is that the conjugate planes are at infinity and that no aperture (or to be more precise, near field profile at the exit or close to the excimer laser resonator) is imaged [42].

1.7.2 Mirrors

Laser mirrors are usually dielectric mirrors. They are made by depositing alternate layers of high and low- index materials on a substrate. A fraction of the incident light is reflected from each interface, and the total reflectivity depends on the relative phase of these reflections.

A high reflectivity mirror, for example, might have several layers of transparent deposited on glass substrate. Each layer would be exactly the right thickness so that the light reflected from its front surface would be precisely in phase with the light reflected from its rear surface. It is possible to fabricate dielectric mirrors like this whose reflectivity is greater than 99.999%. [45]

1.7.3 Homogenizer

The point to point fluctuations in the energy distribution of an excimer laser beam can exceed more than $\pm 10\%$. This is already too much for “large” area high precision ablation applications. In principle, the homogenizer optics cut the beam in pieces and mix parts of the excimer laser beam with each other in a way such that the product is a complete, homogeneous distribution.

The raw beam of an excimer provides an inhomogeneity of about up to 20% for the inner part. Only the inner part of the raw beam (approximately 30%-50% of the total emitted laser light) can be used to get a 90%-100% homogeneous illumination. Additionally, the intensity distribution is varied pulse to pulse due to the nature of the high pressure electrical discharge in the excimer laser tube.

Critical to inhomogeneity is any slope sign change within a lenslet (lens array) size. Therefore, small lenslets are preferred. The laser beam is segmentally superimposed. This shows clearly that the beam profile becomes more homogeneous, the more beam segments that are built into the homogenizer (number of lens elements)[43]. The purpose of a beam homogenizer is to break up

the beam into small sections and recombine them in a pattern that increases the overall fluence over a smaller cross-section.

1.7.4 Field lens

A field lens is a large diameter plano-convex lens with a focal length of 1 to 2 meters. The purpose of a field lens is to collimate the laser beam onto the surface of the imaging lens or another lens[17]. The field lens is designed to image a pattern at a finite distance to a finite position. The purpose of the field lens is to image the light source into the projection lens. The position of this image is defined by the lens' stop. Thus the field lens images the pupil of the homogenizer to the lens' stop. [43]

1.7.5 Projection lenses

Projection lenses are designed to image a pattern at a finite distance to a finite position. The most simple projection lens is a plano-convex single element. However, such a lens has imperfections. Further the lenses provide a field curvature and a distortion if a larger field of view is considered. Projection lenses are developed to compensate within a given field of view (FOV) the aberrations and to minimize the field curvature and distortion. Further the lenses are developed for specific performance needs such as demagnification and energy density at the image plane, focal length/working distance, NA/resolution, telecentricity.

The substrate surface height changes through the ablation process. Consequently the projection lens has to provide a depth of focus of the same range as the drilling depth. The DoF and the NA(resolution) of a lens are directly related to each other by the following formula:

$$\text{DoF} = \pm \left(\frac{\text{blur}}{2NA} \right),$$

$$\text{Blur} = \frac{\lambda}{NA} \text{ (diffraction limit) or any application acceptable blur}$$

2. Wyko interferometer

2.1 Principle of operation

Light from the illuminator travels through the IOA (Integrated Optics Assembly) which contains a CCD camera, a field-of-view (FOV) lens, a filter assembly and an illumination source. Then it is reflected down to the objective by a beamsplitter. Once the light reaches the objective, another beamsplitter separates the light into two beams. One beam, the reference beam, reflects from a super smooth reference mirror in the objective, while the other (the test beam) reflects from the surface of the sample and back to the objective. If the surface of the sample is in focus, the two light beams will recombine and form an interference pattern of light and dark bands called fringes. The number of fringes and their spacing depends upon the relative tilt between the sample and the reference mirror. If the sample and the reference are parallel, only one large fringe will be seen. In this case, the fringes are said to be nulled. The interference pattern is received by the CCD camera and the signal is transferred to the computer, where it is processed by wyko vision32. Wyko vision32 will then produce a graphical output display representing a contour map of the sample's surface.

For all the measurements the vertical scanning interferometry (VSI) mode was used. Contrary to phase-shifting interferometry (PSI), the VSI mode does not suffer from the limitation on the maximum height difference between neighboring samples points ($\lambda/4$ limit). In VSI, an internal translator scans downward during the measurement as the camera periodically records frames. As each point on the surface comes into focus, the modulation on that point reaches a maximum, then tapers off as the translator passes through focus. By recording the height of the translator at maximum modulation, the system can determine the height of each pixel.

Appendix B

Excimer Scripts

Script for synchronized scanning - roughness reduction

```
' Program used for synchronized image scanning
question%=7
'Let the user enter his values
Def UserInterface() {file=ProcesSynchr}
    FocusPos!=36.25    {dsc="position elevator stage, z-pos"}
    nopulses!=10      {dsc="Number of pulses"}
    noloops!=10       {dsc="number of loops"}
    ZMask!=53.5       {dsc="Position of Z-axis mask"}
    UMask!=181.5      {dsc="Position of U-axis mask"}
    Reprate!=83       {dsc="Laser pulse frequency, min 1, max 200"}
    Atten!=62.647     {dsc="attenuator position"}
    'SpeedScan!=50    {dsc="define the scan speed (mm/min)}
    Xstep!=0.1        {dcs="define the step of the x-axis, zstep will be 5
times xstep}
    Ystep!=0.02       {dcs="define the step of the y-axis, ustep will be 5
times ystep}
    speed!=500        {dsc="speed of axis", hidden=1}
End Def

loop
Edit UserInterface() 'gives oppurtunity to check def values

'Move the axis according to the users' choise
G90 g1 V(UserInterface.Focuspos) F(UserInterface.speed)
G90 g1 Z(UserInterface.ZMask) F(UserInterface.speed)
G90 g1 U(UserInterface.Umask) F(UserInterface.speed)
IO.aset(2,25)
u500_1.wait()
u500_2.wait()
dwell(1000)

'Save the user's values in other variables
number=(UserInterface.number)
noloops=(UserInterface.noloops)
reprate=(UserInterface.reprate)
atten=(UserInterface.atten)
nopulses=(UserInterface.nopulses)
stepx=(UserInterface.Xstep)
stepz=5*stepx
stepy=(UserInterface.Ystep)
stepu=5*stepy

distance=(10000    stepz 2    noloops)/nopulses
speedscan=(distance    reprate    60)/10000

question%=msgbox("The distance between pulses is " &distance/10 &"um" &" and
the speedscan is " &speedscan &"mm/min" &"/n Is it ok for you?", 4)
```

```

if speedscan>2000 then
    msgbox("The scanspeed exceeds the machine limits" &/n"Try again!!!")
    question=7
endif

until (question%=6)

'Position sample under the camera, let the user define any last minute choice
Userjog(1,"Position sample under the camera", "X11100","Y12100")
XPosCam!=U500_1.fb("x")
YPosCam!=U500_1.fb("y")

'Move to laser position
Continue% = msgbox("Ok to move to laser position and fire shots? (btw turn on
the exhaust)",1,"Moveeeeeee")
if Continue=2 then
    forceabort()
endif
io.set(extract_pump,1)
G91 G1 X-(AlignCam.xalign) Y-(AlignCam.yalign) f(setFocus.FTable)
U500_1.wait()

laser_1.on          'laser on
laser_1.cmd("trigger=ext") 'trigger laser extern
Io.set(shutter_open,1) 'open shutter
Io.set(vac_on,1)      'open vacuum chunk
dwell(1000)          'wait 1 second ;- )

'moves the attenuator to correct position
smartmotor.move(0,500,atten)
smartmotor.wait
dwell(1000)

counter=0
loop
    counter=counter+1
    PR ME          'metric units
    bo 1          'Board 1
    PSOP,0,10     'pulse width 1msec
    PSOD,0,distance 'pulse distance set by user
    PSOF,3,x,z    'x-axis synchronized laserpulse
    G91 G1 x(stepx) z(stepz) f(speedscan)
    U500_1.wait() 'wait until Unidex board 1 has finished all actions
    dwell(100)
    g91 g1 y(stepy) u(stepu) f(speedscan)
    U500_1.wait()
    dwell(100)
    PSOP,0,10
    PSOD,0,distance
    PSOF,3,x,z
    G91 G1 x-(stepx) z-(stepz) f(speedscan)
    U500_1.wait()
    dwell(100)
    G91 G1 y(stepy) u(stepu) f(speedscan)
    U500_1.wait()

```

```

        dwell(100)
until counter=noloops

        u500_1.wait()

PSOF,0          'disable laser
io.set(shutter_open,0)      'shutter closed
LASER_1.OFF()
dwell(1000)
io.set(vac_on,0)
io.set(extract_pump,0)

bo 1
G90 G1 X(XPosCam) Y(YPosCam) f1000 `return to camera position
u500_1.wait()

EXIT()

```

✦ Synchronized scanning of a large area in one dimension (it was used for scanning the test pattern for the ablation curve)

```

' Synchronized scanning of a large area
'Let the user enter his values
Def UserInterface() {file=ProcesSynchr}
    FocusPos!=36.25    {dsc="position elevator stage, z-pos"}
    ZMask!=260        {dsc="Position of Z-axis mask"}
    UMask!=401.14     {dsc="Position of U-axis mask"}
    Reprate!=83       {dsc="Laser pulse frequency, min 1, max 200"}
    Atten!=62.647     {dsc="attenuator position"}
    maskstep!=100     {dcs="define the step of u or v"}

    speed!=500        {dsc="speed of axis", hidden=1}
End Def

Edit UserInterface()    'gives opportunity to check def values

'Move the axis according to the users' choise
G90 g1 V(UserInterface.Focuspos) F(UserInterface.speed)
G90 g1 Z(UserInterface.ZMask) F(UserInterface.speed)
G90 g1 U(UserInterface.Umask) F(UserInterface.speed)
IO.aset(2,25)
U500_1.wait()
U500_2.wait()

'Save the user's values in other variables
reprate=(UserInterface.reprate)
atten=(UserInterface.atten)
'nopulses=(UserInterface.nopulses)
maskstep=(UserInterface.maskstep)
speedscan=(maskstep*reprate*60)/10000
nopulses=135000/maskstep

msgbox("The speed of z axis is: " &speedscan &"mm/min" &"/nYou are going to
fire approximately: "&nopulses&" pulses")

```

```

if speedscan>2000 then
  msgbox("You have exceeded the axis speed limits.")
  forceabort()
endif

'Position sample under the camera
Userjog(1,"Position sample under the camera", "X1120",
"Y1220", "R2110", "V2210")
XPosCam!=U500_1.fb("x")
YPosCam!=U500_1.fb("y")

'Move to laser position
Continue% = msgbox("Ok to move to laser position and fire shots? (btw turn on
the exhaust)", 33,"Moving!!!!!!!")
if Continue=2 then
  forceabort()
endif
io.set(extract_pump,1)
G91 G1 X-(AlignCam.xalign) Y-(AlignCam.yalign) f(setFocus.FTable)
U500_1.wait()

laser_1.on
laser_1.cmd("trigger=ext")
Io.set(shutter_open,1)
Io.set(vac_on,1)
dwell(1000)

smartmotor.move(0,500,atten)
smartmotor.wait
dwell(1000)

PR ME
bo 1
PSOP,0,10
PSOD,0,maskstep
PSOF,3,z,x
G91 G1 z75 x15 f(speedscan)
U500_1.wait()

PSOF,0
io.set(shutter_open,0)
'disable laser
'shutter closed

dwell(1000)
LASER_1.OFF()
'laser off
io.set(vac_on,0)
io.set(extract_pump,0)

bo 1
G90 G1 X(XPosCam) Y(YPosCam) f1000
U500_1.wait()
'dwell(11000)

EXIT()

```

✦ Create a grid of holes with the same parameters

'Direct firing

```
Def ProceS() {file=ProceSVar}
  FocusPos!=36.25 {dsc="position elevator stage, z-pos"}
  nopulses!=10 {dsc="Number of pulses"}
  NOS!=10 {dsc="number of sites horizontally"}
  NOS2!=10 {dsc="number of sites verically"}
  ZMask!=53.5 {dsc="Position of Z-axis mask"}
  UMask!=181.5 {dsc="Position of U-axis mask"}
  Reprate!=83 {dsc="Laser pulse frequency, min 1, max 200"}
  Xstep!=4 {dsc="stepsize in x-direction [mm]"}
  Ystep!=4 {dsc="stepsize in y-direction [mm]"}
  Att!=40.7 {dsc="position of attenuator"}
  speed!=500 {dsc="speed of axis", hidden=1}
```

End Def

Edit ProceS

'Move the axis according to the users' choise

```
G90 g1 V(ProceS.focuspos) F100
G90 g1 Z(ProceS.ZMask) F(ProceS.speed)
G90 g1 U(ProceS.Umask) F(ProceS.speed)
IO.aset(2,25)
u500_1.wait()
u500_2.wait()
dwell(1000)
```

'Position sample under the camera

```
Userjog(1,"Position sample under the camera", "X11500", "Y12500")
XPosCam!=U500_1.fb("x")
YPosCam!=U500_1.fb("y")
```

```
Continue% = msgbox("Ok to move to laser position and fire
shots?",1,"Move!!!")
```

```
if Continue=2 then
```

```
  forceabort()
```

```
endif
```

```
G91 G1 X-(AlignCam.xalign) Y-(AlignCam.yalign) f(SetFocus.FTable)
U500_1.wait()
```

```
io.set(extract_pump,1)
```

```
Laser_1.on()
```

```
laser_1.cmd("trigger=ext")
```

```
Io.Set(Shutter_open,1)
```

```
bo 1
```

```
Dwell(2000)
```

```
number=(proceS.nopulses)
```

```
reprate=(proceS.reprate)
```

```
att=(ProceS.att)
```

```
SmartMotor.move(0,200,att)
```

```
SmartMotor.wait
```

```

dwell(1000)
bo 1

for counter1=1 to Proces.NOS2
  for counter2 = 1 to Proces.NOS

    bo 1
    psop,1,0,20,((10000/(reprate))-20)'set laser frequency at the correct
value
    psop,2,(number) 'fires correct number of pulses with correct freq.
    dwell(((1/(reprate)) (number)) 1000)+500) 'wait correct time
during fire of laser, before continue
    g91 g1 x(proces.xstep) F(proces.speed)'icremetal step in x direction
    U500_1.wait 'wait until U500_1 finished all actions
    dwell(500)
  Next counter2
  G91 g1 x-Proces.NOS (proces.xstep) F(proces.speed)
  G91 G1 Y(Proces.ystep) F(proces.speed)
  U500_1.wait
  dwell(500)
Next counter1

io.set(extract_pump,0)
Psof,0 'stop laser
Io.Set(Shutter_open,0)
io.set(vac_on,0)
laser_1.off
'Go back to camera position
G90 G1 X(XPosCam) Y(YPosCam) f(SetFocus.FTable)
U500_1.wait

EXIT()

```

Appendix C

Matlab scripts

Roughness evaluation

%Script that finds the rms value of roughness of an area in microns

```
close all;
clear all;
%.....initial values.....
name='elb.csv';
Lsx=1.65;
Lsy=1.93;
number1=8;
number2=7;
%.....Lengthscale.....
Lx=number1*Lsx
Ly=number2*Lsy
Fcx=1/number1;
Fcy=1/number2;
%.....Initial image.....
I=csvread(name);
I=0.08*I;
minI=min(min(I));
I(I==0)=minI;
I=abs(I-minI);
figure(1), mesh(I), title('3d initial image');
%.....

%Fourier Transformation
F_Y = fftshift(fft2(I));
F_Y_log = log10(1+abs(F_Y));
%figure(2),mesh(F_Y_log), title('FFT');
figure(5), imshow(F_Y_log/max(max(F_Y_log)));
axis equal tight;
[fx,fy]=freqspace(size(F_Y));%normalized frequencies -1..1
figure(2),mesh(fx,fy, F_Y_log), title('FFT');

%filter construstion
[r,c]=size(I);%r= rows,c columns
m_Y=zeros(r,c);
[fxx,fyy]=meshgrid(fx,fy);
m_Y(abs(fxx)<Fcx&abs(fyy)<Fcy)=1; %RECTANGULAR FILTER
figure(3), mesh (fx,fy,m_Y), title('filter');

%.....

%Implementation of the filter
F_Y_filtered=F_Y.*m_Y ;

%Inverse fourier
iF_Y = ifftshift(F_Y_filtered);
iY1 = ifft2(iF_Y);
```



```

figure(4), mesh(iY1), title('filtered surface');

%.....
E=abs(double(I)-double(iY1));
%cut the problematic areas at the edges
lim1=round(0.1*r);
lim2=round(0.1*c);
E= E(lim1:end-lim1, lim2:end-lim2);

Rq=sqrt(sum(sum(E.^2))/(r*c));
disp('The root mean square value of roughness is [um]'); disp(Rq);

```

✚ Estimate the laser fluence distribution that corresponds to the ablated depth distribution of the cavity

```

%clear all; close all;

%.....Initial values.....
F=350;%nominal fluence (mJ/cm^2)
nopulses=100;
%.....
z= xlsread('ablation curve.xls');
a=z(4:end,:);
a2=z(3:end,:);
b=xlsread('pc3.xlsx');
b_pi=xlsread('pi3.xlsx');
%b=b(4:end,:);
rows = length(b(:,1));
F_nom=F*ones(rows,1);
%.....PC.....
p1 = polyfit(a(:,1),a(:,2), 5);
poll=p1(1)*a(:,1).^5+p1(2)*a(:,1).^4+p1(3)*a(:,1).^3+p1(4)*a(:,1).^2+p1(5)*a(
(:,1)+p1(6);
figure; plot(a(:,1), poll, z(:,1), z(:,2)); title('ablation curve of PC');
%.....PI.....
p1_pi = polyfit(a2(:,1),a2(:,3), 5);
poll_pi=
p1_pi(1)*a2(:,1).^5+p1_pi(2)*a2(:,1).^4+p1_pi(3)*a2(:,1).^3+p1_pi(4)*a2(:,1).
^2+p1_pi(5)*a2(:,1)+p1_pi(6);
figure; plot(a2(:,1), poll_pi, z(:,1), z(:,3));title('ablation curve of PI');

p2 = polyfit(a(:,2),a(:,1), 5);
c=abs(b(:,2)-b(:,3));
c=c./nopulses;
for i=1:rows
    if c(i)<0.002
        n(i)=0;
    else n(i)=
p2(1)*c(i)^5+p2(2)*c(i)^4+p2(3)*c(i)^3+p2(4)*c(i)^2+p2(5)*c(i)+p2(6);
    end
end

%figure; plot(b(:,1), n, b(:,1),F_nom);

```

```

%.....pi.....
rows_pi = length(b_pi(:,1));
F_nom_pi=F_ones(rows_pi,1);
p3 = polyfit(a2(:,3),a2(:,1), 5);
c_pi=abs(b_pi(:,2)-b_pi(:,3));
c_pi=c_pi./nopulses;
for i=1:rows_pi
    if c_pi(i)<0.002
        n_pi(i)=0;
    else n_pi(i)=
p3(1)*c_pi(i)^5+p3(2)*c_pi(i)^4+p3(3)*c_pi(i)^3+p3(4)*c_pi(i)^2+p3(5)*c_pi(i)
+p3(6);
    end
end

%figure; plot(b_pi(:,1), n_pi, b_pi(:,1),F_nom_pi);

figure; plot(b(:,1), n, b_pi(:,1), n_pi, b_pi(:,1),F_nom_pi);title('energy
distribution for pi and pc');

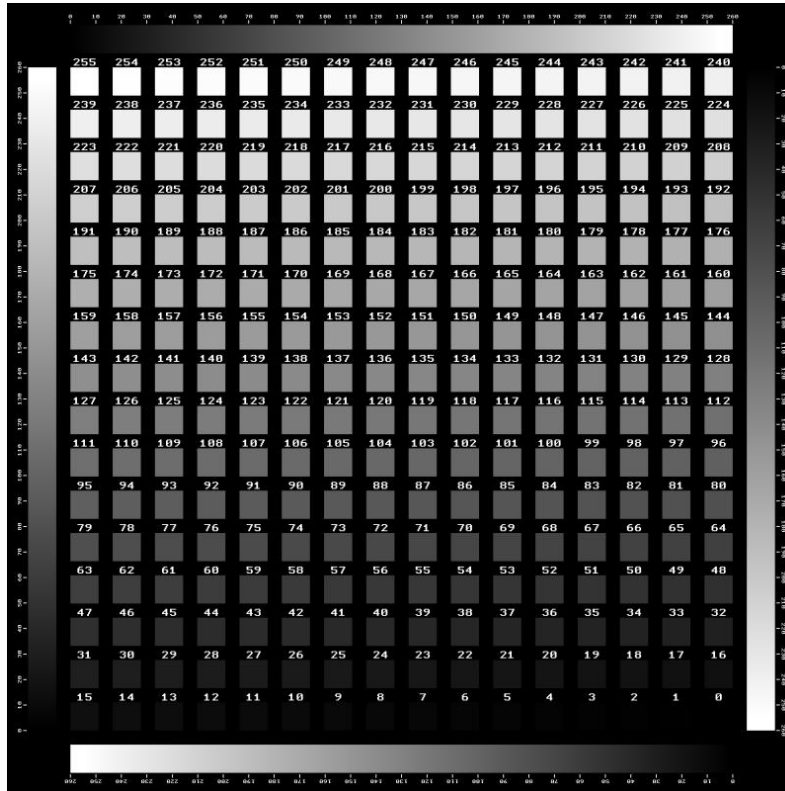
figure; plot(b(:,1), b(:,2), b_pi(:,1), b_pi(:,2));title('depth profile of pi
and pc');

```

Appendix D

Ablation curve mask

In order to acquire the data for the creation of the ablation curve the following grayscale test mask was used.



As we can see from the above pattern, at the sides there are “rulers” that begin from 0 and end up to 100% transmission.

A ruler was scanned by the laser beam with a fluence of $400\text{mJ}/\text{cm}^2$. Then the depth was measured by Veeco at every printed label of the “ruler” and assigned to a percentage of transmission.